INVESTIGATION OF MECHANICAL AND SUPERCONDUCTING PROPERTIES OF $Y_{1-x}Ho_xBa_{2-y}Nd_yCu_3O_{7-\delta}$ SUPERCONDUCTING SAMPLES BY EXPERIMENTAL AND THEORETICAL METHODS

by
NAMIK KEMAL SARITEKİN

THESIS SUBMITTED TO
THE GRADUATE SCHOOL OF NATURAL AND APPLIED SCIENCES OF
THE ABANT IZZET BAYSAL UNIVERSITY
IN PARTIAL FULFILLMENT OF THE REQUIREMENTS FOR THE DEGREE OF
DOCTOR OF PHILOSOPHY
IN
THE DEPARTMENT OF PHYSICS

FEBRUARY 2015

Approval of the Graduate School of Natural and Applied Science

Prof. Dr. Duran KARAKAŞ
Director

I certify that this thesis satisfies all the requirements as a thesis for the degree of doctor of philosophy.

Prof. Dr. İbrahim BELENLİ
Head of Physics Department

This is to certify that we have read this thesis and that in our opinion it is fully adequate, in scope and quality as a thesis for the degree of doctor of philosophy.

Prof. Dr. Cabir TERZİOĞLU
Co-Supervisor

Prof. Dr. Osman GÖRÜR
Supervisor

Examining Committee Members:

1. Prof. Dr. Cabir TERZİOĞLU …….

2. Prof. Dr. Osman GÖRÜR ……

3. Assoc. Prof. Dr. Mustafa AKDOĞAN ……

4. Assoc. Prof. Dr. Özgür ÖZTÜRK ……

5. Assist. Prof. Dr. Gürcan YILDIRIM ……

ABSTRACT

INVESTIGATION OF MECHANICAL AND SUPERCONDUCTING PROPERTIES OF $Y_{1-x}Ho_xBa_{2-y}Nd_yCu_3O_{7-\delta}$ SUPERCONDUCTING SAMPLES BY EXPERIMENTAL AND THEORETICAL METHODS

SARITEKİN, Namık Kemal

Doctor of Philosophy, Department of Physics

Supervisor: Prof. Dr. Osman GÖRÜR

Co-Supervisor: Prof. Dr. Cabir TERZİOĞLU

February 2015, 119 pages

This comprehensive study reports the effect of the Ho, Nd and co-doping inclusions on the microstructural, electrical, mechanical and superconducting characteristics of $YBa_2Cu_3O_{7-\delta}$ ceramic superconductors with the aid of standard characterization methods including the bulk density, dc resistivity, transport critical current density, X-ray diffraction, electron dispersive spectroscopy, scanning electron microscopy and vickers microhardness investigations. The experimental results such as the degree of granularity, hole localization effect, room temperature resistivity, critical transition temperature, degree of the broadening, thermodynamic fluctuations, crystallinity, crystal plane alignments, crystal structure, grain size, phase purity and lattice parameters, appearance of flux pinning centers, grain boundary weak-links, surface morphologies, real microhardness values, elemental

compositions and distributions belonging to the pure, Y-site Ho and Ba-site Nd substituted Y-123 superconducting samples are discussed in detail for the first time. Moreover, mechanical characterization enables us to theoretically determine the elastic modulus and yield strength being in charge of the potential mechanical applications. Additionally, the load dependent microhardness values of the samples have not been modeled by the available theoretical methods (Hays–Kendall and indentation-induced cracking approach) up to the present. All the experimental findings show that the microstructural, electrical, mechanical and superconducting properties improve regularly with the increment in the Ho concentration level at the Y-site in the YHo, in the Nd concentration level at the Ba-site in the YNd and in the Nd concentration level at the Ba-site and in the HcN (Ho constant+Nd changeble) until a certain value of x=0,100, y=0,250 and y=0,100, respectively, beyond which and with the increment in the Ho concentration level at the Y-site in the NcH (Nd constant+Ho changeble), the characteristics tend to retrograde rapidly. This is attributed to the fact that excess penetration of the Ho and Nd damages the crucial properties given above.

Furthermore, all the samples exhibit the typical reverse indentation size effect behavior under the applied indentation test load. The vickers microhardness measurement evidences also declare that the plastic deformation is superior to the elastic deformation. Based on the results, the IIC model is superior to HK approach for the description of the real microhardness values belonging to all the superconducting samples.

Keywords: X-ray diffraction, electron microscopy, ceramics; hardness measurement, mechanical characterization: grain boundaries.

ÖZET

$Y_{1-X}HO_XBA_{2-Y}ND_YCU_3O_{7-\delta}$ SÜPERİLETKEN MALZEMELERİN MEKANİK VE SÜPERİLETKENLİK ÖZELLİKLERİNİN DENEYSEL VE TEORİK METOTLARLA İNCELENMESİ

SARITEKİN, Namık Kemal

Doktora, Fizik Bölümü

Tez Danışmanı: Prof. Dr. Osman GÖRÜR

Yardımcı Tez Danışmanı: Prof. Dr. Cabir TERZİOĞLU

Şubat 2015, 119 sayfa

Bu kapsamlı çalışma, kritik akım yoğunluğu, X-ışını kırınımı, elektron dağılımlı spektroskometre, taramalı elektron mikroskobu, vickers mikro sertlik incelemeleri, kütle yoğunluğu ve dc özdirenç olmak üzere standart karakterizasyon yöntemlerinin yardımı ile Ho, Nd ve Ho ile Nd'nin beraber katkılanmasının $YBa_2Cu_3O_{7-\delta}$ seramik süper iletkenlerinin, elektriksel, mikro yapısal, mekanik ve süper iletkenlik özellikleri üzerinde etkisini anlatır. İlk önce, yapılan deney sonuçlarından, saf Y-123, Y yerine Ho ve Ba yerine Nd katkılanmış Y-123 süper iletkenlerine ait parçacık boyutu, boşluk yerelleştirme etkisi, oda sıcaklığındaki direnç, kritik geçiş sıcaklığı, büyültme derecesi, termodinamik dalgalanmalar, kristalleşme, kristal düzlem dizilişleri, kristal yapı, tanecik boyutu, faz saflığı ve kafes parametreleri, akı çivileme merkezlerinin görünümü, tane sınırı zayıf

bağlantıları, yüzey morfolojileri, gerçek mikro sertlik değerleri, element bileşimleri ve dağılımları detaylı olarak tarif edilmektedir. Ayrıca, mekanik karakterizasyonu teorik olarak bize mekanik uygulamalar için geçerli olan elastik modülünü ve ürün güçlendirmeyi belirlemeyi sağlar. Buna ek olarak, Y yerine Ho ve Ba yerine Nd katkılı Y-123 malzemelerde yüke bağlı sertlik değerleri, günümüze kadar olan mevcut teorik yöntemlerle (Hays-Kendall ve uyarılan çatlak tanımlama yaklaşımı) modellenmemiştir. Ho ve Nd katkılamaları ile ilgili tüm deneysel bulgular, mikro yapısal, elektriksel, mekanik ve süper iletkenlik özelliklerinin YHo örneklerinde optimum x=0,100'e kadar Ho artışı, YNd örneklerinde optimum y=0,250'ye kadar Nd artışı ve HcN (Ho sabit+Nd değişken) örneklerinde optimum y=0,100'e kadar Nd artışı ile düzenli olarak geliştirildiğini, bu optimum değerlerin ötesinde ve NcH (Nd sabit+Ho değişken) örneklerinde tüm Ho artışlarında ise özelliklerin hızla kötüleştiğini göstermektedir. Yani, aşırı Ho ve Nd penetrasyonunun yukarıda belirtilen önemli özelliklere zarar verdiğine atfedilir.

Ayrıca, tüm örnekler uygulanan belirli test yükleri altında tipik ters girinti boyut etkisi davranışı (RISE) sergilerler. Örneklerdeki Vickers mikro sertlik ölçümleri plastik deformasyonun elastik deformasyondan daha önemli olduğunu gösterdi. Bu sonuçlara dayanarak, elde ettiğimiz tüm süper iletken örnekler için IIC modeli sertlik değerlerinin HK yaklaşımına göre daha uygun veya daha üstün olduğu görülmüştür.

Anahtar Kelimeler: X-ışını kırınımı, elektron mikroskobu, seramikler, sertlik ölçümleri, mekanik karakteristikleri, tanecik sınırlamaları.

This dissertation is devoted to my parents for their Patience, Support and Understanding...

ACKNOWLEDGEMENTS

I express my warm thanks to many people who have contributed to the completion of this thesis through their knowledge, guidance support and friendship. First of all, I would like to thank my thesis supervisor, Prof.Dr. Osman Gorur for his support, patience, guidance and encouragement throughout this thesis and also with my professional development. In particular, it is great fun studying with him on several important projects. I also want to thank my co-supervisor Prof. Dr. Cabir Terzioglu for useful conversation.

I am grateful to my thesis committee members, Dr. Mustafa Akdogan and Dr.Gurcan Yildirim, for their guidance and assistance through this process. Of course, their discussion, enlightening comments, ideas and especially feedback have certainly been invaluable to interpret and improve the results obtained. I learnt many things about superconductivity from their lengthy and useful conversations. I am thankful for their aspiring guidance, invaluably constructive criticism and friendly advice during the work. I am sincerely grateful to them for sharing their truthful and illuminating views on a number of issues related to the work.

I am appreciative of the aid from all my friends, especially , Lecturer Musa Dogruer, R.A Sevgi Altintas, Expert Nevin Soylu, being a great source of help on the issues associated with superconductivity, is of the enormous assistance with sample preparation and measurement.

I am very grateful to my parents: Mom, Dad and Sister for their love, moral support, and constant encouragement, throughout this study. I would like especially thank to my wife, Hatice and our children; Recep, Neval, being always here for me with their love, continued support.

TABLE OF CONTENTS

LIST OF TABLES

LIST OF FIGURES

CHAPTER 1

INTRODUCTION

The usage of superconducting materials facilitates the daily life of human beings due to the remarkable properties such as rather smaller power losses, extremely higher current and magnetic field carrying capacity, lower material cost, simpler chemical composition, easier availability of the starting chemicals, greater performance (lesser energy loss and dissipation), optical and electronic properties [1–3]. Moreover, the different attractive and feasible applications such as the future hydrogen society, innovative energy infrastructure, effective utilization of renewable energy, global electric power network, combination with optics and spintronics (magneto electronics: the information storage and transfer using the charge of electrons with their own spin states), innovative superconducting electric power cable make the researchers study on the superconducting compounds. Nowadays among the superconducting parents, the high-temperature cuprate superconductors (especially YBaCuO family) are apt to the engineering and technological applications because of extremely high critical transition temperature value (above liquid nitrogen temperature) [4–9]. YBaCuO with the major phase of Y-123 obtains a perovskite structure with bended Cu–O chains providing the extra performance for the strong flux pinning capability in high magnetic field [10, 11]. However, the new era brings more needs and charges for the introductions of advanced power equipment. Thus, the materials used in the engineering, industry and technology

applications need to be updated rapidly to keep pace with nowadays technological trends. For example; the improvement of the superconducting properties as well as the mechanical characteristics of the poly-crystallized Y-123 superconductors allows the materials to use in the application-oriented material research and large scale applications such as power transmission cable, generators, motors, transformers, superconducting magnetic energy storage, magnetic resonance imaging, accelerators, fusion and fault current limiter technologies [12–16].

YBCO superconductor ceramics incorporate the first material discovered to become superconducting above the liquid nitrogen temperature. From the literature, Cu-O planes play the most important role in the superconductivity of the YBCO materials as a result of the fact that the crystal structure, electron/hole transport and superconducting properties of the compounds vary with respect to the oxygen content [11]. Having some beneficial properties as regards simple chemical composition, easy availability of the starting powders, low material cost, simplicity of the synthesis procedure, high T_c and J_c value, high applied magnetic field capacity, low resistivity about critical temperature, non-poisonous characteristics as compared to Tl and Hg-based superconductors, the YBCO superconducting materials are progressively the center of the interest in technology, engineering and industry applications [17]. Hence, researchers have been exerted an effort to enhance the effective pinning centers such as planar defects, stacking faults and micro-defects with the aid of methods regarding the chemical doping, substitution, transition metal evaporation and changing preparation condition including the annealing ambient, operational procedure, composition, heat-treatment, dopant type and quantity [18–21]. In substitution process, the variation of some significant superconducting characteristics (critical current density, onset and offset critical temperatures, etc.)

pertaining to the YBCO samples is related to the information about both the location and charge of doping metals. In other words, this technique is the most efficient way to access some crucial clues obtained about the mechanism of high-temperature superconductivity [17].

In the present work, the experimental evidences deduced from the bulk density, dc resistivity, transport critical current density, X-ray diffraction, scanning electron microscopy, Electron Dispersive Spectroscopy and Vickers microhardness measurements declare that the optimum level of Ho, Nd and co-doping (Ho+Nd) inclusions inserted in the Y-123 superconducting matrix not only improve the fundamental characteristics of the material but also favor the usage in the large scale applications. The long and short of it is that this study cooperates between the fundamental material science and engineering (especially mechanical and electrical) and in fact may be pioneering survey to provide the new market areas for the universe economy.

"Superconductivity" is the property of exactly no resistance to electric current and expulsion of magnetic fields occurring in certain materials when cooled below a critical temperature. Superconductors have excitations such as phonons and electron-like or hole-like excitations [22]. In conventional superconductors, electrons are found in Cooper pairs by an attraction mediated by lattice phonons. In high-temperature superconductivity, there are two main assumptions as the resonating-valence-bond theory and spin fluctuation [23].

The second hypothesis proposed that electron pairing in high-temperature superconductors is mediated by short-range spin waves known as paramagnons.[24, 25].

The superconducting properties of material are summarized as following;

(i) Zero electrical resistance or zero potential below the critical temperature (T_c).

(ii) This zero resistance is demolished by the application of magnetic fields when the flux density exceeds a critical value, B_c.

(iii) The superconductor ejects magnetic flux from its interior when cooled below T_c in a magnetic flux density less than B_c (the Meissner effect) [26].

If three critical parameters in Figure 1.1; critical temperature (T_c), critical current density (J_c) and critical field (H_c) are not overdone, a material will carry on in superconducting state. Although T_c is material dependent, both J_c and H_c are material and temperature dependent. They are both zero at the critical temperature and they rise as the temperature is reduced. Above critical temperature, the superconducting metals or alloys behave as a normal conductor [27].

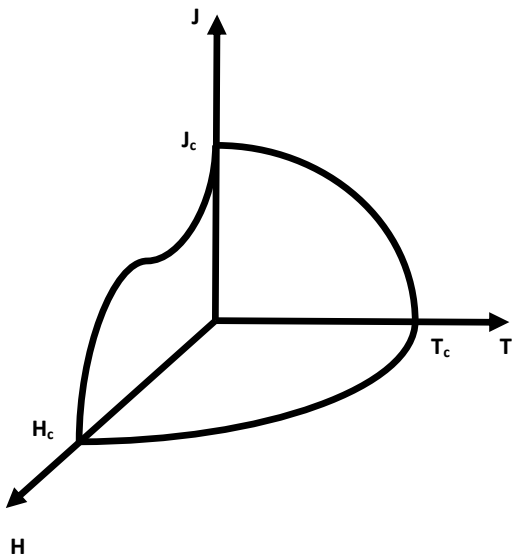

Figure 1.1: Critical surface diagram for Type II superconductors

In Type I superconductors, superconductivity is sharply destroyed when the strength of the applied field rises above a critical value Hc. In Type II superconductors, rising the applied field above a critical value H_{c1} leads to a mixed

state in which an increasing amount of magnetic flux penetrates the material, but still the material can carry resistanceless current as long as the current is not too large (below critical current, I_c). At a second critical field strength H_{c2}, superconductivity is totally destroyed (See Figure 1.2). The mixed state is actually caused by vortices in the electronic superfluid, sometimes called "fluxons" because the flux carried by these vortices is quantized. In Figure 1.3, the variation of applied external magnetic field (H) with critical temperature (T_c) for Type I and Type II superconductors are shown.

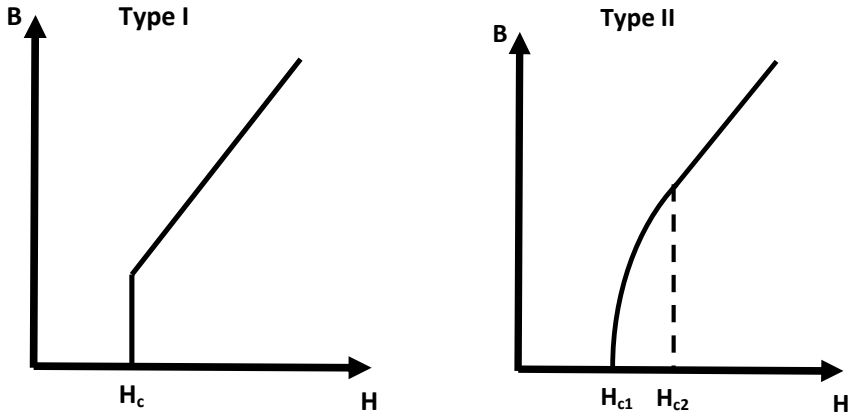

Figure 1.2: Variation of internal magnetic field (B) with applied external magnetic field (H) for Type I and Type II superconductors

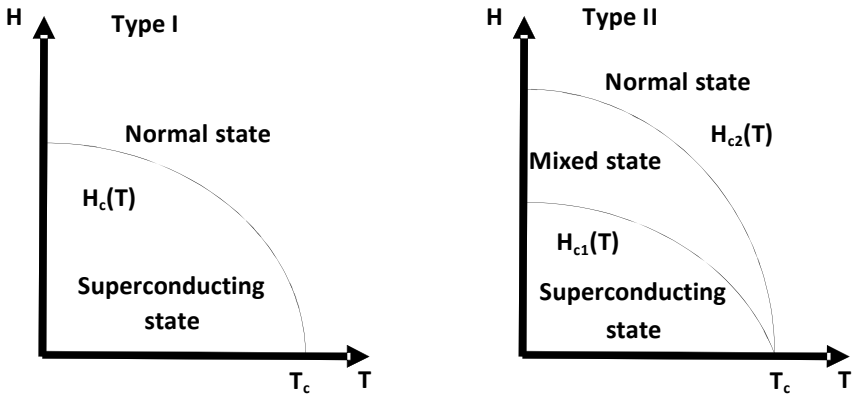

Figure 1.3: Variation of applied external magnetic field (H) with critical temperature (T_c) for Type I and Type II superconductors

The critical current density (J_c) of bulk ceramic superconductors is often several orders of magnitude lower than that of a single crystal or oriented film of the some material due to the weak links residing of the grain boundaries between single crystals within the ceramic sample [28]. High values of J_c can be raised in Type II materials by introducing high density structural defects; such as normal precipitates, grain boundaries and dislocations [27].

Kammerlingh Onnes' [29] discovered that electrical resistance of mercury abruptly disappeared near the absolute zero of temperature; explicitly close to 4 K. Walter Meissner and Robert Ochsenfeld [30] discovered that a superconductor repels a magnetic field in 1933. This phenomenon is known as the "Meissner effect" [31]. Circulating super currents flowing in the surface create magnetic field. A magnetic field opposing the applied field is created so that B=0 (M=H) inside the material and all magnetic flux is expelled. This behavior is called Meissner effect. In other words, the superconductor shows perfect diamagnetism that is the ability of a superconductor to protect its interior from an applied magnetic field. In 1934, Gorter offered an important idea of a two-fluid model where the electron gas within the superconductor obtains two compounds. One of them carrying the super current has no entropy whereas the other compound behaving like a normal electron gas has all the entropy [32]. Furthermore, in this idea, the superconducting electrons short out the normal electrons below the superconducting transition temperature; hence, the electrical resistance for the material goes to zero. After a year, Fritz and Heinz London carried out an important theoretical analysis of the response of a superconductor in the presence of an applied magnetic field [33]. The theory showed that a bulk superconductor exhibits both perfect conductivity and diamagnetism. With the aid of the Maxwell's equations, both predict that the magnetic flux

generated is excluded from all body expect for the surface region of the superconducting material. When a superconductor is in the Meissner state the applied field does not suddenly drop to zero at the surface, but instead decays exponentially to zero over a distance called the penetration depth, λ. After the critical field, H_c is exceeded, magnetic flux completely enters and the material converts normal.

Another important property of superconductor is the presence of a coherence length (ξ). This is the range of interaction between Cooper pairs to form the superconducting state as a quantum mechanical phenomenon. The Ginzburg Landau parameter (κ) is ratio of penetration depth (λ) to coherence length (ξ); ($\kappa=\lambda/\xi$). If κ is greater than 0,7, complete flux exclusion is no longer favorable and flux is allowed to penetrate the superconductor through cores known as vortices [34].

The coherence length is the range over which the interaction binding a pair of electrons together operates. In type I superconductors the coherence length is large $\xi \gg \lambda$. Impurities (like in alloys) cut down on the coherence length which is much smaller than the penetration depth ($\xi \ll \lambda$) for Type-II superconductors and is also temperature dependent [26].

The very short superconducting coherence lengths of the oxide superconductors make their electrical and magnetic properties extremely sensitive to microstructural inhomogeneity thus placing stringent requirements on the quality of grain boundaries [35].

In BCS theory, electrons become paired through an attractive interaction with a vibrating positive ion leading to a reduction in energy and the formation of an energy gap. As the electron pair (called a cooper pair) is in a lower energy state it can only be scattered if the cooper pair receives enough energy to break the pair up into single electrons. Below T_c and B_c this is energetically more favorable and the cooper

pairs which in motion through the crystal structure are unaffected by scattering sites such as impurity ions. This is the origin of the zero resistivity phenomenons in superconductors. The range of the electron-phonon interaction is described by the coherence length ξ, which may be thousands of atomic spacing in conventional superconductors. [27]

One of the most remarkable features emerging from BCS theory is the existence of an energy gap between the BCS ground state and the first excited state. The energy gap is nothing else but the energy needed to break up cooper pairs. If the magnetic field is strong it will be energetically favorable to break up the cooper pairs and align electron spins parallel to each other. It is the minimum energy required to create a single-electron (hole) excitation from the superconducting ground state. Thus the binding energy of a Cooper pair is two times this energy.

The phenomenon of electron tunneling in superconductors is a process arising from the wave nature of the electron. It occurs because of the transport of electrons through spaces that are forbidden by classical physics because of a potential barrier. The tunneling of a pair of electrons between superconductors separated by an insulating barrier was first discovered by Brian Josephson in 1962 [36].

Superconducting magnets are used in MRI/NMR machines, mass spectrometers, and the beam-steering magnets used in particle accelerators. They can also be used for magnetic separation, where weakly magnetic particles are extracted from a background of less or non-magnetic particles, as in the pigment industries.

In the 1950s and 1960s, superconductors were used to build experimental digital computers using cryotron switches. More recently, superconductors have been

used to make digital circuits based on rapid single flux quantum technology and microwave filters for mobile phone base stations.

Superconductors are used to build Josephson junctions which are the building blocks of SQUIDs (superconducting quantum interference devices), the most sensitive magnetometers known. SQUIDs are used in scanning SQUID microscopes and magneto encephalography. Depending on the particular mode of operation, a superconductor-insulator-superconductor Josephson junction can be used as a photon detector or as a mixer. The large resistance change at the transition from the normal to the superconducting state is used to build thermometers in cryogenic micro-calorimeter photon detectors. The same effect is used in ultrasensitive bolometer made from superconducting materials.

Other early markets are arising where the relative efficiency, size and weight advantages of devices based on high-temperature superconductivity outweigh the additional costs involved.

Promising future applications include high-performance smart grid, electric power transmission, transformers, power storage devices, electric motors (e.g. for vehicle propulsion, as in vactrains or maglev trains), magnetic levitation devices, fault current limiters, nanoscopic materials such as buckyballs, nanotubes, composite materials and superconducting magnetic refrigeration. However, superconductivity is sensitive to moving magnetic fields so applications that use alternating current (e.g. transformers) will be more difficult to develop than those that rely upon direct current [37].

In this paper we will make an effort to present an outline of structural studies of different YBCO related materials. Most materials investigated here are obtained by inclusion of one of the YBCO components. We will think about the

partially substitution of Y by Ho and Ba by Nd from other rare earth elements and at the same time oxygen for vacancies.

As a result important development in superconductivity history is shown following Table 1.1;

Table 1.1: The important development in superconductivity history

1908	Helium is liquefied at 4,2 K
1911	The discovery of superconductivity or observation of vanishing resistivity ρ(R) at a critical temperature Tc ≈4,2 K in mercury (Hg) sample by H. Kammerlingh Onnes
1933	Finding the perfect diamagnetism of type I superconductors by W. Meissner and R. Ochsenfeld
1935	The first theory to explain the Meissner effect flux repulsion, London Theory
1950	The isotope effect for Hg, observed by Maxwell and suggested that the electron–phonon coupling might be responsible for superconductivity. Trying to explain superconductivity with quantum theory, Ginzburg-Landau theory
1953	Discovery of new V_3Si superconductor with a critical temperature of 17,1 K
1957	The most comprehensive theory "BCS Theory" explaining superconductivity proposed by J. Bardeen, L.N. Cooper and J.R. Schrieff
1961	Experimental verification of the quantized flux that signal of the presence of cooper pairs
1962	Tunneling of a cooper pair through a thin insulating oxide layer is provided theoretically by B.D. Josephson
1974	Obtaining the maximum critical temperature (23,2 K) in the films of the sputtering Nb_3Ge
1986	The discovery of superconductivity at 30 K temperatures in La-Ba-Cu-O system by J.G. Bednorz and K.A. Müller
1987	The discovery of superconducting property of $YBa_2Cu_3O_{7-\delta}$ with 92 K by Paul Chu et al. at the University of Houston
1993	The discovery of $HgBa_2Ca_2Cu_3O_{8+\delta}$ superconductor with a critical temperature of 135 K
2001	Magnesium diboride (MgB_2 having a critical temperature of 40 K) and non-oxides compounds was discovered by J. Akimitsu et al

An almost trivial substitution is that of oxygen by vacancies in the composition range $1 \geq \delta \geq 0$. All oxygen substitutions only have an effect on the CuO layer configuration. As a function of the oxygen deficiency different orthorhombic superstructures, termed Ortho I (δ=0, T_c=92 K, orthorhombic), Ortho II (δ=0,25, T_c=60 K), Ortho III ($\delta \geq 0,5$, T_c=25 K, tetragonal), etc. have been reported [38, 39], most of them first discovered by electron diffraction. For some time a discussion has been going on concerning the relationship between these superstructures and the behavior of T_c as function of oxygen content. We will give

some more arguments with respect to this problem by substituting Y and Ba in YBCO by rare earth ions of different size [40].

CHAPTER 2

HIGH-TEMPERATURE SUPERCONDUCTORS

2.1 Introduction

After the discovery of superconductivity in mercury at 4 K, scientists investigate to get a new material that shows superconductivity at higher temperatures for nearly 75 years and development of critical temperature in time is seen in Figure 2.1. As a result of research, only a few metals, alloys and a group of ceramic materials with only a maximum of 23 K, T_c (Nb_3Ge alloy in1973) were found up to the eighties.

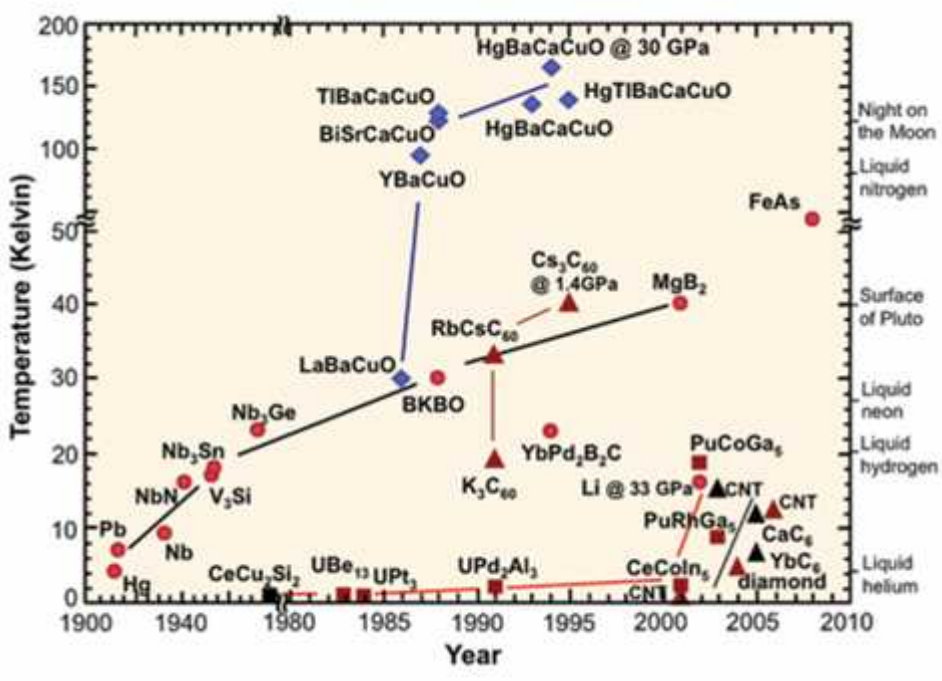

Figure 2.1: Development of critical temperature in time [41]

In different theoretical expectations, the maximum critical temperature was believed to be a maximum of 30 K in superconductors effected electron lattice interactions. Nevertheless these hypotheses was false, because Bednorz and Muller found new oxide ceramic superconductor in (La, Ba)$_2$CuO$_4$ with 35 K as a critical temperature in 1986. Thereafter, 1986 was considered as the beginning of the work on the high temperature superconductivity (HTS), a new HTS oxides was begun to be revealed fast. The research groups (Paul Chu et al.) at the Alabama and Houston University observed superconductivity at around 92 K as a mixed phase of Barium, Yttrium, Copper ($YBa_2Cu_3O_{7-x}$) oxygen in 1987. In this area this is the most important event because it became possible to use liquid nitrogen as a coolant and they superconduct at significantly higher temperatures than conventional superconductors. After that many new compounds and compound class were found within 12 months. From among them, BSCCO ($Bi_2Sr_2Ca_2Cu_2O_{8+x}$ (Bi-2212), T_c with 85 K, $Bi_2Sr_2Ca_2Cu_2O_{10+x}$ (Bi-2223), T_c with 110 K, a different phase of the BSCCO compound and $Tl_2Ba_2Ca_2Cu_3O_{10}$ compound, T_c with 127 K showed superconductivity have been the most studied and used materials. A portion of these materials are similar to a maximum of three copper-oxide material as plane owners 1-2-3 separated by bismuth and thallium oxide plane. However, all known superconductors (T_c>50 K) are perovskite (cubic, tetragonal or orthorhombic structure) copper alloy superconductors.

Today, the maximum critical temperature record of HTS is 133,5 K at low pressure and 164 K under 30 GPa pressure for $HgBa_2Ca_2Cu_3O_{8+x}$. A higher transition temperature could not be reached since 1993 but the new HTS compounds have continued to be obtained like $Ba_2Ca_{3-y}Cu_{3+y}O_x$ with T_c=127 K, MgB_2 with T_c of 40 K and field-induced C_{60} with T_c=117 K, $CaCuO_2$ with T_c=89 K [42].

The type II superconductors are preferred to use for applications since they have higher Tc values and remain superconductors in much higher magnetic fields than a type I superconductor [43].

2.2 Structural properties of high temperature superconductors

Many of the new high T_c materials are copper oxide compounds. Until now, the different superconducting compounds examined in detail can be classified in terms of crystal structure called perovskite in Figure 2.2.

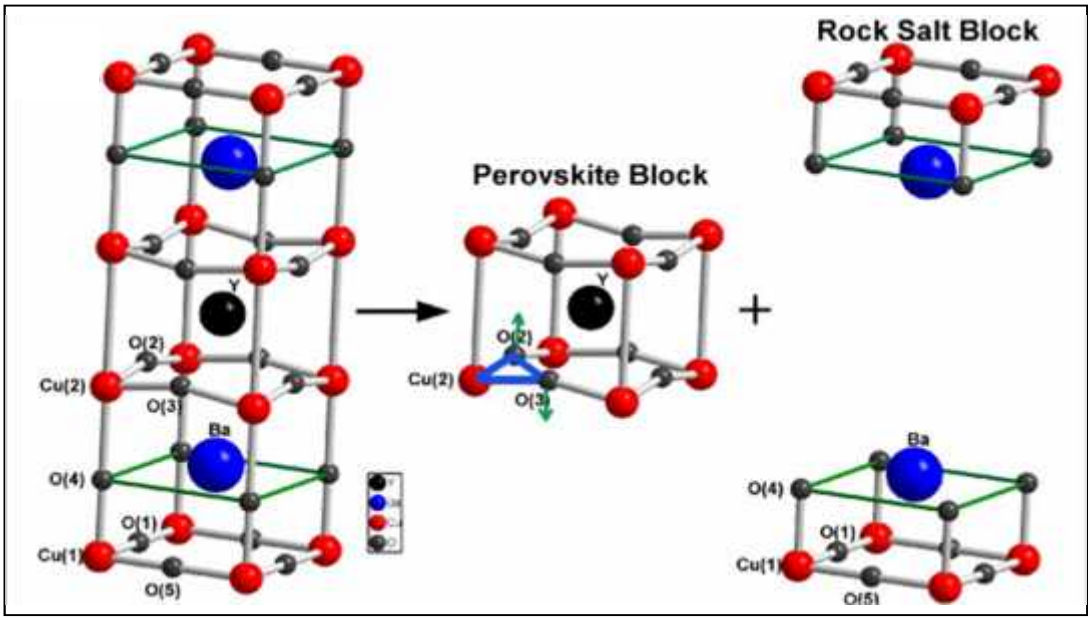

Figure 2.2: A block model (dividing the structure of a high-T_c superconductor into perovskite and rock salt blocks. The blue triangle shows the 'fixed triangle' on the boundary of the perovskite and rock salt blocks. The green arrows illustrate the opposite movements of O (2) and O (3) as the doping content varies) [44]

The first classes are $BaPb_{1-x}Bi_xO_3$ cubic perovskites (a=b=c). As it is known as one of first high T_c materials, transition temperature is 10 K. $KNiF_4$ is known as second class with tetragonal structure (a=b≠c) in Figure 2.3.a and single-layered perovskites. $La_{1,85}Sr_{0,15}CuO_4$ (T_c with approximately 38 K) is an example of this

class. Here, a and b lattice constants are measured in the oxygen plane and c is perpendicular to this plane. Third class are multi-layered perovskite like $YBa_2Cu_30_7$ (T_c=92 K) with orthorhombic structure (a≠b≠c) (Figure 2.3.b). Metal compounds of this class due to their relative proportions are sometimes referred to as the 1-2-3 material.

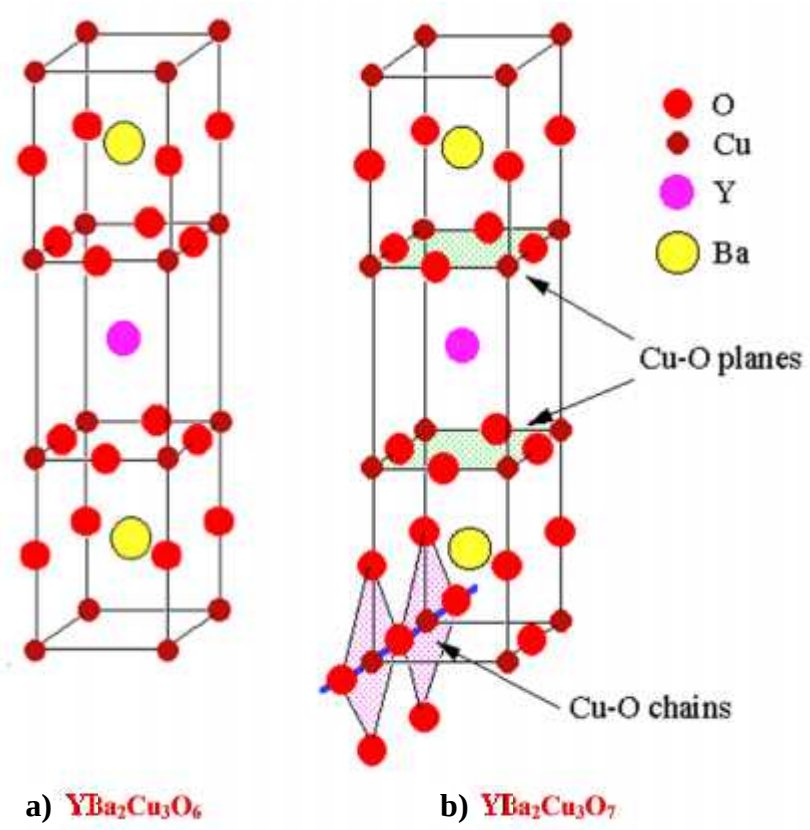

Figure 2.3: Comparison YBCO structures: a) Tetragonal structure of YBCO (insulator), b) Orthorhombic structure of YBCO (superconductor) [45]

Crystal structures of these materials are described multi-layered perovskite structures with CuO_2 plane and missing-oxygen in Figure 2.4. They are always a strong anisotropy in other words they possess the direction sensitivity in superconductivity properties. Active supercurrent flows through interconnected CuO_2 planes (a-b planes of unit cell) with Josephson Coupling. However the conductivity in the direction of the c-axis is poor. Carrier density of HTS ($10^{21}/cm^3$)

is twice as much of elemental low temperature superconductor (LTS). Coherence length of HTS is smaller than the LTS and it varies according to the direction of the plane. It is approximately 3 Å perpendiculars to CuO_2 plane and 10 Å along the plane. The coherence length describes the maximum distance between two coupled electrons, known as cooper pairs. If the paired electrons are separated by more than the coherence length, they no longer “communicate” with one another and they cease being a pair. Supercurrent cannot flow without cooper pairs. As a result, the maximum supercurrent is high in copper-oxygen plane and very low perpendicular to this plane. The copper alloys have a critical magnetic field with 150 T (a million times of Earth’s magnetic field) for the perpendicular direction to CuO_2 plane [42].

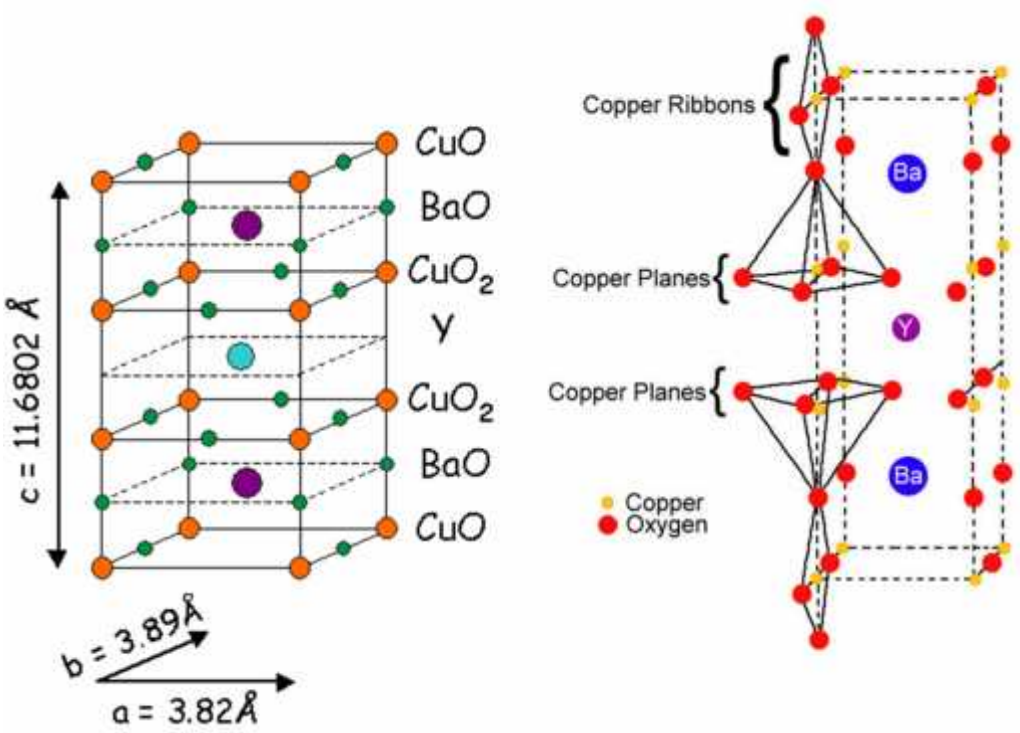

Figure 2.4: $YBa_2Cu_3O_7$-crystal structure of superconducting unit cells [46, 47]

The average size of grains is very important feature for metal. For example, smaller grain size raises tensile strength and tends to raise ductility. A larger grain size is desired for enhanced high-temperature creep properties. Creep is the

permanent deformation that increases with time under constant load or stress. Grain boundary energy increases with increasing misorientation [48]. The maximum current density decreases exponentially as a function of the misorientation angle of the adjacent grains. Like in any other material, grain boundaries in high temperature superconductors are formed by the integration of dislocations into the grain boundary plane [49, 50]. The boundaries parallel to the a-b planes are generally coherent and accommodate misorientations through the formation of edges; on the other hand the boundaries normal to the a-b planes are generally incoherent and exhibit structural disorder [51]. In dirtier grain boundaries, there may be impurities; there may be changes in the charge density, or deficiencies of oxygen [52].

High temperature superconductors are granular in nature and the transport critical current density depends on both intra granular and the intergranular network. In fact grain boundaries are known to act as pinning sites. On the other hand, HTS materials are plagued with grain boundaries that can act as “weak links” to the current flow and limit the performance in a magnetic field [53]. Grains are connected by Josephson junctions, implying the presence of so called “weak links” between grains which can be more than a few nanometers thick [35]. The superconducting coupling at grain boundaries was basically characterized by weak links. These weak links were closely related to the values of transport J_c and normal-state resistivity. The weak link behaviors at grain boundaries were dependent strongly on annealing and cooling conditions [54]. The nature of strong and weak links is that most of the weak links are twist boundaries, and that the strong links are mostly low-angle tilt boundaries [55]. In standard polycrystalline high-T_c compounds the critical currents are limited by the grain boundaries. To increase the critical currents, two strategies have been found. These strategies are based on

enhancing the critical current density of the boundaries. The first consists in aligning the grains along all major axes to within few degrees. This approach utilizes the fact that the grain boundary critical current density is a strongly decreasing function of the misorientation angle, is increased from 0^o to 45^o. Second for a given misorientation angle, the grain boundary critical current density is increased by appropriate doping [56]. Microcracks can form particularly at grain boundaries of polycrystalline materials [57].

Y-Ba-Cu-O, Bi-Sr-Ca-Cu-O and Tl-Ba-Ca-Cu-O systems typically exhibit very anisotropic grain shapes indicative of grain boundary energy anisotropy and/or growth rate anisotropy. It is well-known that there is a transition in transport properties as the misorientation angle of grain boundaries in YBCO increases. At low misorientation angles, grain boundaries are strongly coupled, becoming weak links at higher misorientation angles, and then suffering a strong reduction in critical current density, especially in high magnetic fields.

Thin film and bulk bicrystal grain boundaries in $YBa_2Cu_3O_7$ exhibit a strong dependence of critical current density, J_c, on misorientation angle. J_c in bulk is 30 times smaller than J_c in thin film [58].

The defect structures in the materials are likely to be very complex and are important because of the role play in the superconducting properties. In YBCO, grain boundaries have detrimental effect on the critical current, and twins have been shown to act as weak flux pinning centers. The density of all stacking defects is very sensitive to the composition and thermal processing of the sample [59].

The ceramic sample is made of many small grains with different orientations, when the sample was squeezed under high pressure; the force was exerted on the grains by the edges of other grains. If the grains are aligned by

stacking the platelets like a structure of bricks elongation of the sample caused by pressure application results in lower angles between the grains. This mechanism is effective because of plate-like nature of the microstructure. On the other hand, the grain alignment of the partially melted samples exists only in their surface layers [60, 61].

The characteristics of grain boundaries lying in the low-angle to high angle crossover regime in thin film and bulk scale YBCO and bulk BSCCO-2212 bicrystals have been studied. Such grain boundaries can be considered as periodic or quasi-periodic structures consisting of grain boundary dislocation barriers separated by channels of strong coupling [36].

High-angle grain boundaries are boundaries of rather high surface energy. High-angle grain boundaries can be minimized and crystallographic alignment of grains parallel to the a-b conduction plane produce a better path for the transport current resulting in higher J_c values [27]. The crystal coherence and connectivity at grain boundaries, including high-angle grain boundaries, were generally much higher for the melt-processed materials then for sintered materials. The high crystal coherency may have been achieved by a facet structure or by the cross orientation of the grains themselves. These types of grain boundaries are strongly coupled and thus are not easily penetrated by an applied field [36].

Flux creep is a major concern in these materials, since it limits high T_c superconductor's performance at temperatures above about 30 K. As is well known these properties are strongly influenced by the high-T_c superconductor microstructure. The level of current transport in a given high T_c superconductor depends upon several intrinsic microstructure-property relationships. In the typical orthorhombic crystal structure, supercurrent flows primarily in the a-b planes. In

polycrystalline materials, superconducting current drops off as grain boundary misorientation increases. High current densities in polycrystalline materials need strong c-axis alignment where current is expected to flow through these grains connected by low-angle grain boundaries. When a magnetic field is applied, the flux vortices may shift due to the force from the current or to thermal activation, resulting in a loss of superconducting properties known as flux creep. Flux vortices can be pinned by microstructural defects such as grain boundaries, impurity atoms or dislocations [62].

HTS materials are ceramic oxides and like many other ceramics they are brittle. To improve mechanical properties, HTS oxides are often combined with a metallic material (sheath, substrate, etc.). The metal is also needed to add stability to the conductor, especially thermal stability. Choosing a metal that fits the processing route and is chemically compatible with the superconductor is often a challenge. It is chemically compatible and with the proper mechanical deformation and heating c-axis orientated grains can be grown [63].

Each Cu atoms in the copper plane is bounded the six oxygen atom and the transmission is called p-type in $YBa_2Cu_3O_{7-\delta}$ and $Tl_2Ba_2CuO_{6+\delta}$ compounds. Each copper atom in the $Nd_{2-x}Ce_xCuO_{4-\delta}$ compound of a superconductor is connected to four oxygen atoms so it is known as n-type superconductor.

Superconductivity in the hole-doped copper alloys is induced by insulating antiferromagnetic sources and the hole-doped causes higher Tc than electron-doped. Doping can be performed by various methods like chemical substitution, insertion or reduction. The most common methods used in among them are chemical doping in charge reservoir part. Chemical doping is made occasionally in the active block. It is assumed that superconductivity happens in CuO_2 layers in this active block.

2.3 General properties of YBCO

Among the high temperature superconductors, YBCO synthesized first and still is one of the most widely studied materials. As seen from the figure 2.2, each of the perovskite (ABO_3) unit cells of YBCO are separated by a plane of yttrium atoms and includes two $Cu0_2$ plane sandwiched between two BaO layers. All HTS have a CuO_2 layered structure which played a decisive role in the characters of superconductivity. Other layers in the structure acts as reservoirs to regulate the charge density in the $Cu0_2$ planes, the carriers move only in the $Cu0_2$ plane. From the literature, Cu-O planes play the most important role in YBCO superconducting system [64], the crystal structure, electron/hole transport and superconducting properties of the material varies with respect to the oxygen content [11]. Superconducting transition temperature T_c of the $YBa_2Cu_30_\delta$ (Y-123) material depends on the oxygen content and moving carrier density (n) or the active Cu-valence charge in $Cu0_2$ plane. As oxygen has such a critical effect on the superconducting properties of YBCO, it is usually necessary to anneal this material in an oxygen atmosphere as a final stage in any processing treatment [57].

YBCO has two symmetry (tetragonal or orthorhombic), depending on the amount and distribution of oxygen in the Cu-0 layers. As seen from the figure 2.3, there are two kinds of copper atoms in structure. Two valence electrons of them (Cu^{++}) are connected by four oxygen atoms (square), others have the five oxygen atoms (like a pyramid) in Figure 2.4. Crystal lattice is orthorhombic structure with lattice parameters a=0,382, b=0,389 and c=1,168 nm and Pmmm/4 crystal symmetry. However, these materials, subjected to heat treatment in oxygen-free environment, lost one of the oxygen atoms; they are turned to $YBa_2Cu_3O_6$ insulator in a similar

structure, but are very different in character. Crystal lattice has turned into the tetragonal form because the electrons are detached from quadratic CuO_4 chain.

Exchange of oxygen and oxidation states of Cu has an important role on behavior of superconductivity of these compounds. For example, oxygen content (or hole), oxidation states of copper in different compounds and temperature of superconductivity can be summarized as follows (Table 2.1).

YBCO enters superconductor class in the type II such as other high-T_c superconductors. Instead of the necessity of the use of energy to the exclusion of the magnetic field in this structure, a magnetic field is surrounded by supercurrent, and is trapped inside the vortex flux tubes.

Table 2.1: The copper-transition temperature for different phases of YBCO

Compound	$C^{+3}/Cu^{+2}/Cu^{+}$ (rate)	T_c(K)
$YBa_2Cu_3O_7$	1/2/0	~95
$YBa_2Cu_3O_{6,75}$	0,5/2,5/0	~60
$YBa_2Cu_3O_{6,5}$	0/3/0	~25
$YBa_2Cu_3O_6$	0/2/1	Insulator

The interface energy between YBCO and normal regions is negative and therefore the coherence length (ξ) is smaller than the penetration depth (λ). Accordingly, the grain boundary in order to act as weak links, its magnitude must be sufficient in size. This is considered as description of the current density to be relatively smaller in high T_c bulk ceramic superconductors.

Structure of superconductors with copper-oxide layer gives permission to strong anisotropy [65]. As given in Table 2.2, this anisotropy is resulted in differences in some physical parameters on a-b plane and parallel to the axis c in YBCO.

Table 2.2: Physical parameters of $YBa_2Cu_3O_{7-\delta}$

$\xi^{ab}(0)$=15 Å	$\xi^{c}(0)$=3-5 Å
$\lambda^{ab}(0)$=100-140 nm	$\lambda^{c}(0)$=500-800 nm
$J_c^{ab}(0)$(depairing)=3-12x10^8A/cm^2	$J_c^{c}(0)$(depairing)=5-25x10^7A/cm^2
$\mu_0 H_{c1}^{ab}(0)$=2-23 T	$\mu_0 H_{c1}^{c}(0)$=8-9 T
$\mu_0 H_{c2}^{ab}(0)$=230-624 T	$\mu_0 H_{c2}^{c}(0)$=70-122 T

YBCO has numerous advantages compared to other ceramic superconductors. It is a single quaternary compound with greater than the critical temperature of 77K.

• It does not contain toxic elements or unstable compounds. For example; thallium is highly toxic and bismuth is in short supply, so both materials may be of greater scientific than technological importance [66].

• Single-phase YBCO is relatively easy to prepare.

• It possesses lower anisotropy than other HTS materials and can have higher current densities in stronger magnetic fields.

Also there are YBCO-124 phases with 80K and YBCO-247 phases which have 50K transition temperature. The two phases are not obtained in normal conditions. In other words, they need relatively high oxygen pressure or the alkali metal compound at normal pressure in air. Oxygen quantity is constant in the structure of $YBa_2Cu_4O_8$ (Y124).

2.3.1 Crystal chemistry and ion implantation-displacement effects

Copper oxide perovskites in simple construction are not metals but insulator. And just when creating more complex crystal structures (doping), they act like metal and show the probability to be the superconductor.

Cation substitution and oxygen-doped high-temperature superconductors' properties have been studied in detail since 1987. When

physical (temperature dependent resistance, transition temperature, hall effect, etc.) and structural properties of high temperature copper alloys are generally compared with elemental superconductors, they show difference as a function of doping. And a small change in the physical structure with implantation and induced ion defects has shown that an efficient change occurs in the electronic structure of these materials. This is the biggest indicator; they are different from elemental superconductors. Atomic displacement or doping effects of the copper alloy superconductors details are not fully understood yet, and this shows active area of research.

While investigating the contribution of foreign atoms, the oxygen content should be checked. Because the amount of oxygen affects the number of carriers in the CuO_2 plane and determines the critical temperature value.

Doping of such superconducting materials by isomorphous substitution of aliovalent ions and studying the effect of doping on the superconducting properties has proved to be a successful method to get information on the structural requirements for the occurrence of superconductivity and it lets us optimizing its properties [67]. $YBa_2Cu_3O_7$ is extremely tolerant in accepting various substitutions without greatly modifying its structural features, even though the superconducting properties may be severely changed [68]. An important result of all these experiments is that the structural integrity of the $Cu0_2$ layer seems to be essential for the incident of superconductivity [69]. The stoichiometry and the dopant atoms in the CuO-layer are important in determining the number and the type of charge carriers [70].

Doping studies on the chemistry of YBCO in obtaining accurate data has been quite helpful. Amount of the hole in lattice can be controlled by the

doping. For example, when La^{+3} ion doped instead of Ba^{+2} ion, the amount of hole decreases and the critical temperature (x=0,05) increases to 94 K. Ionic radii, valence electrons, the region of doping, electron configuration and magnetic structure are the main factors affecting the results in doping.

There are basically two reasons of the doping views in YBCO. The first of these is the change in material properties and thus to obtain more information about the possible superconductivity mechanism. Second is to improve physical properties such as brittleness, grain structure and the material's density. YBCO-123 compound is well-adjusted both anionic and cationic doped. Indeed many chemical elements including actinides and noble gas have been found to enter the structure in a certain amount.

2.3.2 Doping to the yttrium region

2.3.2.1 With lanthanide

Lanthanum is the first element in third transition series. And in this group elements (La, Ce, Pr, Nd, Pm, Eu, Gd, Tb, Dy, Ho, Er, Tm, Yb, Lu) possess the 2 and 14 counts ranging electrons in 4f orbit. As all of them show the $^{+3}$ oxidation state like Y, at the same time Ce, Pr and Tb can become stable $^{+4}$ and Nd, Dy, Tm, Eu, Sm and Yb can become stable $^{+2}$ oxidation. An ionic radius of Y in 8-fold coordination is 1,015Å. Also, they have radii ranging from 1,18 Å for La to 0,97 Å for Lu.

Generally, Ce and Tb due to the predominance of the stable tetravalent state are not doped Y and Lu is not completely interchanged with Y, due to small diameters of Lu.

For R=La, Pr and Nd, some substitution of R onto the Ba sites occurs [71], but this tendency decreases with decreasing size of the lanthanide. Thus, for x=0,25,

29% of La substitutes on the Ba site, but only 12% of Pr and 6% of Nd, with the remainder substituting on the Y site.

T_c values were changed by doping of these matters instead of Y, but if the lanthanides radius decreases, the critical temperatures reduce [72-74]. T_c increased with the amount of molar doping of Eu. Even Sm has a greater radius than Y; the critical temperature wasn't changed by Sm doping [75].

The structures of R-123 compounds are similar to those of YBCO, although tetragonal symmetry was proposed by Arabi et al. [76] for fully oxygenated Ho123. Pseudo-tetragonal symmetry is frequently observed in twinned orthorhombic crystals [77]. Gupta [78] proposed a fully ordered tetragonal structure for R-123, with chains forming in both *a* and *b* directions, giving 2-, 4- and 6-fold coordination for Cu(1).

In general, all R-123 phases with $\delta=7$ are orthorhombic; lattice parameters decrease linearly with decreasing rare earth elements (RE) size [e.g., Refs. [76-78], though the contraction is not isotropic [79]. The exceptions are Pr and La [74] which may imply an intermediate valence for Pr and site mixing of La and Ba. For O=6, powder neutron diffraction at 10 K showed tetragonal lattice parameters to decrease linearly with lanthanide size and La and Pr both fit the linear variation [63]. Bond lengths also decrease linearly with decreasing ionic radius, except for the Cu(1)-O bond length which remains approximately constant and the Cu(2)-O bond length which increases with decreasing ionic radius [65]. A similar variation of Cu(2)-O_{ap} with lanthanide ionic radius was observed by Currie and Weller [80] in a high resolution neutron powder diffraction study for R=Er, Ho and Dy.

The basic orthorhombic structure (Ortho I) is formed for the Y compound in the fully oxidized state $O_{7-\delta}$ (with $\delta=0$, all O(1) sites-filled and all O(5) sites-vacant). CuO chains are shaped along the b axis by ordering of oxygen atoms into sites along b in between every two Cu atoms of the square Cu lattice. The Ortho II phase has an ideal oxygen content of 6,75 (with $\delta=0,25$). In the Ortho II phase the oxygen atoms of every other copper-oxygen chain are absent; the unit cell doubles along the a-axis and therefore this superstructure is sometimes also called the $2a_0$ structure. The form of this superstructure is often associated to the presence of a plateau at about 60 K in the T_c versus oxygen content curve of well annealed samples [38, 39]. In the case of quenched samples no plateau is observed and the critical temperature decreases monotonically with increasing oxygen deficiency [81]. In such material, no or very ill defined Ortho II superstructures are detected [39].

A close relationship between the ion size of the substituted rare earth and the different structural and electronical properties of the material are established in different rare earth ions doped into Y-site [82]. Apart from a weak dependence of orthorhombicity on the ionic radius of the rare earth ion, a variation was observed of the width of the 60 K plateau. A well-defined plateau appeared for the smaller ions (Yb, Er, Y) while for the larger ions (Nd, La) no plateau was observed at all. Electron diffraction of these materials was carried out at 100 kV [83]. For the smaller ions, very clear and well defined extra Ortho II or $2a_0$ ordering reflections were detected in the [001] zone pattern. Best defined ordering happened at oxygen contents around $O_{6,6}$. Attempts to image the domains corresponding to such weak diffuse intensity failed in all cases.

In these measurements a clear correlation between the presence of the Ortho II structure and the presence of a 60 K plateau is established. This correspondence is further supported by experiments performed on Pr-doped samples [82]. The T_c of the lower plateau is only slightly affected by the doping and also the Ortho II superstructure is not affected. As a result an unambiguous correlation exists between the superconducting 60 K phase and the structural Ortho II phase.

2.3.2.2 Other $^{+3}$ valence ions

Studies on doping antimony into YBCO are made by percent weight. The critical temperature of the pure YBCO (T_c=92 K) is decreased by Sb doping. Important parameters that affect the tetragonal-orthorhombic phase transition are the heat treatment temperature and atmospheric conditions. Although, 5% Sb_2O_3 doping reduced critical temperature and grain size and porous structure was increased, the positive result was created for the critical current density [42]. Despite these negative effects, the cause of increasing the critical current density is strong coupling in grains boundary. The oxygen adsorption kinetics during tetragonal-orthorhombic transition is a further advantage of Sb_2O_3 doping.

Critical temperature is independent of x in compounds formed by Sc doping to the region Y. Also $Y_{0,75}Sc_{0,25}Ba_2Cu_3O_\delta$ compound has a T_c=92 K. T_c depending on increasing x ($0 \leq x \leq 0,85$) of $Y_{1-x}Al_xBa_2Cu_3O_\delta$ decreases from 90,6 K towards 50K [75].

2.3.2.3 With valent $^{+2}$ ion doping

Ionic radius of calcium (1,12 Å) is close to the radius of Y (1,015 Å) and is much smaller than the radius of Ba. However, doping of Ca with the divalent ions instead of Ba region can be expected. It is found that solubility of calcium is almost 0,2-0,25 in $Y_{1-x}Ca_xBa_2Cu_3O_\delta$.

While critical temperatures and the lattice parameters *a* and *c* are increased, b is observed to decrease with Ca doping.

Orthorhombic symmetry is conserved structurally throughout the solid solution although the orthorhombicity decreases with increasing Ca content attended by a decrease of order in the Cu-O chains

$Y_{0,9}M_{0,1}Ba_2Cu_3O_\delta$ (M=Mg, Ca, Sr, Ba) phases had shown that the critical temperature depended on ionic radii. The critical temperature is 95 K for M=Ba, 91,3 K for Sr, 87,7 K for Ca and 84 K for Mg. All samples of $Y_{1-x}Cd_xBa_2Cu_3O_\delta$ (x=0,1, 0,3, 0,5) have same T_c=92 K. Although it is the claim that there is the displacement in the Y-Cd, XRD results has emerged clearly that materials in a multiphase [75].

2.3.2.4 Doping with monovalents

Fever investigations were carried out in a monovalent ion implantation to Y. The ionic radius of Na with 1,16 Å is very close to Y but it is thought to lead to undesirable results. Potassium (K) is added to Y because ionic radius of K is larger than Y. For compound $Y_{1-x}Na_xBa_2Cu_3O_\delta$, T_c remains constant until x=0,2, and so then T_c is reduced to 42 K at x=0,5.

Impurity phase is not observed in the form of $Y_{1-x}A_xBa_2Cu_3O_\delta$, (A=K, Rb, Cs) to x=0,15, and unexpectedly, it is observed that the unit cell size remains

constant. Of these, the highest critical temperature material reached 95,5 K for $Y_{0,95}Cs_{0,05}Ba_2Cu_3O_\delta$ [75].

2.3.2.5 Different doped description

Furthermore, there are a few studies on the solubility of Bi like In. An orthorhombic distortion and T_c is decreased by doping Ga and Fe up to x=0,2. The solubility of Tl is 10% at 850 °C and 50% at 900 °C so this event shows the temperature dependence of Tl. Although Ca and Th are doped together, each of the implantation studies of Th and Zr has been unsuccessful [75].

2.3.3. Studies in doping to Ba region

2.3.3.1. Ba by lanthanum

The upper limit of La doping is x=0,36; while La can be replaced at the Ba site, Y is also partly substituted by La at higher levels. Unit cell parameters decrease with La content; a large reduction in *c* occurs, although there is different variations in *a* and *b*. The orthorhombicity is reduced, but with a slight maximum at $x=0,05$ and an O/T transition at $0,1< x < 0,25$.

Oxygen content in as-prepared samples rises with La content; critical temperatures decrease overall with La content but of course, also depend on oxygen content. At low x, the T_c increases by 2 K, attaining a maximum at $0,025 < x < 0,10$. This proves that $YBa_2Cu_30_7$ is overdoped. The normal state resistivity increases with x and undergoes a metal-semiconductor at $0,15< x <0,175$. There is a correlation between T_c and ε_T, where ε_T is a measure of the deformation of the unit cell.

2.3.3.2. Ba by other lanthanides and trivalent

Limited solubility of Pr for Ba was proposed, but Ce, Eu, Gd instead of R were found to substitute only at the Y site in solid solutions $Y(Ba_{1-x}R_x)Cu_3O_\delta$. The solubility was limited by oxygen content rather than ion size. No significant change happens in the unit cell parameters in Lu and Sc substitution for Ba.

2.3.3.3. Ba by strontium or calcium

The group IIA elements have ionic radii (for 8-fold coordination) of 0,89 Å (Mg), 1,12 Å (Ca), 1,25 Å (Sr) and 1,42 Å (Ba). Sr is the superconductivity at 65°C in the Y-(Ba, Sr)-Cu-O system. $YSr_2Cu_30_7$ (YSCO) can only be prepared at high pressures, ~7 GPa and there is introduction of dopant cations at the Cu(1) site.

In the non-superconducting samples, superconductivity can be restored by substitution of Ca on the Y site.

Transitions between the structures may occur, e.g., the structure for $YSr_2Cu_{3-x}Ga_xO_7$ is the tetragonal in rate of $(0{,}4 \leq x \leq 1{,}0)$, 123-type, with oxygen displacements for $0{,}4 \leq x \leq 0{,}7$, and orthorhombic for $0{,}8 \leq x \leq 1{,}0$. A similar transition happens in $LnSr_2Ga_{1-x}Fe_xCu_2O_7$ (Ln=Y, Ho).

A slow heating rate is required and the ideal sintering temperature increases with *x;* a temperature very close to 973 °C for partial substitution of Sr for Ba is essential to produce phase-pure samples with x=0,8. The melting point also increases with *x,* from 1030 °C for $x=0$ (in oxygen) to 1061 °C for $x=0{,}5$. Critical temperatures and unit cell parameters decrease isotropically with Sr content. Neutron diffraction confirmed the substitution of Sr at the Ba site.

Other solid solutions limits of $R(Ba_{1-x}Sr_x)_2Cu_3O_\delta$ have $x=0{,}5$ for R=Nd, Sm, Eu, Gd, Dy. Solid solution of R=Yb forms for $0{,}1 < x < 0{,}5$, but it doesn't form for

R=Lu. The orthorhombicity, unit cells decline with *x* in all cases; for R=Gd and an O/T transition occurs at *x*=0,3. T_c decreases with *x*, the suppression of T_c for R=Eu was found to be stronger than for R=Y. The normal state resistivity increases with *x* but decreases with decreasing size of R. No such correlation was detected for T_c, with values at *x*=0,25 of 82,8 K (Nd), 82,8 K (Y), 85,5 K (Gd) and 86,9 K (Sm).

Solubility limits in $Y(Ba_{1-x}Ca_x)_2Cu_3O_\delta$ vary from 0,1 to 0,5, critical temperatures decrease with Ca content.

2.3.3.5. Ba by other divalent

T_c decreases with size of M in solid solutions $Y(Ba_{1-x}M_x)_2Cu_3O_\delta$ with x=0,05 and 0,10 for M=Mg, Ca, Sr, with values at *x*=0,1 of 92 K (Sr), 87,7 K (Ca) and 86,5 K (Mg). At the same time, Mg was found to substitute instead at the Cu site.

Substitution of Hg in solid solutions $Y(Ba_{1-x}Hg_x)_2Cu_3O_\delta$ was used to prepare a 90 K superconductor in air; HgO separates, oxidizing the sample. Hg is lost by volatilization.

2.3.3.6. Ba by monovalents

Solid solutions $Y(Ba_{1-x}A_x)_2Cu_3O_\delta$ have been studied for A=Li, Na, K, Rb and Cs; these have ionic radii of 0,74, 1,02, 1,38, 1,49 and 1,70 Å, respectively, for 6-fold coordination compared with 1,36 Å for Ba.

Unit cells remain orthorhombic and constant and decrease slightly like critical temperatures. Li, Cs and Na substituted samples were impure. When the effect of substitution of K, Rb and Cs at the Y and Ba sites was compared, Tc values were typically 2 K higher for Ba than for Y substitution [75].

2.3.4. Studies in doping to Cu-region

The effect of doping to copper ions region in YBCO is slightly more complex than the others. The first reason for this confusion is the presence of two different Cu ions, and doping in this case will have a different effect on superconductivity and the electronic structure. The second reason, Fe and Co impurities affect short-range order and the amount of oxygen in the Cu(l)-O(1) layer and they can change the number of carriers in Cu(2)-O(2,3) plane. Copper oxide layers are considered as conductor layers of a high temperature superconductor. The charge of copper oxide layers can be changed by forming faults or by doping elements with different valence values to special lattice points. Transition metals are usually used for improving the physical properties of YBCO, however, a large part settles Cu region that is a decisive influence on the superconductivity in the fact. Kamlott and his group studied YBCO samples doped by many transition-metal [42].

The 90 K superconductivity did not change for Zr, Ta, Ti, Pt, Rh and Re. Namely, these transition elements doped didn't enter into lattice. When Nb, V, Fe, Co, Ni, Pd and Ru elements are doped, it was observed a reduction in the critical temperature. Neutron scattering measurements showed that Zn settled to Cu (2) region and Ga settled to Cu (1) chain. So, the specific properties of the copper in the $3d^9$ are important to get high-T_c.

According to structural, magnetic and superconducting investigation of $YBa_2Cu_{3-x}M_xO_{7-\delta}$ compounds, paramagnetic and diamagnetic doping composes different effects in structure. Ni, Fe and Co are paramagnetic and Zn and Al are diamagnetic doping. For example, Zn and Ni with $^{+2}$ multivalent ions don't alter the sample content and they retain the orthorhombic phase, while filling the holes in CuO_2 plane. Al, Fe and Co with $^{+3}$ valence fill Cu (1) chains zones. The amount of

oxygen is increased with these ions in this structure, gaps around the doping region are filled and tetragonal phase transition is observed at smaller x values from 0,1. Critical temperature change via the percentage of doping material is shown in Figure 2.5. T_c of sample doped with Zn and settled Cu (2) plane shows faster decreasing than sample doped with Al, Fe, Co, and settled Cu (1) chain.

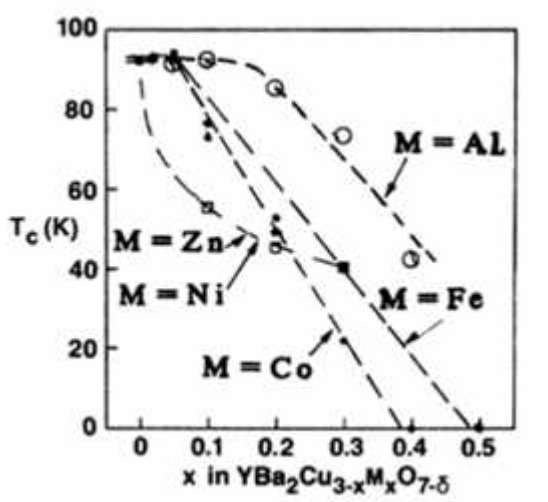

Figure 2.5: Change in T_c with percentage of doping in$YBa_2Cu_{3-x}M_xO_\delta$ (M=Ni^{+2}, Zn^{+2}, Al^{+3}, Fe^{+3} and Co^{+3}) [84]

Many studies related to the $YBa_2(Cu_{1-x}M_x)_3O_\delta$ doped by the first row transition metals and Ga, Al elements had been made and these material properties are investigated. The critical temperature of the samples can be summarized in the following table 2.3 [75].

Table 2.3: Critical temperature found in $YBa_2(Cu_{1-x}M_x)_3O_\delta$ structure [69]

x	Sc	Ti	V	Cr	Mn	Fe	Co	Ni	Zn	Ga
0,1		75		84,5	78,9	38	21,2	66,3		
0,033						61	55	80	70	51
0,1				86	92	50	50	73	40[a]	
0,033						73	73	55	55	
0,033						88	88	80	58	
0,1				86	86	81	81	86		
0,06[b]	92,5	88,3	91,8	87	88,4			82,5	60	

[a] x=0,041 [b] $YBa_2Cu_3M_{0,06}O_\delta$

2.3.4.1. Cobalt (Co) doping

x value in the $YBa_2(Cu_{1-x}Co_x)_3O_\delta$ compound could be taken up 0,33. In these materials the orthorhombic-tetragonal (O/T) transition is formed in 0,025< x < 0,033 value. The doped Co atoms replace atoms in Cu (1) sites.

As it can be seen in Table 2.3 the critical temperature is completely reduced with doped Co and superconductivity is completely eliminated at the value of x=0.l5 to 0,40. The reduction in critical temperature is very small in the lower x value, but in some articles, T_c remains constant or shows a small increase around O/T transition and decrease more fast at greater x [75].

2.3.4.2. Iron (Fe) doping

Virgin 1-2-3 YBCO material normally shows wide and more or less regularly spaced (110) and (110) twin bands; the departure between subsequent interfaces is approximately 100 nm. (001) type diffraction patterns over such twin interfaces display a characteristic spot splitting, which permits to realize the orthorhombicity and indirectly also the (local) oxygen content. Such a pattern from a fully oxidized sample is reproduced. The average structure finally happens tetragonal. This diffraction effect is the result of a fragmentation in real space of the structure in micro-twin domains. For limited substitutions, iron ions have been doped Cu(1) atoms in the CuO chain layer [85] where they pin the interfaces, in agreement with a decreasing twin size for increasing iron content [86]. For the more strongly doped materials, individual twin interfaces can no longer be recognized and a tweed structure improves. Although the average structure is tetragonal, locally orthorhombic distortions are still present; this can be concluded from high resolution images of a tweed structure. Optical

diffraction (Fourier transforms) of limited areas of the high resolution image expose the orthorhombic distortion. At high iron content and with the right heat treatment, the twin bands persevere but a fine tweed structure is superimposed. The reason of this fine tweed structure has been related with the presence of strain fields caused by iron ions or iron clusters not located along the (110) type interfaces [86].

For materials doped iron, O/T transition occurs at $x \sim 0{,}3$ value. Also it was argued that orthorhombic and tetragonal structure occurs together in case of Fe-doping.

In some views, it is said that the displacement occurs sometimes in the Cu (l) region and sometimes at both sites [75]. Atomic displacement happens in Cu (1) site for very low ratio of Fe doping. If Fe doping quantity increases, it happens in Cu (2) site. Another groups found that the preference of site depends on oxygen quantity. Cu(l) site for $\delta > 6{,}8$ and Cu (2) site for lower oxygen quantity is preferred. Oxygen quantity increases with iron concentration. T_c changes with x like Co-doping (there is sharp falling in tetragonal phase and there is small decreasing in orthorhombic phase) and superconductivity destroyed completely for %10-15 Fe doping [75].

2.3.4.3. Nickel (Ni) doping

The solubility limit is between x=0,04 and x=0,20 in the $YBa_2(Cu_{1-x}Ni_x)_3O_\delta$ compound. Although decreasing orthorhombicity, symmetry of Ni doped materials remain orthorhombic. Oxygen content is constant or increases a little. A decrease in critical temperature, which there was direct proportion with amount of x doping, was observed. Also the normal state resistance increases with x [75].

2.3.4.4. Zinc (Zn) doping

The maximum solubility reported in Zn doping for the structure of $YBa_2(Cu_{1-x}Zn_x)_3O_\delta$ is generally x=0,1. All compounds are orthorhombic and oxygen content remains constant or decreases. Critical temperature is greatly reduced with the doping Zn (till~10-13 K). The maximum critical current density is at x=0,01 and critical current and flux vortices of YBCO increase with Zn substitution [70].

2.3.4.5. Gallium (Ga) doping

The solubility of Ga in the $YBa_2(Cu_{1-x}Ga_x)_3O_\delta$ compound is between x=0,05 and x=0,20. Doped Ga is settled in the Cu (1) region. Critical temperature is reduced in YBCO doped Ga and it has lower T_c (~50 K) than Ni, Zn, Fe and Co for x=0,033 [75].

2.3.4.6. Aluminum (Al) doping

The solubility limit is low for Al and varies within the range of x=0,04 to 0,10. As the amount of doping is increased, the orthorhombicity is reduced and O/T transition is observed within the range of x=0,025-0,05. The critical temperature decreases inversely proportional to x. As aluminum replaces with copper atoms in Cu (l) region, the amount of oxygen increases with x [75].

2.3.4.7 Gold (Au) doping

Limited amounts of Cu (up to 5%) were replaced by different metals such as Fe, Al, Zn, Au, etc. For all substitutions, except for Au additions, the critical temperature decreases significantly upon adding foreign elements [87]. The microstructural configuration changes with this decrease in T_c.

Doping makes a small effect on the critical temperature and T_c increases 1,5 K for low concentrations. Room temperature resistance decreases, but the normal state susceptibility and the upper critical field is not hardly affected from doping. Gold settles Cu (1) site and structures remain orthorhombic. In addition, the flexibility of ceramic materials (ductility) is developed. While c lattice parameters increase significantly, the change in the parameters a and b are very small in doped YBCO [75].

2.3.4.8. Silver (Ag) and platinum (Pt) doping

Silver atoms having a larger radius than Cu atoms settle in the Cu (1) region. c lattice parameters with oxygen content decreased. Critical temperature is high in 5% Ag and Pt doped materials, but the impurity phase was found in structure. The solubility limits are 10 % for Ag and 5 % Pt. In different groups, Ag doping did not affect the critical temperature and low Ag concentrations increase T_c slightly [75].

2.3.4.9. Palladium (Pd) doping

The Pd is replaced with copper atoms in Cu(1) site. Impurity phases ($BaCuO_2$ and Y_2BaCuO_5) in the material do not contain Pd atoms and δ=6,8 adapts to the nominal stoichiometry. The critical temperature is a decrease from starting at 77 K and 49 K in the zero point [75].

2.3.4.10. Lithium (Li), magnesium (Mg) doping and doping of other substances

The solubility of the lithium in $YBa_2(Cu_{1-x}Li_x)_3O_\delta$ compound varies from 0,04 up to 0,1. Radius of Li atom is close to Cu atom and initially only on the Cu (l),

as the amount of the doping increases, it is also settled in the Cu(2) region. T_c reduces with substitutions.

The solubility limit varies between 0,04-0,2, the critical temperature is reduced for magnesium substitutions.

In addition in the work of the other doping to copper region, Nb and Ta didn't enter into the structure significantly and silicon didn't dope completely. The solubility limit, for Cd and Hg are $x < 0,02$ and for molybdenum is in range $0 < x < 0,04$ and it settles on Cu(1) region and critical temperature falls to 50 K for the value of x=0,035. In Sn doping case, $YBa_2(Cu_{1-x}Sn_x)_3O_\delta$ compound is the single-phase in $0 \leq x \leq 1$ interval value it does not show superconductivity when it exceeds the value of 0,033 [75].

Some elements are not reactive with YBCO, when these elements is added the structure, it does not replace any of the elements in the lattice and remains in the region between the grains. In this case, changing the properties of grain boundaries significantly affects superconductivity properties of the material. Also Silver is commonly used in changing the properties of grain boundaries of YBCO.

Replacement of Ba by Sr (or by a mixture of Sr and Ce) does not change the topology of the YBCO-123 structure. However Co ions as well as Ga ions have a strong tendency to be tetrahedrally coordinated by oxygen ions in the isostructural compounds $YSr_2Cu_2CoO_7$ and $YSr_2Cu_2GaO_7$ [84, 88]. Therefore the CoO or GaO layers, which are instead of the CuO chain layer, adopt a configuration of chains of corner sharing MO_4 (M=Co, Ga) tetrahedral along the [110]p and [110]p directions and p refers to the perovskite base. The tetrahedron of oxygen atoms around the M ion contains the two oxygen atoms of the SrO layer forming the apices of the CuO(5) pyramid and of two oxygen atoms in the MO-layer. In reality these tetrahedral are

rotated about an axis parallel to c. This rotation can take place in two "a priori" equally probable senses, giving rise to zigzag chains of opposite "phase" along [110]p or [110]p (see figure 2.6). In the structure described by Roth et all. [88] all parallel chains are either all L-chains or all R-chains which have identical surroundings and hence are energetically equivalent.

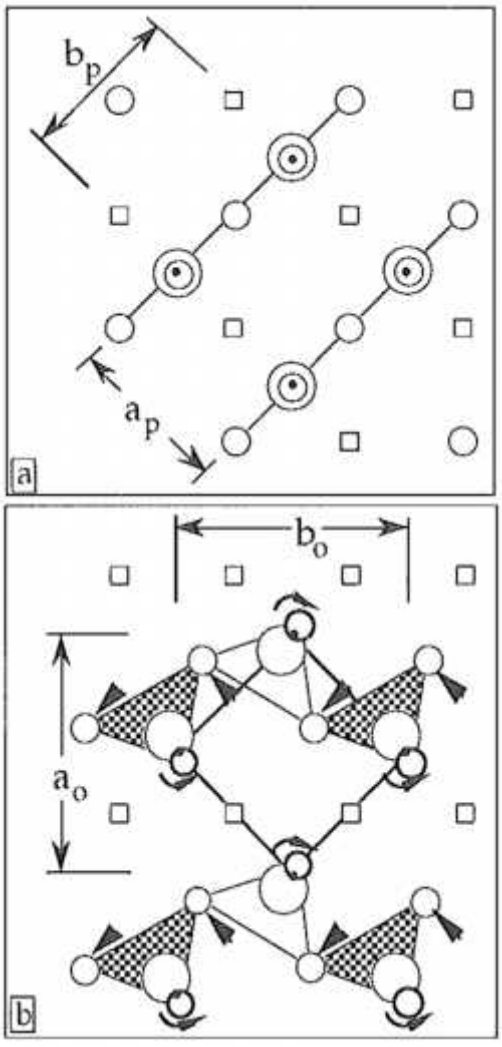

Figure 2.6: Schematic representation of the atom configuration of (a) the CuO chain layer in $YBa_2Cu_3O_7$ with a square configuration of O around Cu and (b) the MO layer, showing the chains of tetrahedral along the [110]p direction. Large circles are M-ions, small circles are oxygen ions. Vacancies are indicated by squares [40]

The basic unit cell (with all chains parallel and of the same type) is designated by a rectangular quasi-square lattice with $a_0 = b_0 = \sqrt{2a_p}$, where a_0 is selected perpendicular to the chains. In the compounds studied the chains are parallel in two MO-layers successive along c_0 and are moved with respect to each other in such a way that they form a surprised arrangement when they are viewed end-on.

2.3.5. Effect of oxygen gap

The effect of oxygen is very high on the electronic properties of high-temperature superconductors. Normally, an oxygen atom takes two electrons from another atom. If there is the lack of oxygen, there will be two free electrons which can go to any place in the crystal.

Oxygen gaps change the number of free carriers in the crystal lattice. According to the model of load–transmission, oxygen deficit is revealed in the CuO chains. While CuO_2 layers stay chemically unchanged, $CuO_{1-\delta}$ structures occur. Amount of oxygen should be controlled in doping YBCO. Because the amount of oxygen affects the number of carriers in the CuO_2 plane and determines the value of T_c.

Changes in the crystal structure of YBCO with different substitutions have been researched by electron microscopy and have been associated to the physical properties of these substituted materials. Oxygen ordering has been examined in superconducting $RBa_2Cu_3O_{7-\delta}$ ceramic materials with R=Er, Nd, Sm, Pr Y and Yb. The critical temperature Tc was obtained as a function of the oxygen deficiency of the compound. Small Fe substitutions for Cu have a vivid effect on Tc as well as on the microstructure. The twin domain size declines and

a "tweed" pattern results. Arbitrarily distributed Fe^{+2} ions or Fe^{+2} clusters entertainment as pinning centers for twin interfaces. Ga or Co inclusions for Cu alter the structure of the "chain" layer.

CHAPTER 3

EXPERIMENTAL DETAILS

3.1 Preparation of Superconducting $Y_{1-x}Ho_xBa_2Cu_3O_{7-\delta}$, $YBa_{2-y}Nd_yCu_3O_{7-\delta}$ and $Y_{1-x}Ho_xBa_{2-y}Nd_yCu_3O_{7-\delta}$

There are many preparation methods of ceramic superconductor, which are Nitrate Method, The Flame-Quench-Melt-Growth Method, Sol-Gel Method, Co-Precipitation, Aqueous Combustion Synthesis, Microemulsion, Powder-In-Tube Method, The Solid-State Reaction Method, Chemical Route and Novel Preparation Method etc. The solid-state reaction method is the most common preparation route for ceramic superconductors since researchers have better control on processing and does not require special equipment.

Superconducting $Y_{1-x}Ho_xBa_{2-y}Nd_yCu_3O_{7-\delta}$ samples were prepared by the standard solid-state reaction method. For this method, the appropriate amounts of Y_2O_3, Ho_2O_3, $BaCO_3$, Nd_2O_3 and CuO were mixed in the stoichiometric ratios of $Y_{1-x}Ho_xBa_{2-y}Nd_yCu_3O_{7-\delta}$ for two hours in mortar. Table 3.1 explains the properties of compounds.

Table 3.1: Atomic weight and purity of the compounds

Compound		Purity (%) (Alfa Aesar)	Atomic Weight (gr)
Symbol	Name		
Y_2O_3	Yttrium (III) Oxide	99,99	225,81
$BaCO_3$	Barium Carbonate	99,95	197,35
CuO	Copper Oxide	99,00	79,55
Nd_2O_3	Neodymium (III) Oxide	99,99	336,48
Ho_2O_3	Holmium (III) Oxide	99,90	377,86

Therefore, the chemical equilibrium equation was written as following:

$$(0,5–(x/2))Y_2O_3+(\ x/2)Ho_2O_3+BaCO_3+3CuO+nO_2 \rightarrow Y_{1-x}Ho_xBaCu_3O_{7-\delta}+CO_2$$

$$(0,5)Y_2O_3+(2-y)BaCO_3+(0,5y)Nd_2O_3+3CuO+nO_2 \rightarrow Y_1Ba_{2-y}Nd_yCu_3O_{7-\delta}+CO_2$$

$$(0,45)Y_2O_3+(0,05)Ho_2O_3+(2-y)BaCO_3+(0,5y)Nd_2O_3+3CuO+nO_2 \rightarrow$$

$$Y_{0,9}Ho_{0,1}Ba_{(2-y)}Nd_yCu_3O_{7-\delta} + CO_2$$

$$(0,5–(x/2))Y_2O_3+(x/2)Ho_2O_3+(1,75)BaCO_3+(0,125)Nd_2O_3+3CuO+nO_2 \rightarrow$$

$$Y_{(1-x)}Ho_xBa_{(1,75)}Nd_{0,25}Cu_3O_{7-\delta}+CO_2$$

Final equilibrium concentration

$$(0,5–(x/2))Y_2O_3+(x/2)Ho_2O_3+(2-y)BaCO_3+(0,5y)Nd_2O_3+3CuO+nO_2 \rightarrow$$

$$Y_{1-x}Ho_xBa_{(2-y)}Nd_yCu_3O_{7-\delta}+CO_2$$

$$(0,45)Y_2O_3+(0,05)Ho_2O_3+(1,90)BaCO_3+(0,050)Nd_2O_3+3CuO+nO_2 \rightarrow$$

$$Y_{0,9}Ho_{0,1}Ba_{1,9}Nd_{0,1}Cu_3O_{7-\delta}+CO_2$$

From this formula, the quantities of reactants to produce approximately 6 grams of unreacted compound were shown in Table 3.2, 3.3, 3.4 and 3.5.

The mixed powders were calcined in alumina crucible in air at temperatures of 930 °C, for 24 hours in furnace as seen in figure 3.1 and figure 3.2. Throughout our experiments, the heating and cooling rates of the temperature were chosen to be 3 and 2 °C min^{-1}, respectively.

Table 3.2: Calculations for 6 grams of starting material for $Y_{1-x}Ho_xBaCu_3O_{7-\delta}$ stoichiometry

Sample Name	Doping Quantity=x	Atomic Weight (gr)	Y_2O_3	$BaCO_3$	CuO	Ho_2O_3	Total (gr)
YHo0	0,000	548,90500	1,23415	2,15720	2,60865	0,0000	6,0000
YHo1	0,025	550,80563	1,19914	2,14976	2,59965	0,05145	6,0000
YHo2	0,050	552,70625	1,16438	2,14237	2,59071	0,10255	6,0000
YHo3	0,100	556,50750	1,09556	2,12773	2,57301	0,20370	6,0000
YHo4	0,250	567,91125	0,89463	2,08501	2,52134	0,49901	6,0000
YHo5	0,500	586,91750	0,57711	2,01749	2,43970	0,96571	6,0000
		TOTAL (gr)	6,16497	12,67956	15,33305	1,82241	36,00000

Table 3.3: Calculations for 6 grams of starting material for $Y_1Ba_{2-y}Nd_yCu_3O_{7-\delta}$ stoichiometry

Sample Name	Doping Quantity=x	Atomic Weight (gr)	Y_2O_3	$BaCO_3$	CuO	Nd_2O_3	Total (gr)
YNd0	0,000	746,25500	0,90777	3,17345	1,91878	0,00000	6,0000
YNd1	0,025	745,52725	0,90866	3,13684	1,92065	0,03385	6,0000
YNd2	0,050	744,79950	0,90955	3,10016	1,92253	0,06777	6,0000
YNd3	0,100	743,34400	0,91133	3,02658	1,92630	0,13580	6,0000
YNd4	0,250	738,97750	0,91671	2,80411	1,93768	0,34150	6,0000
YNd5	0,500	731,70000	0,92583	2,42743	1,95695	0,68979	6,0000
		TOTAL (gr)	5,47985	17,66856	11,58289	1,26870	36,00000

Table 3.4: Calculations for 6 grams of starting material for $Y_{0,9}Ho_{0,1}Ba_{(2-y)}Nd_yCu_3O_{7-\delta}$ stoichiometry (Ho is constant and Nd is variable)

Sample Name	Doping Quantity=x	Atomic Weight (gr)	Y_2O_3	Ho_2O_3	$BaCO_3$	Nd_2O_3	CuO	Total (gr)
HcN0	0,000	751,85750	0,80876	0,15037	3,14144	0,00000	1,8994	6,0000
HcN1	0,025	751,12975	0,80954	0,15052	3,10517	0,03351	1,9013	6,0000
HcN2	0,050	750,40200	0,81032	0,15066	3,06883	0,06708	1,9031	6,0000
HcN3	0,100	748,94650	0,81189	0,15095	2,99594	0,13442	1,9068	6,0000
HcN4	0,250	744,58000	0,81664	0,15184	2,77556	0,33802	1,9179	6,0000
HcN5	0,500	737,30250	0,82468	0,15333	2,40247	0,68270	1,9368	6,0000
		TOTAL (gr)	4,88182	0,90767	17,48941	1,25573	11,46537	36,0000

Table 3.5: Calculations for 6 grams of starting material for $Y_{(1-x)}Ho_xBa_{(1,75)}Nd_{0,25}Cu_3O_{7-\delta}$ stoichiometry (Nd is constant and Ho is variable)

Sample Name	Doping Quantity=x	Atomic Weight (gr)	Y_2O_3	Ho_2O_3	$BaCO_3$	Nd_2O_3	CuO	Total (gr)
NcH0	0,000	738,97750	0,91671	0,00000	2,80411	0,34150	1,9377	6,0000
NcH1	0,025	740,37813	0,89150	0,03825	2,79692	0,34062	1,9327	6,0000
NcH2	0,050	741,77875	0,86642	0,07631	2,78976	0,33975	1,9278	6,0000
NcH3	0,100	744,58000	0,81664	0,15184	2,77556	0,33802	1,9179	6,0000
NcH4	0,250	752,98375	0,67029	0,37388	2,73380	0,33294	1,8891	6,0000
NcH5	0,500	766,99000	0,43593	0,72947	2,66693	0,32479	1,8429	6,0000
		TOTAL (gr)	4,59750	1,36974	16,56707	2,01762	11,44806	36,0000

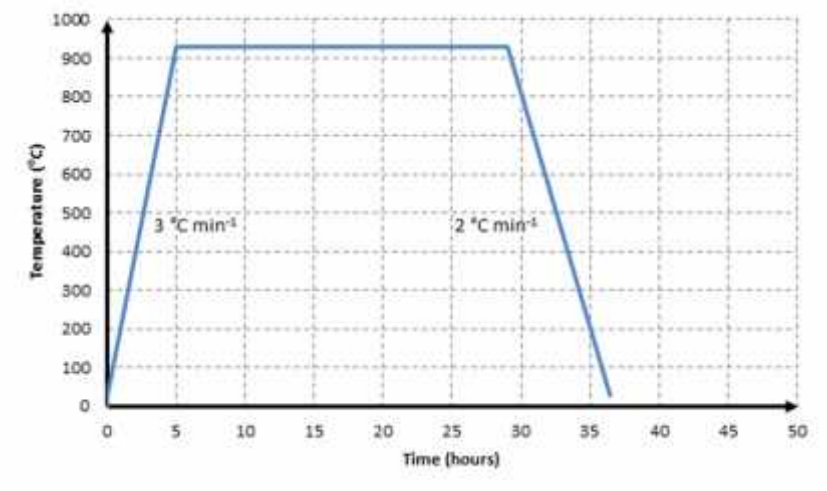

Figure 3.1: Calcinations process of the powder

Figure 3.2: Single zone programmable tube furnace (Protherm – PTF 12/50/450)

3.2 Sintering process

As well known, the sintering process performed at higher temperatures than calcinations process helps the carbons in the starting powders to release. This is very important to save the formation of the impurity phases [89]. The calcined material was reground for two hours in mortar again and pressed into pellets of 40x5x2 mm^3 at 330 MPa with a manual hydraulic press (Figure 3.3) to increase the connection areas of the grains.

Figure 3.3: TÜMAS manual hydraulic press

All calcinations and annealing processes are shown in figure 3.4.

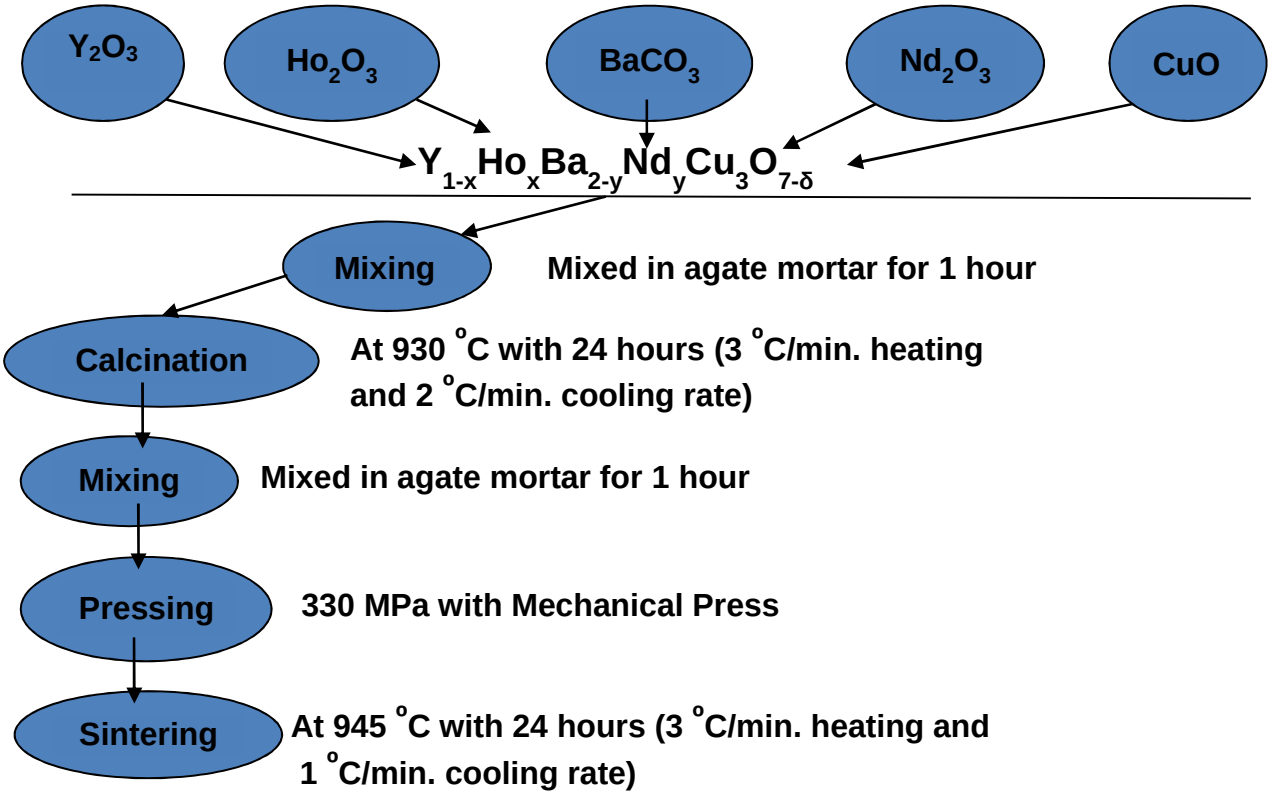

Figure 3.4: Schematic diagram of preparation of $Y_{1-x}Ho_xBa_{2-y}Nd_yCu_3O_{7-\delta}$ superconductor

The DTA results indicate that Ho and Nd addition can change (decrease) the melting temperature of Y-system superconductors. This may be because of the Ho^{+3}, Nd^{+3} and Nd^{+2} ionic radius is different from the Y^{+3} and Ba^{+2} ionic radius. Moreover, the atmosphere has an important influence on melting temperature. This has potential for fabricating oxide superconductors with a metal substrate, since the superconductor cannot react with some metals at lower temperature [90].

The pellets were sintered in air at 945 ^{o}C for 24 h and then cooled down to room temperature. The heating and cooling rates of the temperature were chosen to be 3 and 1 ^{o}C min^{-1}, respectively (Figure 3.5). At the same time, O_2 was given between 716 ^{o}C and 416 ^{o}C while the pellets sintered were cooling.

The annealing and evaporation process was performed in a programmable tube furnace from PROTHERM (Model PZF 12/75/700) in Figure 3.6. The aim for annealing the samples was to complete the phase formation, improve the mechanical properties, obtain better grain growth and enhance the superconducting properties. In forthcoming sections, the superconducting ceramics prepared with different Ho stoichiometry such as 0, 0,025, 0,050, 0,100, 0,250 and 0,500 will be abbreviated as YHo0, YHo1, YHo2, YHo3, YHo4 and YHo5, respectively. At the same times, Nd samples are YNd0, YNd1, YNd2, YNd3, YNd4 and YNd5, Ho constant (x=0,100) Nd samples are HcN0, HcN1, HcN2, HcN3, HcN4 and HcN5 and Nd constant (y=0,250) Ho samples are named as NcH0, NcH1, NcH2, NcH3, NcH4 and NcH5.

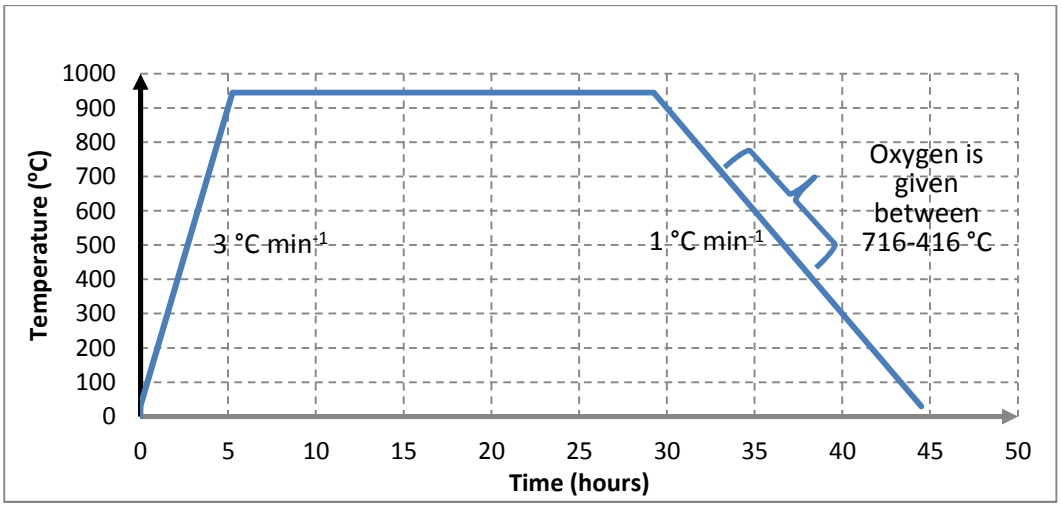

Figure 3.5: Sintering process of the samples

Figure 3.6: Protherm (Model PZF 12/75/700) programmable tube furnace (3 zones)

3.3 Characterization of the bulks

X-Ray diffraction analysis (XRD), resistivity, transport critical current density, the bulk density, scanning electron microscopy (SEM), Electron Dispersive Spectroscopy (EDS) and Vickers microhardness (H_v) measurements are performed to determine the effect of Ho, Nd and co-doping of (Ho+Nd) on the microstructural, electrical, mechanical and superconducting properties of the superconducting bulks produced.

3.3.1 X-Ray diffractometer measurements

X-Ray diffractometer was used to examine the structure of a material from the scattering pattern. The working mechanism was subject to the interaction between high-energy beams of radiation or charged particles and a material. X-ray diffraction measurements were exerted with the aid of a Rigaku Multiflex+XRD diffractometer in Figure 3.7 with CuK_{α} target giving a monochromatic beam (wavelength of 1,54 Å) in the range of 2θ=3–60° at a scan speed of 3°/min and step increment of 0,02° in air atmosphere at the room temperature. The XRD patterns obtained allow us to discuss the change of the texturing, phase purity, crystal structure, grain size (from Scherrer–Warren approach) and cell parameters (accuracy of ±0,*0*1 Å).

Figure 3.7: Rigaku MultiFlex 2kW X-Ray Diffractometer

3.3.2 Resistivity measurements

The electrical characteristics belonging to the pure and substituted Y-123 superconducting ceramics are studied by means of the temperature dependent-resistivity measurements using 5 mA DC current through the sample surface in the

He gas contact cryostat (Figure 3.8) with provision for the vacuum in the temperature range of 40-110 K. The standard four-probe measurements are exerted with a Keithley 2400 source meter and a Keithley 2700 multimeter. The four-point contacts are made by the silver paint to be rid of the extra resistivity. The current was applied to the two outer electrical contacts. The voltage drop across the two inner electrical contacts was measured against temperature.

Figure 3.8: Cryo Industries 7 T resistivity measurement system

The resistivity of the bulks studied is determined by the following relations;

$$R = \frac{^{\circ}L}{A} \quad \text{and} \quad V = I.R \tag{1}$$

$$^{\circ} = \frac{RA}{L} = \left(\frac{V}{I}\right).\left(\frac{A}{L}\right) \tag{2}$$

where ρ denotes the resistivity of a material, L is the distance between the inner electrical contacts, and A presents the cross-section of the bulks.

Additionally, a temperature value, where the resistance started to decrease sharply, is called the onset critical temperature (T_c^{onset}) of the samples whereas the offset

transition temperature (T_c^{offset}) is defined as the temperature at which R=0 Ω (within the sensitivity of the measurement system).

3.3.3 Critical current density measurements

The measurement of the potential difference between the inner contacts is used to obtain the maximum current passing through a material or critical current density of a material when the current applied to the material is regularly enhanced at the constant temperature at which this material exhibits the superconducting properties and so the potential difference is recorded as zero. However, when the critical value is reached, the potential difference starts to increase immediately due to the presence of the resistance. In this work, the transport critical current experiments are performed in self-field using four-probe method at the liquid nitrogen temperature of 77 K in zero magnetic fields. A PCE Power Control GEN1500 programmable current source (6V-200A) and a Keithley 2700 Multimeter were used for I-V measurements. The experimental data obtained are recorded by Labview software. The current applied parallel to the direction of pressed surface is ramped at a constant rate (100 mA/s) for the entire sample. The critical current (I_c) values of the samples are defined with the criterion of 1 μV/cm. The J_c values are calculated from the I_c and the total cross-sectional area of the samples studied.

3.3.4 The bulk density

At the same time, the bulk densities of the superconducting samples are experimentally measured via the density measurement kit based on Archimedes water displacement method. They are shown in Table 4.5, Table 4.6, Table 4.7 and Table 4.8.

3.3.5 Scanning electron microscopy measurements

A high-energy focused beam of electrons scan the surface of a material in Scanning electron microscope (SEM). After the interaction between the incident electrons and atoms in the material, a signal containing the information about the surface topography of the material appears. Micrographs of the samples were magnified approximately 3000 and 5000 times and magnification bar is given on each micrograph. In this thesis, the microstructural (surface morphology, crystallinity, crystal plane alignments, porosity, melting, microvoids, cracks, grain size distribution and connectivity between the superconducting grains) analyses are performed by a Jeol scanning electron microscope (Model Number: JEOL 6390-LV) (Figure 3.9) at the operation voltage of 20 kV with a resolution power of ≈3 nm.

3.3.6 Electron dispersive spectroscopy measurements

Electron dispersive spectroscopy (EDS) is used for analyzing the elemental or chemical characterization of a material. As well known at rest, an atom has ground state (or unexcited) electrons in discrete energy levels. The incident beam (high-energy beam of charged particles) can excite an electron in an inner shell of an atom and in fact ejecting the electron from the shell. Hence, a hole appears in the inner shell. Accordingly, an electron from an outer (higher-energy) shell fills the hole appeared. The energy between the outer and the inner shell can be released in the form of a photon. Energy-dispersive spectrometer can be used to measure the number and energy of the photon emitted from the material. By analyzing the photon emitted, the elemental composition of the material studied can also be determined. In this dissertation, the element composition and distribution examination are also searched by SEM equipped with an eumex Electron Dispersive Spectroscopy (EDS). IXRF

SYSTEMS Model 550i Analyzer (Figure 3.9) is used to investigate the photon (x-rays) emitted from the bulks.

If micrographs contain voids and unoriented grains, this explains low critical current density values.

Figure 3.9: JEOL JSM-6390LV Scanning Electron Microscope and IXRF Systems Model 550i Analyzer (EDS)

3.3.7 Vickers microhardness

Regarding the mechanical properties belonging to the superconductors, the experimental microhardness results are recorded at the different locations on the specimen surfaces in the air atmosphere at room temperature using a digital microhardness tester (SHIMADZU, HVM-2). The indentation load is applied for 15 s in the load range from 0,245 to 2,940 N with the accuracy of ±0,*1* μm. Moreover, the Vickers microhardness, elastic modulus and yield strength values are inferred from the microhardness curves. The experimental findings are investigated by the available methods of Hays–Kendall (HK) approach and indentation-induced cracking (IIC) model.

CHAPTER 4

RESULTS AND DISCUSSIONS

4.1 XRD Analyses

In this extensive study, X-ray diffraction (XRD) patterns recorded at the room temperature of the pure Y-123, Y-site Ho substituted compounds, Ba-site Nd substituted compounds and co-doping of Ho+Nd enable us to determine the crystal plane alignment, phase purity, crystal structure, crystallite size and lattice parameters. The XRD patterns obtained between 20° and 60° for the samples are given in Figure 4.1 a, b, Figure 4.2, Figure 4.3 and Figure 4.4. It is visible form the diagrams in the figure that the corresponding Miller indices *h k l* are attributed to perovskite based Y-123 phase whereas the other characteristic peaks marked on the patterns are in correspondence to the $BaCuO_2$, $Y_2Ba_4Cu_7O_{14+x}$ (Y-247) and $YBa_2Cu_4O_8$ (Y-124) phases. It is natural to say that especially Y-124 and Y-247 can easily act as an intergrowth within the perovskite based Y-123 phase as a result of the additional Cu–O chain layer adjacent to the Ba–O plane resulting in double chain layer in the system [91,92]. Prior to discussions, it is to be mentioned here that virgin compound crystallizes in an orthorhombic structure with space-group P/mmm.

The orthorhombic crystal system improves with the increment of Ho doping level at the Y-site, with the increment of HcN doping level at the Ba-site in the superconducting matrix until a certain value of x, y=0,100, with the increment of Nd doping level at the Ba-site in the superconducting matrix until a certain value of x=0,250, with the decrement of NcH doping level at the Y-site in the

superconducting matrix until a certain value of x=0,100 beyond which the crystal structure tends to exhibit the tetragonal.

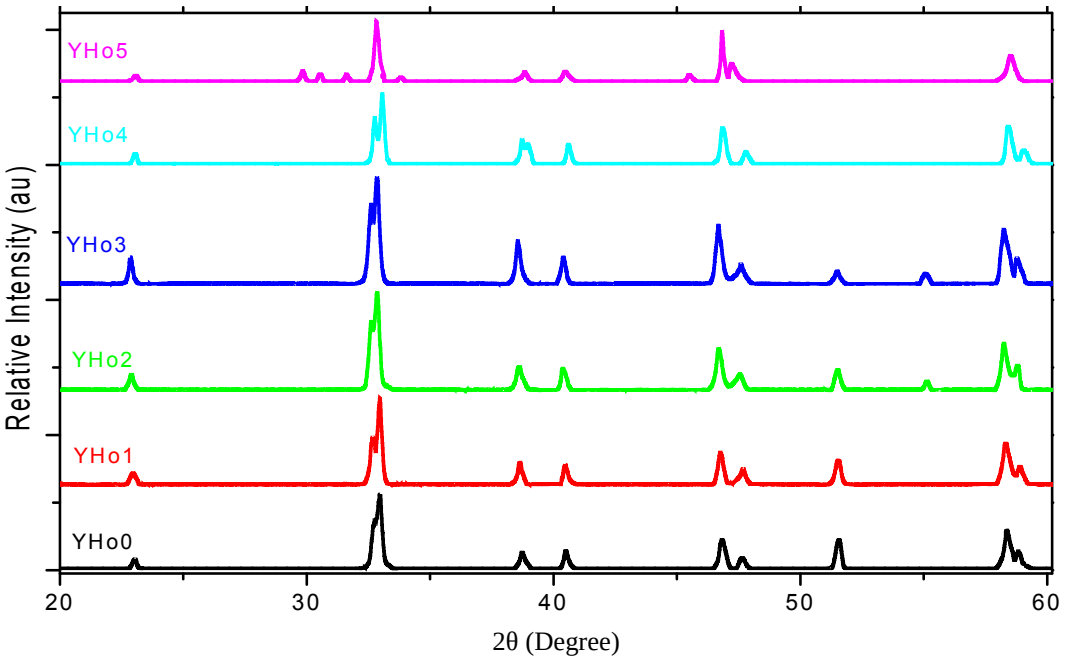

a)

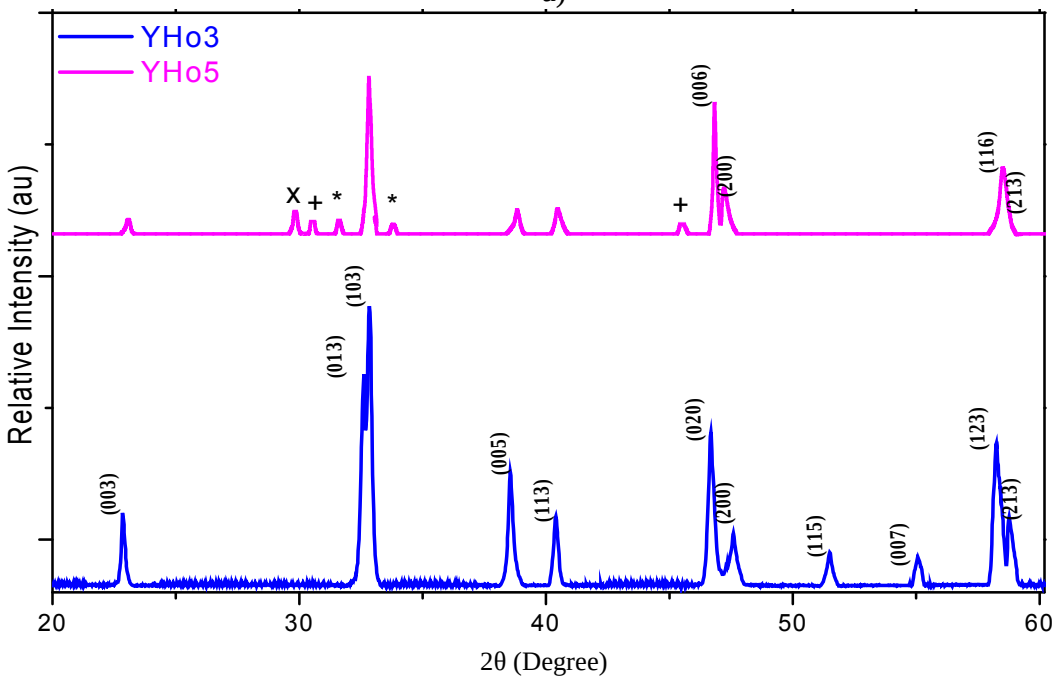

b)

Figure 4.1: a) XRD patterns belonging to the virgin and Y-site Ho substituted compounds and b) the detailed *XRD* patterns with the miller indices for the best (YHo3) and worst (YHo5) samples

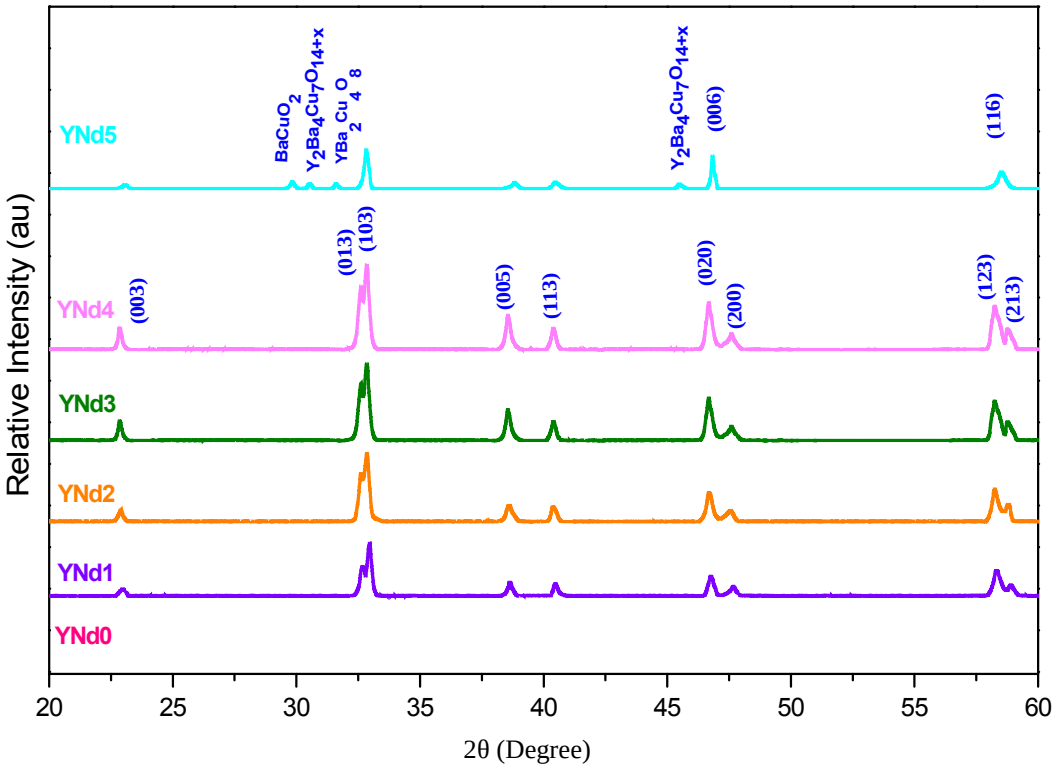

Figure 4.2: XRD patterns belonging to the virgin and Ba-site Nd substituted compounds

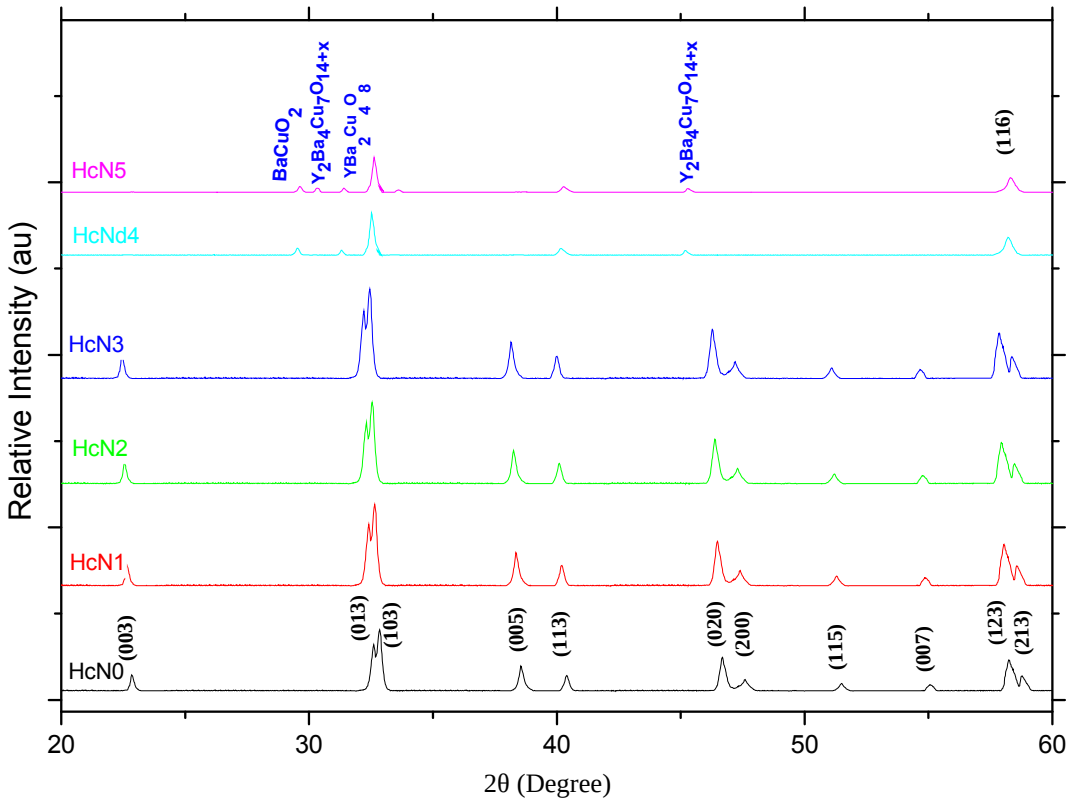

Figure 4.3: XRD patterns belonging to the Ho constant (x=0,100) and Nd variables (from y=0 to y=0,500) compounds

In fact, the YHo5, YNd5, HcN4 and NcH4 compounds almost present the tetragonal nature due to both the presence of the mixture phases and especially the occupation of unfilled O(5) sites in CuO_x chains in the system. In other words, excess (0,100 < x) Ho inclusions and excess (0,250 < x) Nd inclusions are unfavorable for the Y-123 phase formation.

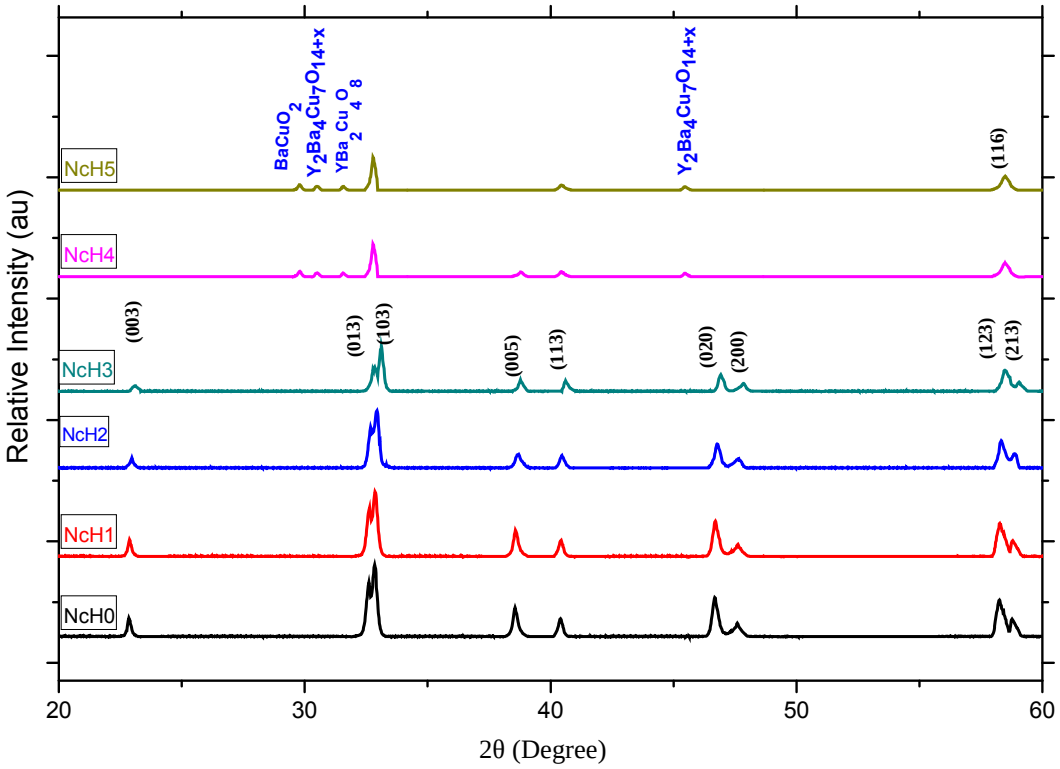

Figure 4.4: XRD patterns belonging to the Nd constant (y=0,250) and Ho variables (from x=0 to x=0,500) compounds

Here, it is necessary to underline that non-existence of any different phases containing the Ho and Nd impurities and other cation shows no solubility limit of Ho and Nd in the Y-123 system up to the content level of x=0,100 and y=250, respectively. Namely, the solid solubility of the Y-site Ho and Ba-site Nd substituted compounds are found to be larger than x=0,100 and y=250, respectively [93]. This is attributed to the fact that the Ho^{+3} inclusions until a certain dopant content level of x=0,100 are introduced into the Y-123 crystal structure by replacing Y^{+3} individuals

and same property is seen between Ba^{+2} and Nd^{+2} until y=0,250 [94-97]. At the same time, the figures ensure that each sample mentioned in this work exhibits the polycrystalline superconducting phase with greater intensity of diffraction lines as the Ho and Nd concentration levels enhance in the Y-123 superconducting system. Here, it is noteworthy that far greater peak intensity demonstrating the enhanced grain growth and orientation of grains results in the increment in the critical current density [98, 99].

From the Ho content level of x=0,100 onwards, from the Nd content level of y=0,250 onwards, from the Ho constant (x=0,100) Nd variable content level of y=0,100 onwards, and from the Nd constant (x=0,250) Ho variable content level of x=0,000 onwards, the peaks belonging to the Y-123 phase start to decrease rapidly. In the case of the YHo5 compound, some peaks such as *013, 020, 115, 007,123* and *213,* and in the case of the YNd5 compound, some peaks such as *013, 020, 200,123* and *213* disappear immediately whereas the *006* and *116* peaks, in the HcN4 compound, some peaks such as *003, 013, 005, 113, 020, 200, 115, 007,123* and *213* and *i*n the NcH4 compound, some peaks such as *003, 013, 005, 020, 200, 123* and *213* disappear immediately whereas the *116* peaks belonging to the characteristic tetragonal crystal structure appear instantly. Even, it is well known from the literature that in the orthorhombic crystal structure, the split diffraction peaks take place at 2teta around 47,6° (*020* and *200*) and 58,3° (*123* and *213*) with high-intensity and low-angle [100]. Regarding the tetragonal crystal structure, the split peaks given above begin to merge with each other at low-intensity and high-angle (reversion of values in the angle and intensity). Therefore, new peaks (*006, 200, 116* and *213*) are sequenced at 2teta around 47,6° and 58,3°, respectively. The long and short of it is that the crystal plane alignments (known as texturing) and crystallinity

of the poly-crystallized Y-123 bulk samples retrograde with the excess Ho and Nd impurities. Moreover, the YHo5,YNd5, HcN4 and NcH4 samples exhibit the different phase formations as regards $BaCuO_2$, $Y_2Ba_4Cu_7O_{14+x}$ (Y247) and $YBa_2Cu_4O_8$ (Y124) due to the additional Cu–O chains layer adjacent to the Ba–O planes causing the double chain layers in the Y-123 system [92].

Furthermore, the variation of the cell parameters *a, b* and *c* with the Ho, Nd and co-doping ingredients (leading to the shifts of the peaks) in the superconducting matrix allows us to examine the change in superconducting characteristics of the Y-123 oxygen deficient system. One can decide the crystal structure of the system, orthorhombic or tetragonal by means of *a* and *b*-axis lengths. As well known the change of the oxygen content in the Cu–O chains [Cu_1 site] and Cu–O_2 planes [Cu_2 site] causes to the orthorhombic–tetragonal (O–T) transition due to the reordering of the unit cell structure. Namely, the layers ($BaO/CuO_2/Y/CuO_2/BaO$) in Y-123 superconducting material are interconnected by a sheet of Cu and O atoms with variable composition Cu–O_x. The oxygen sites to be appeared in the slabs are regarded as O_1, O_2, O_3, O_4 and O_5. Among them, O_1 and O_5 sites dwell in Cu-O_x strings (Cu–O chains) whereas O_2 and O_3 sites reside at the basal copper (Cu–O_2) planes. The last one, O_4 site exists in the Ba–O plane [101]. It is necessary to underline that the rare earth (RE) layer is association with the devoid of any oxygen. Moreover, fully occupied O_1 (along with the lattice parameter *b*) and unoccupied O_5 (related to the lattice parameter *a*) sites enable us to feature why the *b* axis length is longer than the *a* axis length for the orthorhombic crystal structure (inherit characteristics) [102], meaning that the oxygen change in the Cu–O chains due to the external forces such as annealing ambient, composition, heat-treatment, type, purity and quantity of the chemicals makes the crystal structure deteriorate (structural phase

transition from orthorhombic to pseudotetragonal) as a result of the change in the *a* and *b* axis lengths. The former is correspondence to the O_2 site while the latter is attributed to the O_3 site resided in the Cu–O_2 plane. In the present work, the lattice lengths are determined using the least square technique throughout *d* values and *h k l* planes for the orthorhombic unit cell structure.

$$d = \frac{1}{\sqrt{\left(\frac{h}{a}\right)^2 + \left(\frac{k}{b}\right)^2 + \left(\frac{l}{c}\right)^2}} \quad (1)$$

The results calculated are provided in Table 4.1, Table 4.2, Table 4.3 and Table 4.4. According to the results in Table 4.1, Table 4.2 and Table 4.3, initially the *a* and *b* axis lengths contract systematically from 3,829 Å to 3,819 Å and from 3,888 Å to 3,880 Å for Ho inclusion, from 3,838 Å to 3,814 Å and from 3,890 Å to 3,881 Å for Nd inclusion and from 3,820 Å to 3,781 Å and from 3,887 Å to 3,870 Å for HcN inclusion, respectively, owing to the increment in the hybridization of the in-plane Cu(3d) and O(2p) orbitals (Cu–O_2 plane) [103] whereas the c-axis length elongates from 11,704 Å to 11,734 Å with the enhancement in the Ho dopant level up to x=0,100, from 11,621 Å to 11,735 Å with the enhancement in the Nd dopant level up to y=0,250 and from 11,726 Å to 11,797 Å with the enhancement in the Ho constant (x=0,100), Nd variable dopant level up to y=0,100 after which the cell parameters *b* and especially *a* start to expand (shrivel) rapidly due to the increase (decrease) of the electrons into anti-bonding orbital [104, 105] while the lattice parameter *c* tends to shrink considerably, and in fact the *c* value reaches to local minimum point for the concentration value of x, y=0,500 for YHo and YNd samples, y=0,250 for HcN and x=0,250 for NcH samples. According to the results in the table 4.4, initially the *a* and *b* axis lengths get longer systematically from 3,811 Å to 3,831 Å and from 3,881 Å to 3,889 Å for NcH inclusion, respectively, owing to the decrement in the

hybridization of the in-plane Cu(3d) and O(2p) orbitals ($Cu–O_2$ plane) [103] whereas the c-axis length become shorter from 11,739 Å to 11,698 Å with the enhancement in the Nd constant (y=0,250), Ho variable dopant level up to x=0,100. The reduction in the c-axis length stems from preferentially substitution of Ho and Nd inclusions at the Cu_1 site in the system. In other words, the excess Ho substitution at the Y site, the excess Nd substitution at the Ba site, the excess co-doping degrade the major (Y-123) phase as a consequence of the hole filling (localization). Moreover, this behavior (firstly increment then decrement of *c* value) can be explained that the ionic radius of Ho^{+3} (104,1 pm) is slight larger as compared to that of Y^{3+} (104 pm) and the ionic radius of Nd^{2+} (143 pm) is slight smaller as compared to that of Ba^{2+} (149 pm), leading to regular expand of the cell parameter *c* with the increment of the Ho and Nd concentration in the Y-123 superconducting matrix up to the certain content value of x=0,100 and y=0,250 beyond which the *c* axis length starts to shrink rapidly. This is the consistent with the fact that the Ho^{3+} and Nd^{2+} inclusions may substitute for the Cu^{2+} individuals in the crystal structure after the critical value of x=0,100 and y=0,250, being favored by the findings of the EDS examination [106]. In other words, hole filling plays dominant character to determine the Ho and Nd substituted Y-123 superconductors.

Besides, the Y/Ho substitution, Ba/Nd substitution and co-doping successfully performed or not can also be checked from the oxygen concentrations in the unit cells of the samples mentioned in this work by means of the following equation [107]:

$$y = 7 - \frac{c - 11.68}{0.1501} \tag{2}$$

The oxygen concentrations calculated are given in Table 4.1, Table 4.2, Table 4.3 and Table 4.4. It is visible from the table that the values are found to range from

6,8414 (for the virgin sample) to 7,0193 (for the YHo5 compound). It should be mentioned here that the value initially decreases to local minimum of 6,6376 (for the YHo3 specimen) and then considerably increases to 7,0193 due to the significant decrement of the cell parameter *c*, verifying that the Ho nanoparticles mainly occupy around the Cu_1 sites in the crystal structure [100]. The same properties are seen for Nd and co-doping samples.

Additionally, broadening nature in the X-ray diffraction patterns enables us to examine how the crystallite (grain) size changes with the Ho, Nd and co-doping of Ho and Nd foreign atoms in the Y-123 superconducting matrix. In this respect, we calculate the grain size belonging to the compounds by means of Scherrer–Warren equation for the highest 5 intensities of diffraction lines [108, 109].

$$t = {0.941^{a}}\Big/{B\cos^{-}_{B}} \tag{3}$$

where t denotes the thickness of the crystallite size, λ is relation to the wavelength of the XRD source, Θ_B shows the Bragg angle, and B (in radian unit) is in association with the full width at half maximum (FWHM) of the Bragg peak. The results obtained are listed in Table 4.1, Table 4.2, Table 4.3 and Table 4.4, clearly. According to the table, the materials get larger and larger crystallite sizes with the enhancement of the Ho particles in the superconducting core up to x=0,100 after which the value tends to decrease towards to the local minimum size value of 37 nm, with the enhancement of the Nd particles in the superconducting core up to x=0,250 after which the value tends to decrease towards to the local minimum size value of 42 nm, with the enhancement of the Nd particles in the HcN superconducting core up to x=0,100 after which the value tends to decrease towards to the local minimum size value of 47 nm and the materials get smaller and smaller crystallite sizes with the enhancement of the Ho particles in the superconducting core up to x=0,250 and

decrease towards to the local minimum size value of 48 nm with worst crystallinity and connectivity between grains. This change in the average crystallite size confirms that why both the superconducting characteristics diminish rapidly and phase transits from orthorhombic to pseudotetragonal with the excess only Ho and only Nd nanoparticles inserted in the Y-123 superconducting core. This finding is even favored by the SEM images.

Finally, using the XRD patterns we determine the Lotgering index (*F*) of the materials mentioned to quantify the degree of *c*-axis orientation in the crystal structure [110, 111]. The *F* values calculated are given in Table 4.1, Table 4.2, Table 4.3 and Table 4.4.

Table 4.1: Experimental XRD results (cell parameters *a*, *b* and *c*, crystallite size, oxygen concentrations and Lotgering indices for the pure and Y-site Ho substituted bulk samples

	Ho content	Lattice parameters				Grain size	*F Values*
Samples	x	a (Å)	b (Å)	c (Å)	y(c)	(nm)	
YHo0	0,000	3,829	3,888	11,704	6,841	61	0,166
YHo1	0,025	3,824	3,884	11,716	6,759	68	0,174
YHo2	0,050	3,821	3,881	11,728	6,684	73	0,197
YHo3	0,100	3,819	3,880	11,734	6,638	82	0,259
YHo4	0,250	3,842	3,895	11,681	6,994	55	0,163
YHo5	0,500	3,896	3,901	11,677	7,019	37	0,141

Table 4.2: Experimental evidences of DC resistivity and XRD results for every superconducting samples of YNd

	Nd content	Lattice parameters				Grain size	*F Values*
Samples	x	a (Å)	b (Å)	c (Å)	y(c)	(nm)	
YNd0	0,000	3,838	3,890	11,621	6,606	65	0,73
YNd1	0,025	3,830	3,888	11,624	6,624	69	0,92
YNd2	0,050	3,826	3,887	11,667	6,913	74	0,137
YNd3	0,100	3,825	3,882	11,720	6,732	85	0,249
YNd4	0,250	3,814	3,881	11,735	6,635	93	0,252
YNd5	0,500	3,914	3,922	11,569	6,261	42	0,149

It is apparent from the table that the crystal plane alignments (texturing of the Y-123 superconducting grains) improve monotonously with ascending the Ho

and Nd inclusions in the system up to x=0,100 and y=0,250 beyond which degrade harshly due to the penetration of the excess Ho particles into the Y-123 matrix.

$$f_{(123)} = \frac{\sum I_{(00l)} + P_0 \sum I_{(hkl)}}{\sum I_{(hkl)} + P_0 \sum I_{(hkl)}} \quad (4)$$

where I gives the peak intensity of the present phase and P_0=0,07 for Y-123.

Table 4.3: Experimental evidences of DC resistivity and XRD results for every superconducting samples of HcN

	HcN content	Lattice parameters				Grain size	*F Values*
Samples	x	a (Å)	b (Å)	c (Å)	y(c)	(nm)	
HcN0	0,000	3,820	3,887	11,726	6,758	80	0,251
HcN1	0,025	3,819	3,879	11,735	6,723	84	0,261
HcN2	0,050	3,813	3,878	11,745	6,698	87	0,273
HcN3	0,100	3,781	3,870	11,797	6,684	93	0,289
HcN4	0,250	3,835	3,895	11,406	8,822	47	0,161
HcN5	0,500	…	…	…	…	…	…

Table 4.4: Experimental evidences of DC resistivity and XRD results for every superconducting samples of NcH

	NcH content	Lattice parameters				Grain size	*F Values*
Samples	x	a (Å)	b (Å)	c (Å)	y(c)	(nm)	
NcH0	0,000	3,811	3,881	11,739	6,606	93	0,255
NcH1	0,025	3,817	3,883	11,731	6,658	81	0,183
NcH2	0,050	3,822	3,884	11,726	6,696	62	0,175
NcH3	0,100	3,825	3,886	11,711	6,797	59	0,126
NcH4	0,250	3,831	3,889	11,698	6,877	48	0,117
NcH5	0,500	…	…	…	…	…	…

4.2 Electrical resistivity measurements

The influence of partial substitution of Y particles by Ho inclusions, the influence of partial substitution of Ba particles by Nd inclusions, the influence of partial substitution of co-doping on superconducting properties belonging to the bulk Y-123 polycrystalline compounds is analyzed by the temperature dependence of the transport (DC electrical resistivity) measurements in the temperature range of 10–300 K and the experimental results observed are graphically depicted in Figure 4.5, Figure 4.6 a, b, Figure 4.7, Figure 4.8, Figure 4.9 and Figure 4.10. Prior to the

serious discussions, it is to be mentioned here that both the transition temperatures and especially resistivity values belonging to the virgin and Y-site Ho substituted, Ba-site Nd substituted and Ho+Nd co-doped Y-123 superconductors are extremely dependent upon the concentration level of Ho inclusions, Nd inclusions inserted in the Y-123 crystal lattice. Moreover, the samples each present a sharp transition into the superconducting state below the critical onset temperature (T_c^{onset}) with the positive (dρ/dt) linear temperature dependence of resistivity as a result of the metallic behavior. This is in association with the electron-phonon interaction in the crystal structure [112, 113] or logarithmic divergence in density of states at the Fermi level [114-117]. Furthermore, Figure 4.5, Figure 4.6 a, and Figure 4.7, show that the normal state resistivity belonging to the superconducting Y-123 samples after T_c^{onset} value reduces monotonously with the enhancement in the Ho content level up to x=0,100 in YHo, and Nd content level up to y=0,250 in YNd and Nd content level up to y=0,100 in HcN, in due to both the increase of the metallic interaction between the superconducting grains and the optimization of the hole density and possible improvements in the lattice vibration [118, 119]. But, Figure 4.9, shows that the normal state resistivity belonging to the superconducting Y-123 samples after T_c^{onset} value rises monotonously with the enhancement in the Ho content level up to x=0,100 in NcH, in due to both the decrease of the metallic interaction between the superconducting grains and the optimization of the hole density and possible deteriorations in the lattice vibration. Regarding the room temperature (300 K) resistivity, the YHo5 samples, YNd5 samples, HcN4 samples and NcH4 samples obtain the highest resistivity value (8,15 mΩ cm), (8,61 mΩ cm), (10,9 mΩ cm) and (17,26 mΩ cm), respectively; on the other hand, the lowest resistivity value of 2,37 mΩ cm, 2,77 mΩ cm, 1,72 mΩ cm and 2,84 mΩ cm are attributed to the YHo3

compound, YNd4 samples, HcN3 samples and NcH0. In other words, the magnitude of the room temperature resistivity changes by about a factor of 4 with the variation of the Ho inclusions, by about a factor of 4 with the variation of the Nd inclusions, by about a factor of 6 with the variation of the HcN inclusions and by about a factor of 6 with the variation of the NcH inclusions in the Y-123 superconducting core. The main reason of the increase in the resistivity with the excess Ho, Nd impurities arises from the decrement in the mobile hole concentration (hole localization effect) of the Cu–sites in the Y-123 system, causing to the phase transition from optimally doped to the underdoped position in the crystal structure [120, 121]. Moreover, the thermodynamic fluctuations or the opening of spin-gap mechanism (regarded as the small curvatures above the T_c^{onset} values) confirm the penetration of the magnetic impurities (Ho and Nd nanoparticles) into the superconducting system [122]. This is a clue about the survival of the Cooper pairs even above the T_c values. Additionally, the temperature dependent-electrical resistivity measurement results enable us to find the onset critical transition (T_c^{onset}) and offset critical transition (T_c^{offset}) temperatures. One can encounter the numerical results of T_c^{onset} and T_c^{offset} in Table 4.5, Table 4.6, Table 4.7 and Table 4.8. Based on the table, all the values obtained increase with ascending the Ho impurities in the Y-123 superconducting matrix up to the critical value of x=0,100, with ascending the Nd impurities in the Y-123 superconducting matrix up to the critical value of y=0,250 and with ascending the HcN impurities in the Y-123 superconducting matrix up to the critical value of y=0,100 beyond which they degrade rapidly and in NcH T_c values decrease with ascending NcH impurities due to not only the decrease of the mobile hole concentration and average crystallite size but also the increase of the porosity and weak links between the grains [123]. This is in correspondence to the fact that the Ho inclusions, Nd inclusions and HcN

inclusions make the inherently overdoped nature of the Y-123 superconducting system change to optimally doped state until the case of the concentration level of x=0,100, y=0,250 and y=0,100, respectively. From the dopant level of x=0,100 and y=0,250 onwards there is a transition of optimally doped state to the underdoped state position of the Y-123 superconductors, meaning the decrement in the T_c^{offset} and T_c^{onset} values.

The maximum T_c^{offset} and T_c^{onset} values are found to be about 92,14 K and 94,38 K, respectively for the YHo3 sample whereas the YHo5 compound obtains the minimum values of 43,89 K (T_c^{offset}) and 90,12 K (T_c^{onset}). The maximum T_c^{offset} and T_c^{onset} values are found to be about 97,25 K and 98,93 K, respectively for the YNd4 sample whereas the YNd5 compound obtains the minimum values of 32,97 K (T_c^{offset}) and 54,4 K (T_c^{onset}). The maximum T_c^{offset} and T_c^{onset} values are found to be about 94,84 K and 97,22 K, respectively for the HcN3 sample whereas the HcN4 compound obtains the minimum values of 60,72 K (T_c^{offset}) and 84,92 K (T_c^{onset}). The maximum T_c^{offset} and T_c^{onset} values are found to be about 96,76 K and 98,13 K, respectively for the NcH0 sample whereas the NcH4 compound obtains the minimum values of 75,66 K (T_c^{offset}) and 99,51 K (T_c^{onset}).

HcN5 and NcH5 samples shown in Figure 4.8 and Figure 4.10 are semiconducting matter.

All the ρ-T graphs of samples are given following figures; Figure 4.5, Figure 4.6, Figure 4.7, Figure 4.8, Figure 4.9 and Figure 4.10.

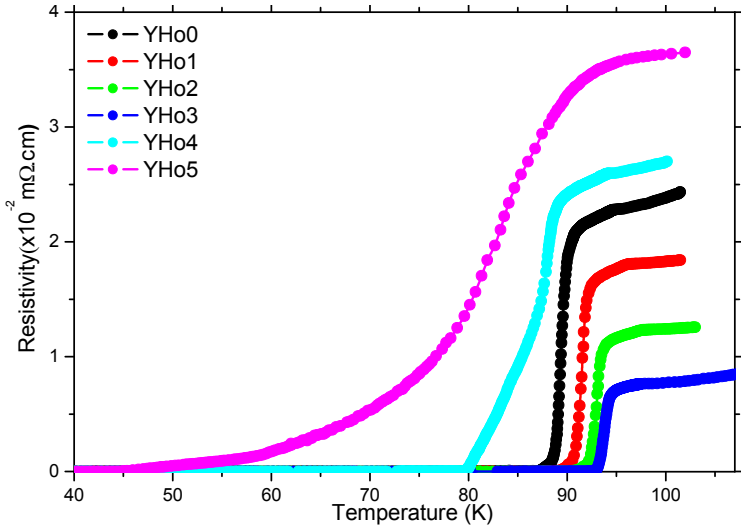

Figure 4.5: Temperature dependent-resistivity curves in the range of 40 K-110 K for the YHo superconducting materials

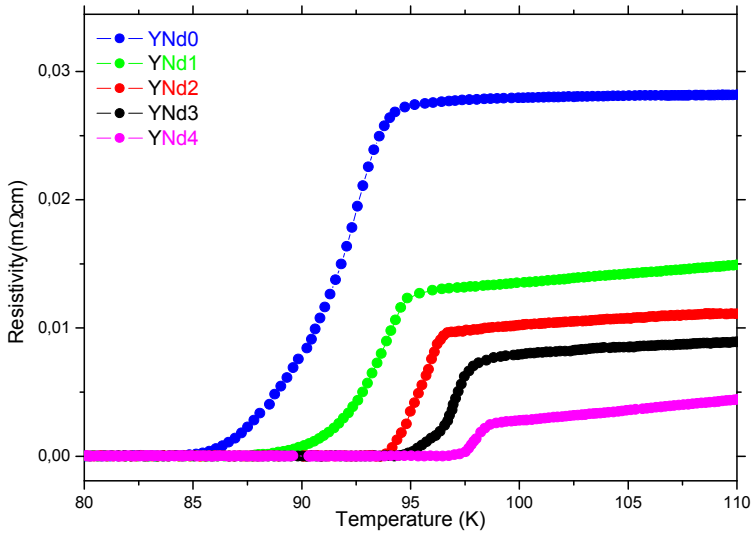

a)

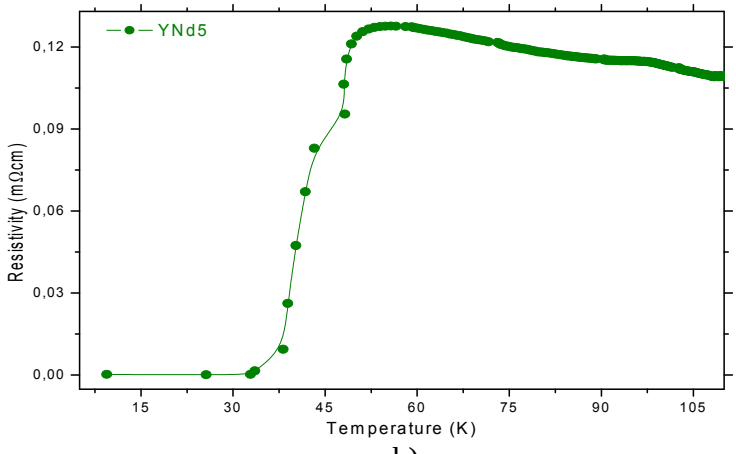

b)

Figure 4.6: Temperature dependent-resistivity curves for the YNd superconducting materials a) YNd0-YNd4 and b) YNd5

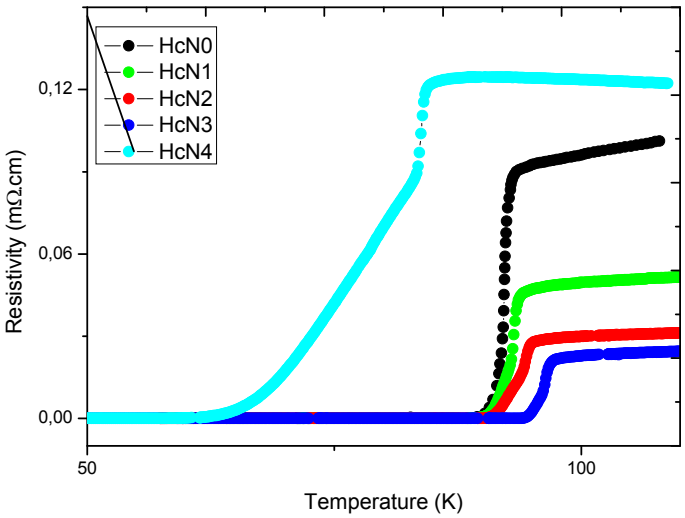

Figure 4.7: Temperature dependent-resistivity curves for the superconducting materials (HcN0-HcN4)

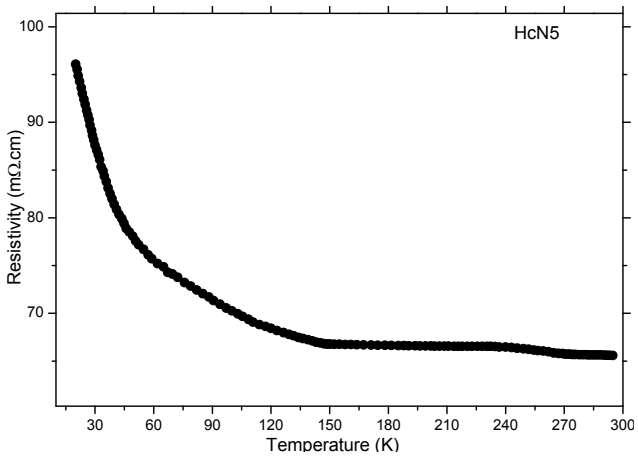

Figure 4.8: Temperature dependent-resistivity curves for the HcN5 samples

The long and short of it is that the optimum Ho and Nd concentration level in the crystal structure is noted to be x=0,100 and y=0,250 for the Y-123 superconducting phase formation as a consequence of the considerable improvement of the mobile hole concentration and interaction between the superconducting grains. Furthermore, it is to mentioned here that the variation of the former (T_c^{offset}) values are fairly higher than those in the latter (T_c^{onset}) values as a result of the change in the

oxygen content level in the superconducting crystal structure by the partial replacement of homovalent Ho-sites on the Y-sites and Nd-sites on Ba-sites.

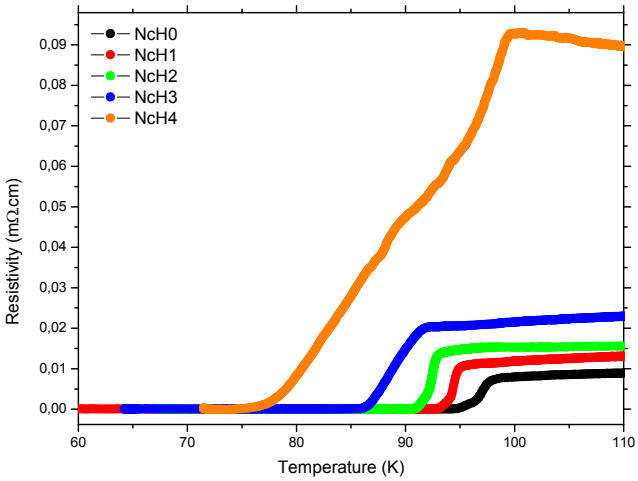

Figure 4.9: Temperature dependent-resistivity curves for the superconducting materials (NcH0-NcH4)

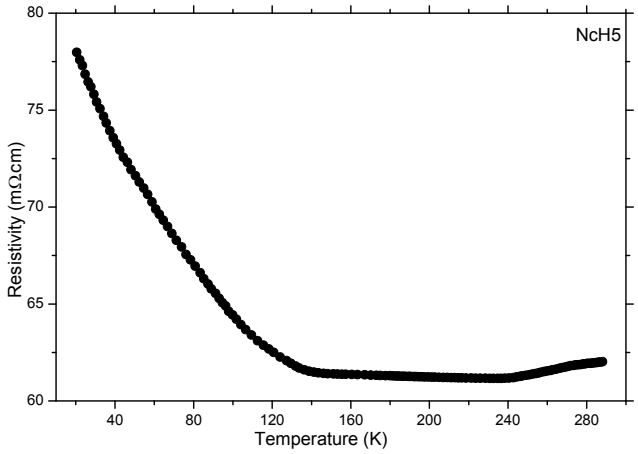

Figure 4.10: Temperature dependent-resistivity curves for the NcH5 samples

At the same time, the dramatic changes of the T_c^{offset} and T_c^{onset} values lead to the reduction/enhancement in the degree of the broadening (ΔT_c). In the present work, ΔT_c value is observed to decrease systematically from 3,41 K to 2,24 K with the increment of the Ho concentration level until x=0,100, from 10,17 K to 1,68 K with the increment of the Nd concentration level until y=0,250 and from 4,75 K to

2,38 K with the increment of the Nd concentration level until y=0,100 after this critical value the value begins to increase steeply towards to 46,23 K for YHo, to 21,87 K for YNd, to 24,2 K for HcN and ΔT_c value is observed to increase systematically from 1,37 K to 23,85 K with the increment of the Ho concentration level until x=0,250 due to both the increase of the porosity, grain boundary resistivity and weak-links in the crystal structure [124-126] and the absence of homogeneities (presence of CuO impurities) in the oxidation states of the superconducting grains [127].

4.3 Hole-carrier concentration calculation

The hole-carrier concentrations per Cu ion, *P*, are calculated by means of the following relation [128]:

$$P = 0.16 - \left[\left(1 - \frac{T_c}{T_c^{\max}}\right)/82.6\right]^{1/2} \tag{5}$$

where $T_c^{\max}$ is taken as 92 K for Y-123 phase [129] and 85 K for Y-124 phase [130] and T_c values are deduced form Figure 4.5, Figure 4.6 a, b, Figure 4.7 and Figure 4.9.

The compound is doped maximum and T_c is maximum at $P=P_0=0,16$. The hole-carrier concentration of the YHo3, YNd4, HcN3 and NcH0 samples obtaining the highest critical temperature is observed to be greater than the others (Table 4.5, Table 4.6, Table 4.7 and Table 4.8).

Table 4.5: Experimental evidences of bulk density, porosity, dc resistivity and transport critical current density for every superconducting sample of YHo

Samples	Ho content x	T_c^{onset}(K)	T_c^{ofset}(K)	ΔT_c (K)	$\rho_{300\,k}$ (mΩ cm)	J_c (A cm^{-2})	Hole carrier (n)	ρ (g/cm^3)	P (%)
YHo0	0,000	90,45	87,04	3,41	5,89	132	0,177	6,101	4,027
YHo1	0,025	92,08	88,76	3,32	3,31	186	0,183	6,137	3,461
YHo2	0,050	93,46	90,27	3,19	2,62	215	0,195	6,159	3,115
YHo3	0,100	94,38	92,14	2,24	2,37	232	0,236	6,186	2,69
YHo4	0,250	87,60	78,49	9,11	6,24	98	0,171	5,805	8,683
YHo5	0,500	90,12	43,89	46,23	8,15	71	0,17	5,683	10,60

Table 4.6: Experimental evidences of bulk density, porosity, dc resistivity and transport critical current density for every superconducting sample of YNd

Samples	Nd content x	T_c^{onset}(K)	T_c^{ofset}(K)	ΔT_c (K)	300K (mΩ cm)	J_c (A cm^{-2})	Hole carrier (n)	ρ (g/cm^3)	P (%)
YNd0	0,000	94,69	84,52	10,17	7,89	92	0,129	6,023	4,397
YNd1	0,025	95,41	88,44	6,97	7,45	139	0,138	6,124	2,794
YNd2	0,050	96,9	93,62	3,28	6,5	183	0,145	6,179	1,921
YNd3	0,100	98,13	94,88	3,25	4,19	207	0,141	6,205	1,508
YNd4	0,250	98,93	97,25	1,68	2,77	224	0,134	6,221	1,254
YNd5	0,500	54,84	32,97	21,87	8,61	86	0,072	5,901	6,333

Table 4.7: Experimental evidences of bulk density, porosity, dc resistivity and transport critical current density for every superconducting sample of HcN

Samples	HcN content x	T_c^{onset}(K)	T_c^{ofset}(K)	ΔT_c (K)	$\rho_{300\ K}$ (mΩ cm)	J_c (A $cm^{-2)}$	Hole carrier (n)	ρ (g/cm^3)	P (%)
HcN0	0,000	93,97	89,22	4,75	2,32	225	0,141	6,087	3,381
HcN1	0,025	94,22	89,97	4,25	2,25	237	0,143	6,133	2,651
HcN2	0,050	95,03	91,45	3,58	1,96	243	0,151	6,157	2,270
HcN3	0,100	97,22	94,84	2,38	1,72	251	0,140	6,214	1,365
HcN4	0,250	84,92	60,72	24,2	10,9	97	0,096	5,961	5,381
HcN5	0,500	…	…	…	…	…	…	…	…

Table 4.8: Experimental evidences of bulk density, porosity, dc resistivity and transport critical current density for every superconducting sample of NcH

Samples	NcH content x	T_c^{onset} (K)	T_c^{ofset} (K)	ΔT_c (K)	$\rho_{300\ K}$ (mΩ cm)	J_c (A cm^{-2})	Hole carrier (n)	ρ (g/cm^3)	P (%)
NcH0	0,000	98,13	96,76	1,37	2,84	225	0,15	6,278	0,476
NcH1	0,025	95,03	93,35	1,68	3,97	210	0,147	6,192	1,746
NcH2	0,050	93,15	91,27	1,88	5,18	195	0,135	6,175	1,984
NcH3	0,100	91,7	86,51	5,19	7,95	150	0,133	5,984	5,079
NcH4	0,250	99,51	75,66	23,85	17,26	100	0,114	5,736	9,048
NcH5	0,500	…	…	…	…	…	…	…	…

4.4 Transport critical current density

In this part of the paper, the critical current density (J_c) measurements enable us to investigate the effect of the Ho and Nd inclusions inserted in the Y-123 system on both the flux pinning mechanism and quality of the interaction between the grains in the crystal structure. As well-known J_c can be defined as the resistance against the applied temperature, current and magnetic field and the cuprate superconductors have a crucial handicap such as the easy motion of their vortices due to the grain misorientations [131]. In the present work, we try to improve the

corruption characteristic belonging to the Y-123 bulk superconductors using highly dispersed Ho nanoparticles and Nd nanoparticles leading to the introduction of the nucleation centers (effective flux pinning centers) into the crystal structure. According to the experimental results obtained, the self-field J_c value is found to increase from 132 A.cm^{-2} (for the pure sample) to 384 A.cm^{-2} (for the YHo3 compound) with the enhancement of the Ho particles in the Y-123 matrix up to the certain content value of x=0,100 beyond which it tends to reduce rapidly to 98 A.cm^{-2} and in fact reaches to local minimum point of 71 A.cm^{-2} at the constant temperature of 77 K, the self-field J_c value is found to increase from 92 A.cm^{-2} (for the pure sample) to 224 A.cm^{-2} (for the YNd4 compound) with the enhancement of the Nd particles in the Y-123 matrix up to the certain content value of y=0,250 beyond which it tends to reduce rapidly to 86 A.cm^{-2} at the constant temperature of 77 K, the self-field J_c value is found to increase from 225 A.cm^{-2} (for the Ho constant sample) to 251 A.cm^{-2} (for the HcN3 compound) with the enhancement of the Nd particles in the Y-123 matrix up to the certain content value of y=0,100 beyond which it tends to reduce rapidly to 97 A.cm^{-2} at the constant temperature of 77 K, the self-field J_c value is found to decrease from 225 A.cm^{-2} (for the Nd constant sample) to 100 A.cm^{-2} (for the NcH4 compound) with the enhancement of the Ho particles in the Y-123 matrix up to the certain content value of x=0,250 at the constant temperature of 77 K. The systematic increase in the J_c values is related to tight bonding of the Ho nanoparticles and Nd nanoparticles to the nucleation centers [132, 133]. On the other hand, the considerable decrease in the J_c value with the excess Ho atoms and Nd atoms can stem from the defects (deterioration of the flux pinning centers) such as the pores, hole localization effect, voids, stacking faults, planar and micro defects (twin, domains etc.) and weak links between the superconducting grains and grain

boundary resistivity [134]. It is another interesting result is that the J_c value is more sensitive to the Ho and Nd individuals in the Y-123 matrix than the T_c value.

An improvement of the J_c value is associated with not only the reduction of the porosity and weak links between the superconducting grains but also the increase in the flux pinning centers, the average length of the cell parameter *c*, the grain size and their orientations [135]. Hence, researchers have been made an effort to enhance the effective pinning centers such as planar defects, stacking faults and micro-defects with the aid of methods such as chemical doping, substitution, transition metal evaporation and changing preparation condition including the annealing ambient, operational procedure, composition, heat-treatment, dopant type and quantity [18-21]. In substitution process, the variation of the some significant superconducting properties (critical current density, onset and offset critical temperatures, etc.) of the samples studied is related with the information obtained about both the location and charge of doping metals. In other words, this technique is the most efficient in order to access the some crucial clues about the mechanism of high-temperature superconductivity [136, 137].

In other words, the critical current density in the crystals can be improved by introducing the effective flux pinning centers. As well known, when a magnetic field applies to a type-II superconductor it penetrates into the material in the form of vortices. Each vortex carries a flux quantum $\Phi = h/2e$, and consists of both a cylindrical core of a radius ξ (called as coherence length) and a current circulating around the core out to a distance λ (named as penetration depth of the material) [138]. Therefore, the current flowing into the superconductor material generates the energy dissipation as a result of the Lorentz force, leading to the mobility of vortices and the disappearance of superconductivity in the material.

Nevertheless, the vortices mobility can be minimized by introducing defects which pin these vortices. Hence, the J_c value of a material is in accordance with the flux pinning of vortices. Besides, an effective flux pinning centers in a material can easily be produced by means of the defects such as stacking faults, pores/voids, screw dislocations, twin boundaries, planar and micro-defects [139].

4.5 SEM Analyses

The surface morphologies belonging to the virgin, Y-site Ho substituted, Ba-site Nd substituted and Ho+Nd substituted bulk superconducting materials are depicted in the secondary electron image mode at 3000X and 5000X magnification via the scanning electron microscopy investigations. The images obtained are displayed in Figure 4.11 a-f, Figure 4.12 a-f, Figure 4.13 a-c and Figure 4.14 a-c.

Based on the figure, it can easily be said that the Ho foreigners and the Nd foreigners inserted in the Y-123 system make the specimen morphologies change seriously. Namely, with the increment of the Ho and Nd individuals in the Y-123 core and Nd individuals in HcN up to the critical value of x=0,100, y=0,250 and y=0,100, respectively, the microstructural properties regularly improve owing to the presence of the dense surface with a fine connectivity between the grains.

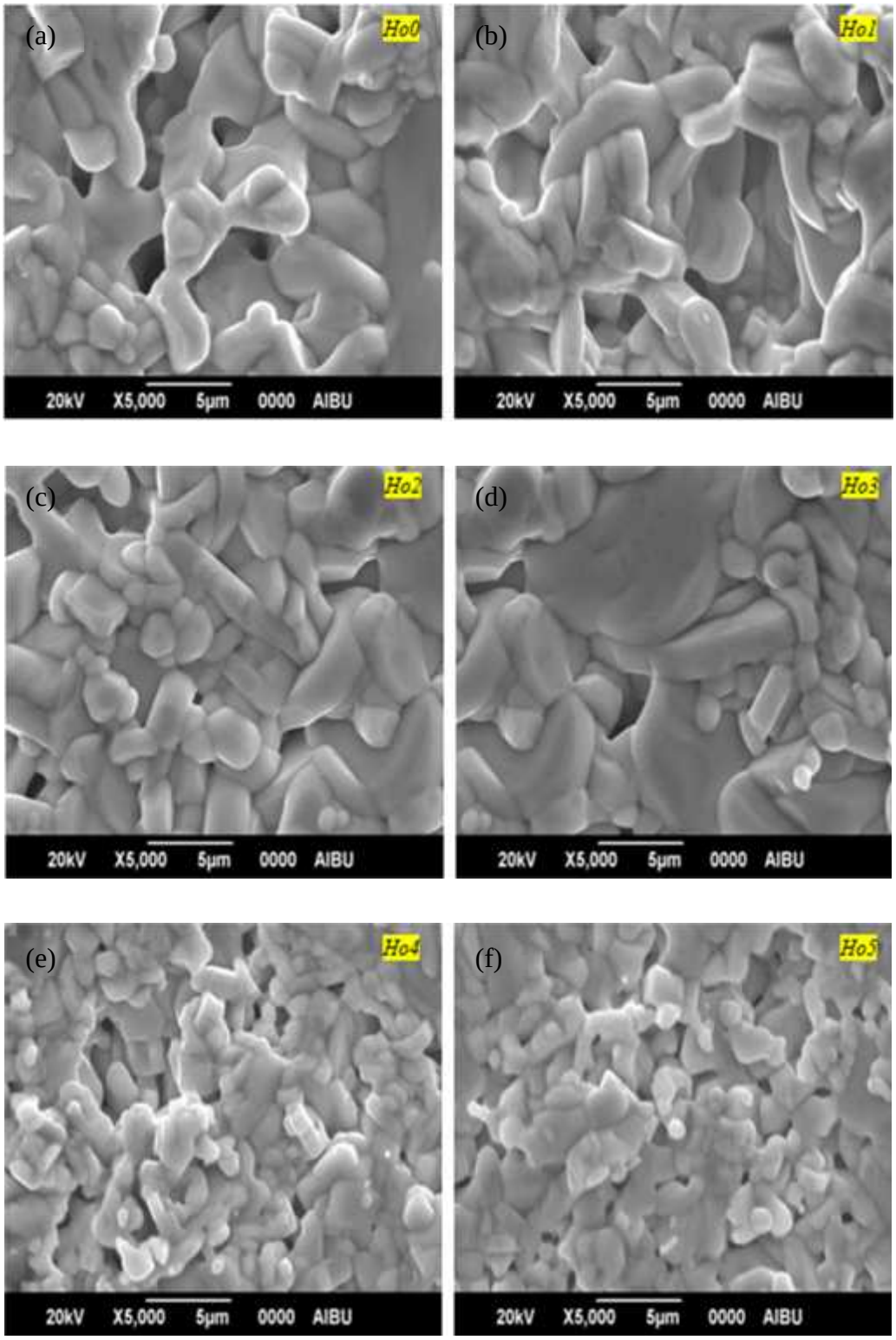

Figure 4.11: *SEM* micrographs belonging to a) pure, b)YHo1, c) YHo2, d) YHo3, e) YHo4 and f) YHo5 materials

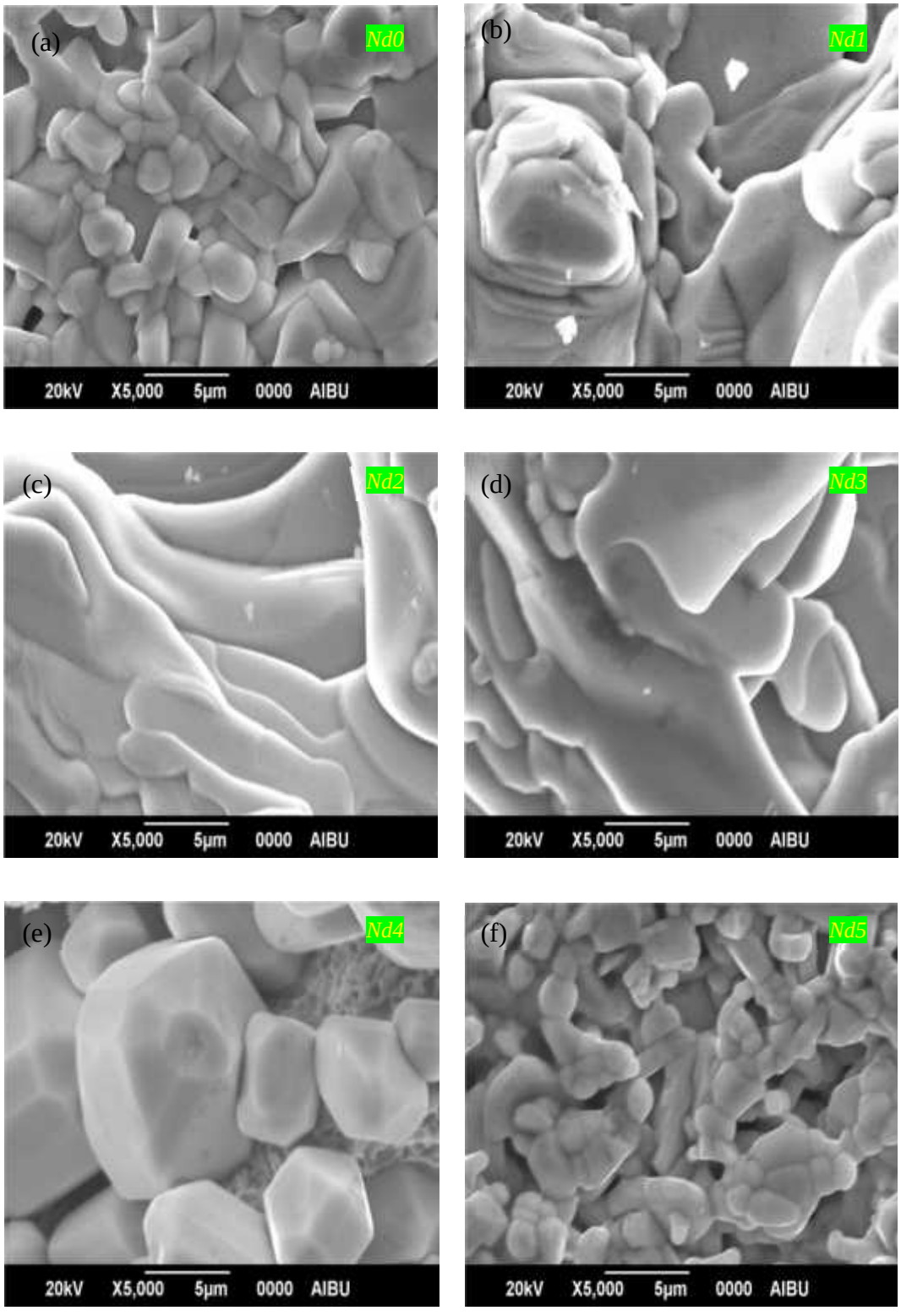

Figure 4.12: *SEM* micrographs for all YNd materials

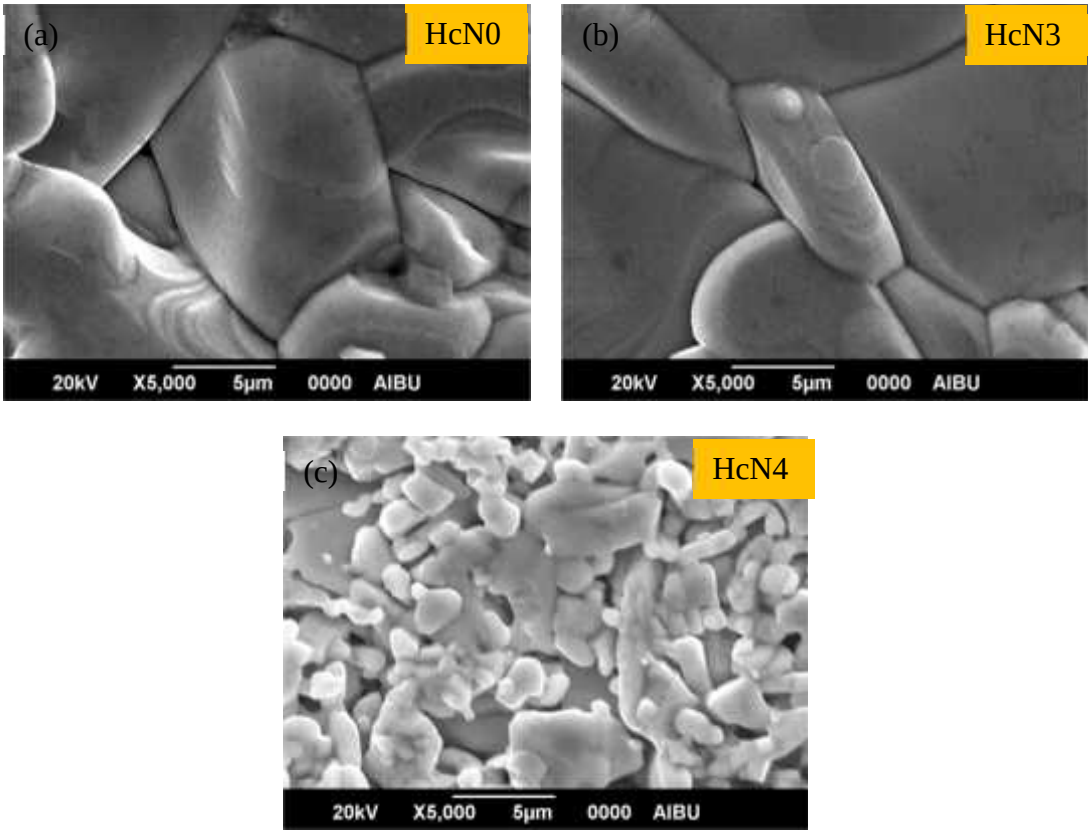

Figure 4.13: *SEM* micrographs for a) HcN0, b) HcN3 and c) HcN4 materials

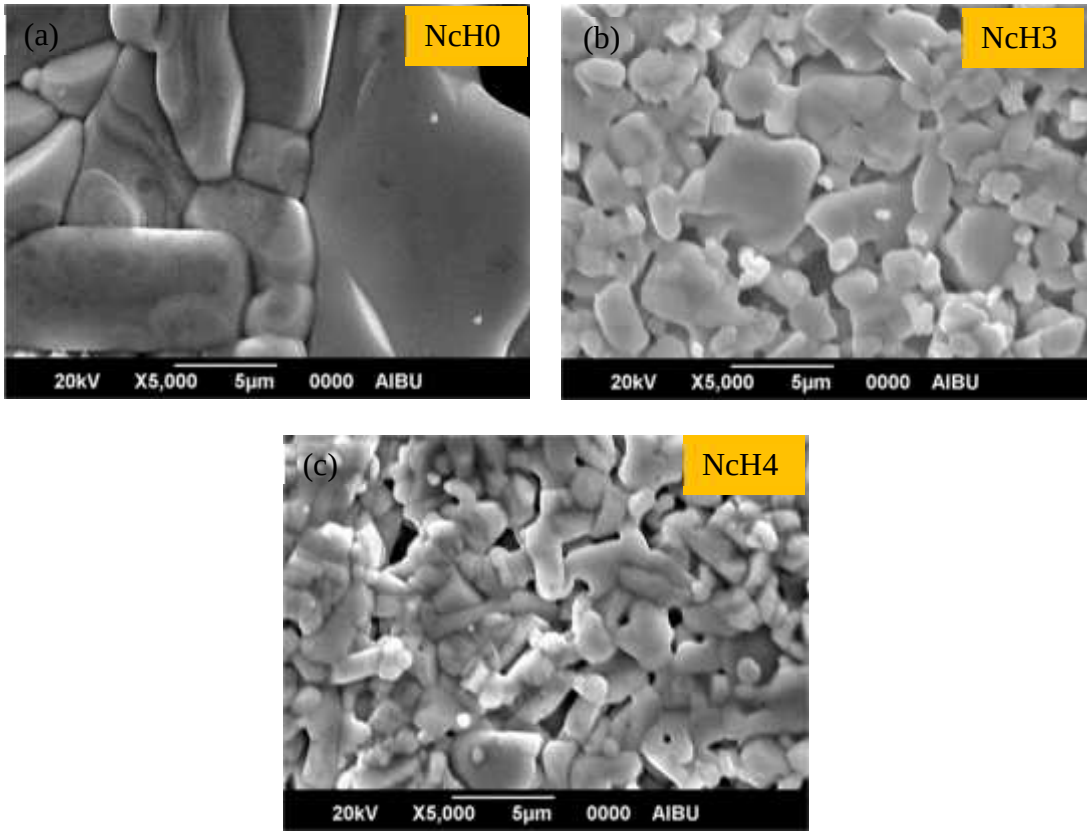

Figure 4.14: *SEM* micrographs for a) NcH0, b) NcH3 and c) NcH4 materials

However, from the Ho concentration level of x=0,100 in YHo, from the Nd concentration level of y=0,250 in YNd, Nd concentration level of y=0,100 in HcN onwards and for Ho concentration level in NcH, the surface morphology begins to deteriorate and in fact, it just gets worse and worse due to the existence of the porosity, partial melting, voids and cracks causing to new phase formations in the crystal structure. Here, it should be noted that we have already encountered the different minor phases ($BaCuO_2$; Y-247 and Y-124) for the YHo5 sample, YNd5 sample, HcN4 sample and NcH4 sample.

Moreover, among the superconducting samples, the YHo3 material, YNd4 material, HcN3 sample and NcH0 sample obtains the smoothest and densest surface morphology with the most uniform surface appearance, largest crystalline (particle) size, best texturing, lowest porosity, best crystallinity and interaction between the superconducting grains. The long and short of it is that these samples except HcN5 and NcH5 exhibit completely the basic characteristics of Y-123 phase, being in good agreement with the Lotgering index data deduced from the XRD diffraction graphs.

4.6 EDS Analyses

The local chemical composition investigations of the bulk samples are quantitatively surveyed by means of the Electron Dispersive Spectroscopy (EDS) method to obtain more detailed information about the material microstructures. The experimental evidences observed are pictured in Figure 4.15 a, b, Figure 4.16 a-f and Table 4.9 in details. The former representative images show the detailed EDS analyses for the pure and Y-site Ho substituted Y-123 superconducting compounds while the latter pictures illustrate the Y, Ba, Cu, Ho and O element composition mappings taken from nano-scale grains on the specimen surfaces belonging to each

of the sample. That no extra peaks appear between two pictorials except for the Ho peaks is obvious from Figure 4.15 a (pure sample) and b (YHo3 sample), confirming that all the elements given above enter successfully into the Y-123 superconducting matrix [120]. Additionally, it is another probable result deduced from the curves that the peak intensities belonging to the cupper and especially yttrium elements retrograde appreciably with the existence of the holmium nanoparticles in the superconducting matrix.

This is attributed to the fact that the Ho inclusions inserted in the Y-123 system may substitute for the Cu and Y elements, and hence there seems to be a rapid decrement in the superconducting properties such as critical temperature and critical current density value of the Y-123 samples

Regarding Figure 4.16 a-f, one can observe that for all the materials the element distribution is almost uniform (homogeneous) on the whole area scanned.

It would be more precise to say that among the compounds, the Cu element (symbolized by green dots) and Y (given by blue dots) element distributions in the YHo5 sample are found to be lower as compared to the other samples. This is related to the fact that this material exhibits less superconducting properties. Moreover, the same sample obtaining the highest O element distribution in the superconducting matrix may cause to degrade in the superconducting properties.

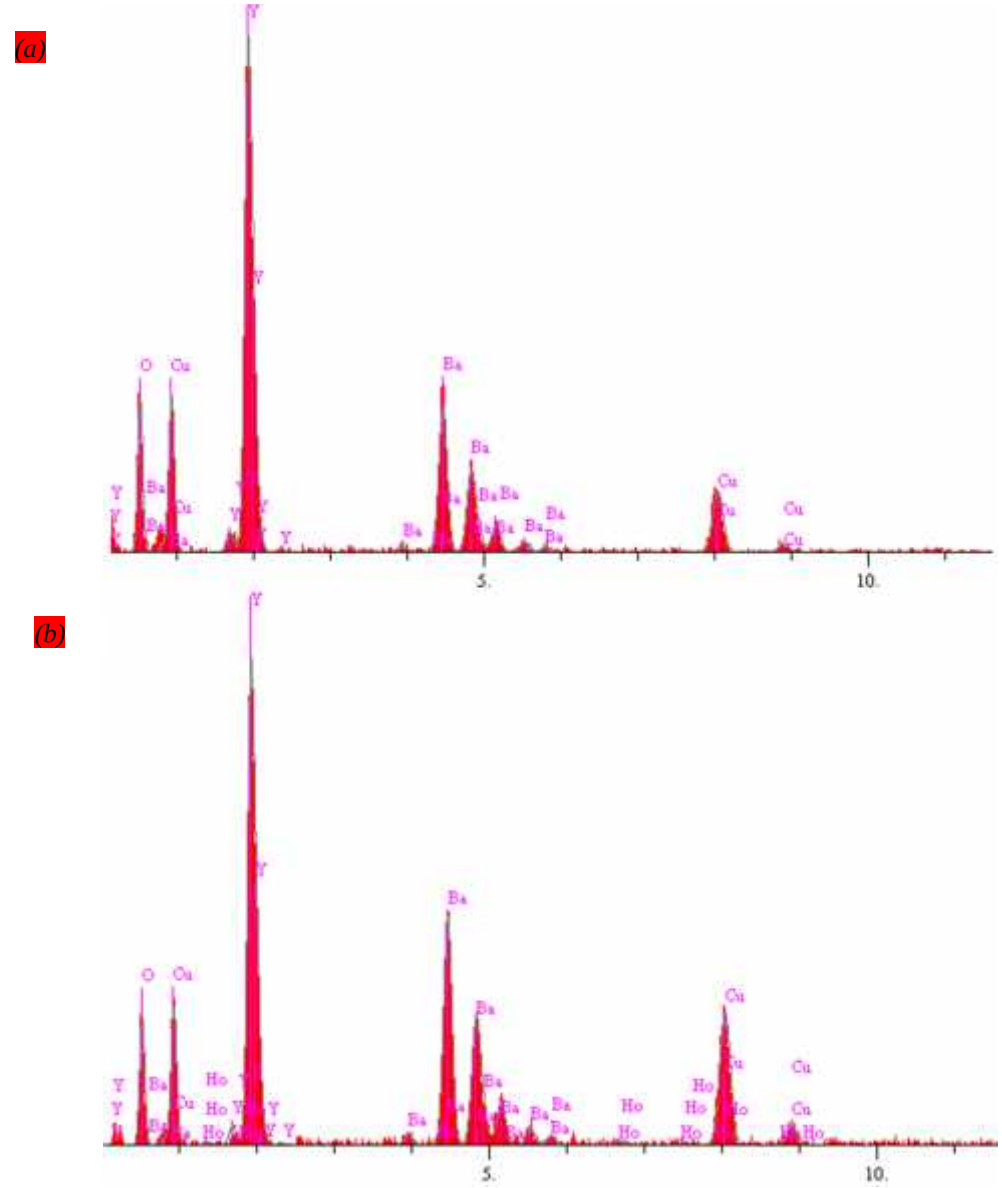

Figure 4.15: EDS image of the element distributions for (a) pure and (b) YHo3 compound

Table 4.9: Element concentrations in the superconductors

Component	Line	Concentration (wt.%)					
		YHo0	YHo1	YHo2	YHo3	YHo4	YHo5
O	K_α	15,982	15,665	15,402	15,021	16,205	16,886
Cu	K_α	21,445	21,864	21,919	23,176	21,206	20,827
Y	K_α	14,719	14,011	13,641	12,203	11,801	9,155
Ba	L_α	47,854	47,396	47,453	46,867	47,021	46,989
Ho	L_α	----------	1,064	1,585	2,733	3,767	6,143

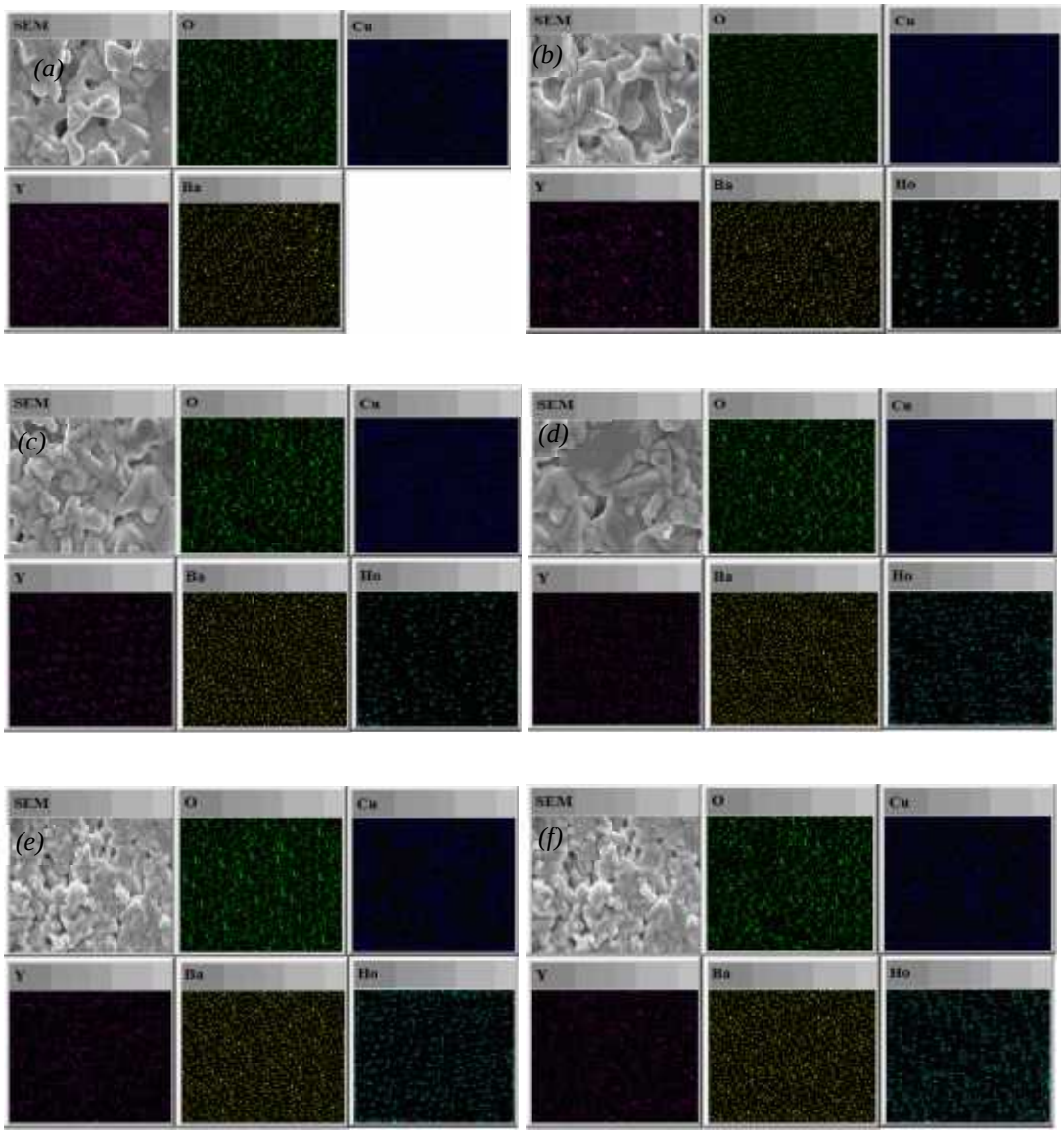

Figure 4.16: EDS maps of a) YHo0, b) YHo1, c) YHo2, d) YHo3, e) YHo4 and f) YHo5

4.7 The bulk density and porosity analyses

Here, Archimedes water displacement method allows us to examine directly the change of transport properties belonging to the grain boundaries in the Y-123 bulk superconducting materials. The calculated relative densities of the ceramics are inferred from the density of pure Y-123 system (approximately 6,357 g/cm^3) [102]. The relative densities computed are numerically tabulated in Table 4.5. As seen from the table, similar to the evidences in other parts, the density value is observed to

enhance from 6,101 g/cm^3 (for the virgin compound) with 6,186 g/cm^3 (for the YHo3 sample) increasing the Ho inclusions in the Y-123 system up to the certain value of x=0,100 beyond which the value decreases drastically towards to 5,683 g/cm^3 (for the YHo5 material). It is attributed to the fact that the microstructural properties improve with the Ho impurities until the critical value of x=0,100 owing to the enhancement of the interaction between the superconducting grains, and the YHo3 sample contains the highest level of CuO (favored by the EDS examination). However, the excess Ho particles damage the texturing and crystallinity, being favored by the experimental findings of the dc resistivity and SEM examinations. Additionally, one can define the porosity values known as the granularity degree via the two available methods described in [140-143] to discuss the strength of connection between superconducting grains. The calculations are also depicted in the same table. It is visible from the table that the porosity values tend to decrease gradually with increasing the Ho content in the Y-123 system as a consequence of the partially filling of the pores in the crystal structure up to the concentration value of x=0,100 after which the porosity begins to decrease significantly and in fact the YHo5 superconducting material obtains the largest pores along with the weakest connection between the superconducting grains. This fact confirms that why the microstructural and superconducting properties suppress with the excess concentration of Ho impurities in the Y-123 superconducting matrix.

From the Table 4.6, the density value is observed to enhance from 6,023 g/cm^3 (for the virgin compound) with 6,221 g/cm^3 (for the YNd4 sample) increasing the Nd inclusions in the Y-123 system up to the certain value of x=0,250 beyond which the value decreases drastically towards to 5,901 g/cm^3 (for the YNd5 material).

As seen from the Table 4.7, similar to the evidences in other parts, the density value is observed to enhance from 6,087 g/cm^3 (for the HcN0 compound) with 6,214 g/cm^3 (for the HcN3 sample) increasing the Nd inclusions in the Y-123 system up to the certain value of x=0,100 beyond which the value decreases drastically towards to 5,961 g/cm^3 (for the HcN5 material).

According to the Table 4.8, the density value is observed to decrease from 6,278 g/cm^3 (for the NcH0 compound) with 5,736 g/cm^3 (for the NcH4 sample) increasing the Ho inclusions in the Y-123 system.

4.8 Vickers microhardness analyses

Y-123 superconducting material survives with its own inherit brittleness nature because of the grain boundary weak-link problems. Hence, the compound obtains poor mechanical properties and is not generally preferred in the potential mechanical applications [140, 144]. In the comprehensive work, we try to improve the mechanical performances by the partial substitution of Y inclusions for Ho particles and the partial substitution of Ba inclusions for Nd particles in the crystal structure. Vickers microhardness measurements are the best known method to determine mechanical characteristics of the superconducting compound. In this technique, the variation of the diagonal length against the different applied indentation test load (0,245 N - 2,940 N) gives the real (load independent) microhardness values of the superconductors by using the following equation.

$$H_V = 1854\ .4\left(\frac{F}{d^2}\right) \tag{6}$$

where F displays the test load when d (in the unit of μm) is relation to the mean diagonal length of the indentation impression. The microhardness values obtained from the equation are graphically depicted in Figure 4.17, Figure 4.21 a, b and Figure

4.25 for YHo, Figure 4.18, Figure 4.22 a, b and Figure 4.26 for YNd, Figure 4.19, Figure 4.23 a, b and Figure 4.27 for HcN and Figure 4.20, Figure 4.24 a, b and Figure 4.28 for NcH in detail. At the first glance, the figures address that Vickers microhardness values belonging to each sample tend to increase with the enhancement of the applied load (linear microhardness) until the maximum test load of 2,940 N. This is associated with the fact that the pure and Y-site Ho substituted samples and the pure and Ba-site Nd substituted samples, in which the plastic deformation is superior to the elastic deformation (no elastic recovery), exhibit the typical Rise Indentation Size Effect (*RISE*) behavior under the applied indentation test load. Moreover, it is another probable result extracted from the figure that the real (true) microhardness values ascend regularly with the enhancement of the Ho content level up to x=0,100 in YHo, the Nd content level up to y=0,250 in YNd, and Nd content level up to y=0,100 in HcN beyond which and for Ho content in NcH, the load independent values decrease rapidly due to the increase of the specimen cracking/porosity, minor phases, grain boundary weak-links and irregular grain orientation distribution [144]. Conversely, the best quality of crystallinity and interaction between the superconducting grains ascribe to the YHo3, YNd4, HcN3 and NcH0 samples, being even favored by the XRD and SEM experimental findings. Furthermore, the load independent results obtained allow us to theoretically calculate the elastic (Young's) modulus (E) and yield strength (Y) parameters. That is to say,

$$E = 81.9635 H_V \tag{7}$$

$$Y \approx \frac{H_V}{3} \tag{8}$$

The calculations are numerically listed in Table 4.10, Table 4.12, Table 4.14 and Table 4.16. It is apparent from the table that, similar to the other experimental findings, the ceramic characteristics (E, Y and H_v values calculated) initially improve

with the Ho concentration until the certain value of x=0,100 in YHo, with the Nd concentration until the certain value of y=0,250 in YNd and with the Nd concentration until the certain value of y=0,100 in HcN owing to the perfection of the crystallinity and the strength in the connectivity between the superconducting grains. After these critic values and for NcH, all the values degrade harshly as a consequence of the excess penetration of the homovalent Ho-sites on the Y-sites and the homovalent Nd-sites on the Ba-sites resulting in the increment of the grain boundary weak-links.

At the same time, we depict the variation of elastic modulus against the experimental bulk density belonging to each compound in Figure 4.25, Figure 4.26, Figure 4.27 and Figure 4.28. One can deduce from Figure 4.25, Figure 4.26, Figure 4.27 and Figure 4.28 that the *E* values tend to ascend parabolically with the increment in the bulk densities, confirming the enhancement in both the crystallite size and interaction between the superconducting grains up to x=0,100 for YHo, y=0,250 for YHo and y=0,100 for HcN beyond and confirming the decrement in both the crystallite size and interaction between the superconducting grains up to x=0,250 for NcH, which the values in the y axis of the graphic decrease drastically. According to the discussions given above, it is not wrong to utter that the YHo3 compound with the greatest bulk density obtains the maximum *E* value of 71,80 GPa whereas the minimum value of 22,13 GPa is attributed to the YHo5 one, the YNd4 compound with the greatest bulk density obtains the maximum *E* value of 170,32 GPa whereas the minimum value of 28,77 GPa is attributed to the YNd5 one, the HcN3 compound with the greatest bulk density obtains the maximum *E* value of 97,04 GPa whereas the minimum value of 33,77 GPa is attributed to the HcN5 one and the NcH0 compound with the greatest bulk density obtains the maximum *E* value

of 170,32 GPa whereas the minimum value of 33,77 GPa is attributed to the NcH5 one. Moreover, it is pertinent to mention here that for all the samples the changes in the *E* values at the smaller indentation test loads are found to be higher than those at the higher test loads. This confirms that there is not a sublimit for the beginning of the plastic deformation and so their own plastic deformation plays dominant character on the superconducting materials at every test load applied.

As for the theoretical modeling of the Y-site Ho substituted and the Ba-site Nd substituted Y-123 superconducting compound, we use only Hays–Kendall (HK) approach and indentation-induced cracking (IIC) model due to their useful and reliable features [145, 146]. As well known, the former technique is generally successful for the explanation of the Vickers microhardness for the materials exhibiting the indentation size effect ISE behavior whereas the latter one is known to be the best model to describe the microhardness values of the compounds obeying the RISE nature. In HK model, there is a maximum test load (W) where the dominant character of plastic (irreversible) deformation begins to substitute for that of elastic (reversible) deformation in the material [147]. As a result, the indentation size is determined from the proportional to an effective load $F_{eff}=F-W_{HK}$. Namely,

$$F - W = A\, d^2 \tag{9}$$

where *W* denotes the load independent constant, and the parameters of *A* and *W* deduced from the linear graphs of *F* versus d^2 (Figure 4.21 a, Figure 4.22 a, Figure 4.23 a and Figure 4.24 a) are numerically depicted in Table 4.11, Table 4.13, Table 4.15 and Table 4.17. As seen from the table all the W values belonging to the samples mentioned in this work are found to be negative due to the *RISE* nature in their crystal structures. Moreover, it is noteworthy that the YHo3, YNd4, HcN3 and NcH0 samples have the maximum *A* value, assuring that this sample exhibits the best

structural characteristics. At the same time, the true hardness values (H_{HK}) are calculated from the following formula:

$$H_{HK} = 1854.4A \tag{10}$$

On the other hand, in the IIC model, the indentation test load applied is balanced by the total sample resistance at the maximum depth value because of the four important components: (I) the friction at the indenter (specimen facet interface), (II) elastic deformation, (III) plastic deformation and (IV) specimen cracking [148].

Hence, the real microhardness value (H_{IIC}) can be determined from the following equation:

$$H_v = K\left(\frac{F^{5/3}}{d^3}\right)^m \tag{11}$$

where *K* and *m* are attributed to load independent constants given in Table 4.14 and Table 4.15. The real microhardness values are computed from the graph of [*ln* (H_v)] *vs* [*ln*$(F^{5/3}/d^3)$] as visualized in Figure 4.21 and Figure 4.23. According to the results obtained, each m value is found to be lower than the number of 0,6 (m < 0,6), meaning that every sample obeys *RISE* behavior [146]. It is another interesting result that the results of the *IIC* model are very close to the plateau region as compared to those of the *HK* one (Table 4.16 and Table 4.17). This is attributed to the fact that the IIC model is quite superior to the *HK* approach to explain the microhardness properties of the virgin and Y-site Ho and Ba-site Nd substituted Y-123 superconducting materials.

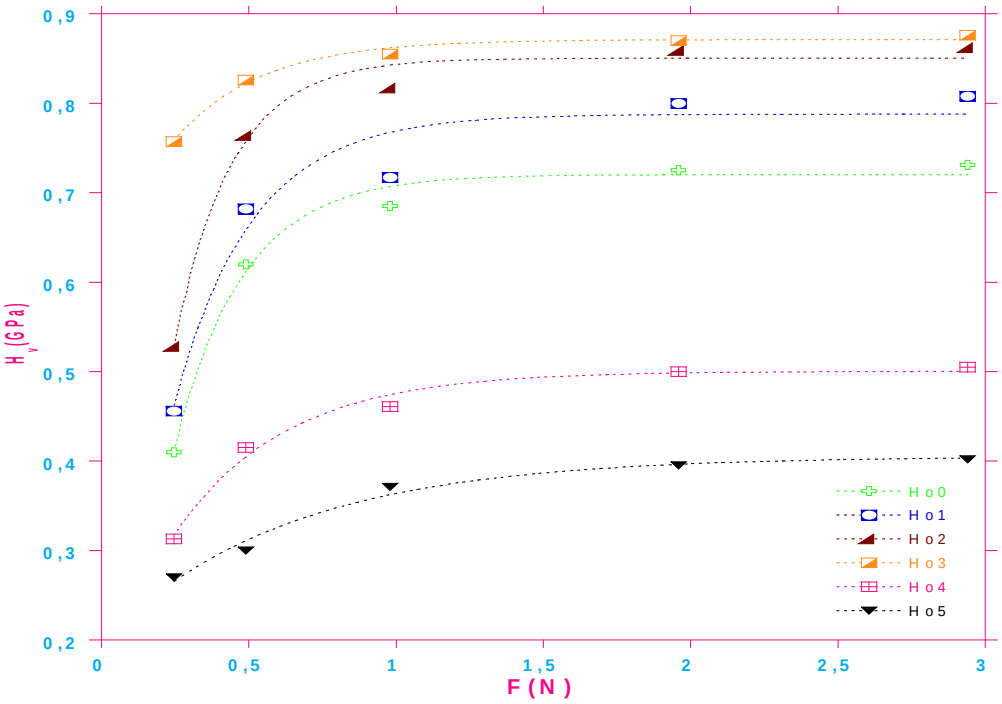

Figure 4.17: Effect of the applied indentation test loads on the Vickers microhardness evidences of the YHo-123 bulk superconductors

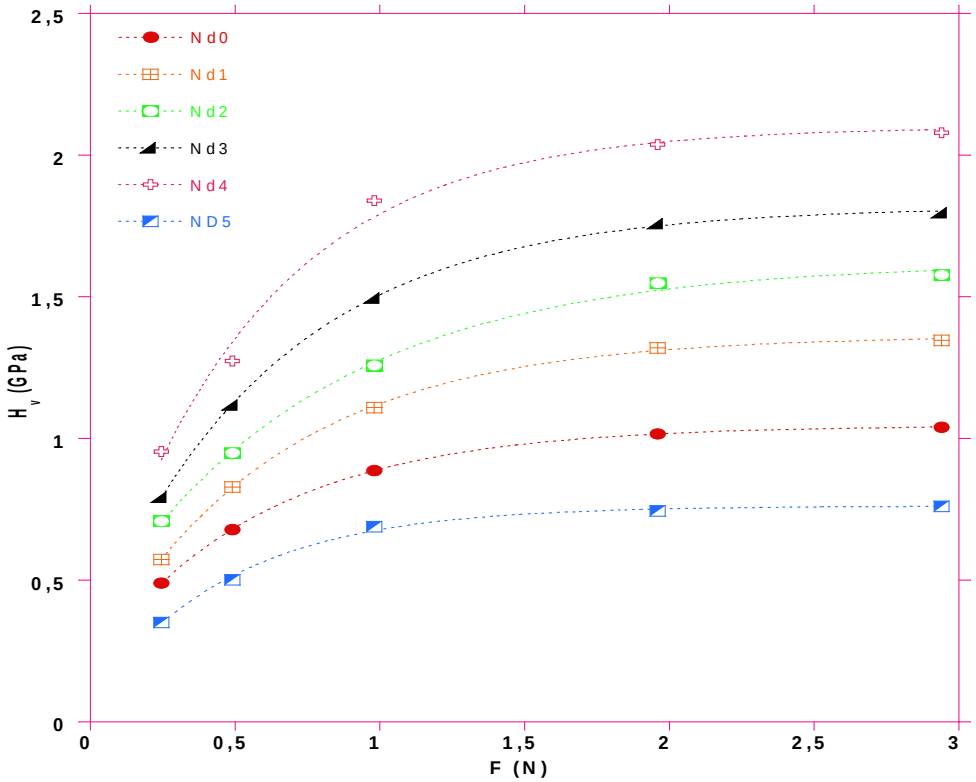

Figure 4.18: Effect of the applied indentation test loads on the Vickers microhardness for YNd

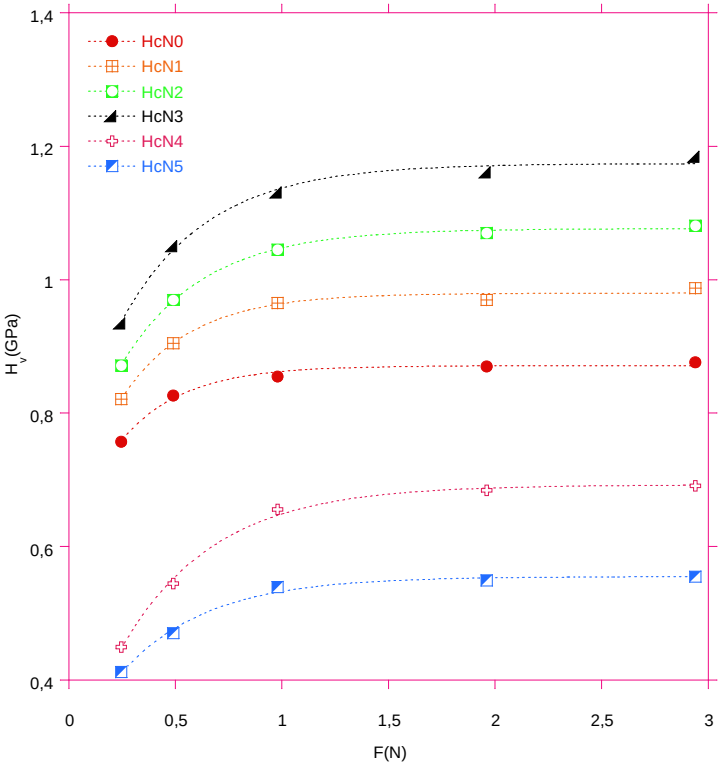

Figure 4.19: Effect of the applied indentation test loads on the Vickers microhardness for HcN

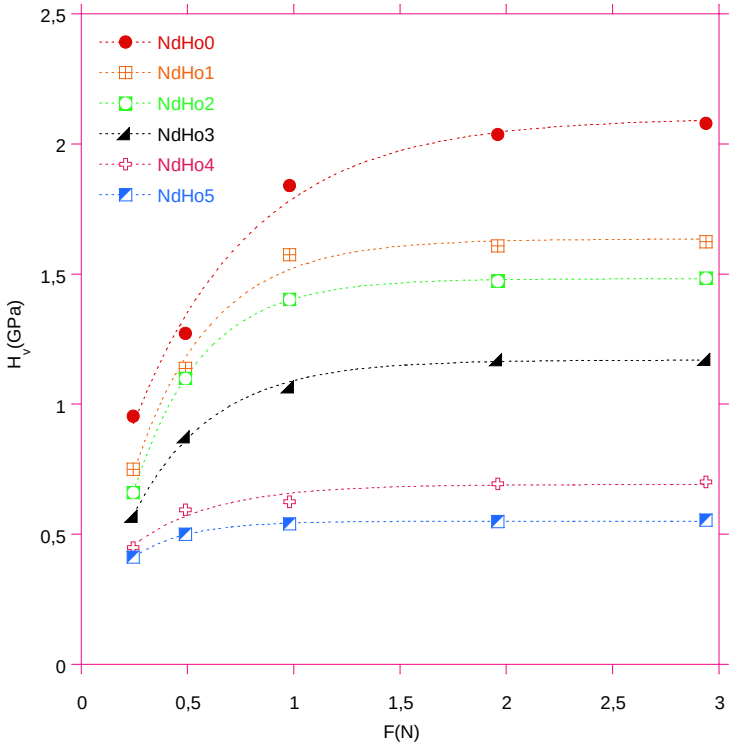

Figure 4.20: Effect of the applied indentation test loads on the Vickers microhardness for NcH

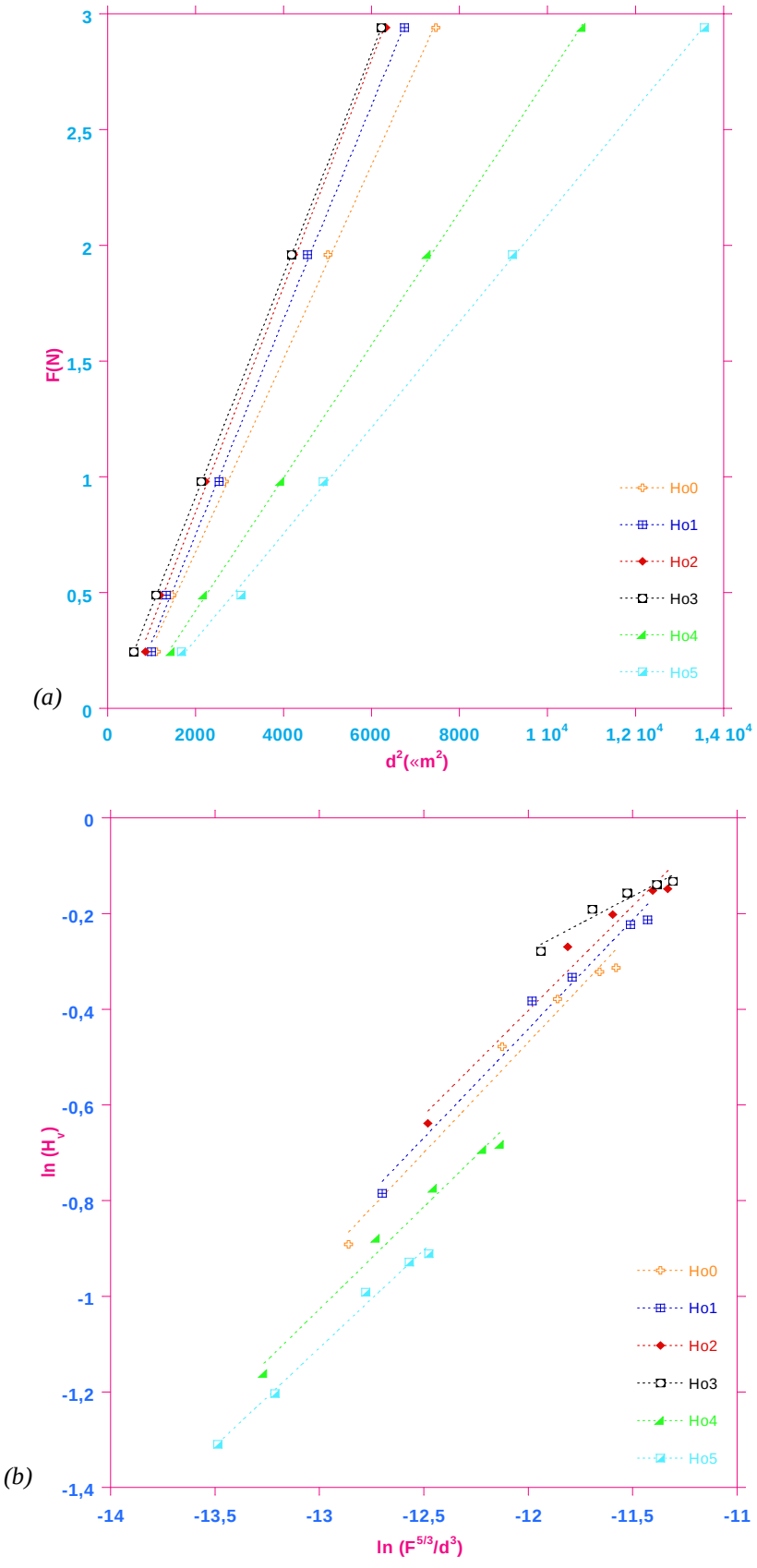

Figure 4.21: (a) Applied indentation test load against the square of the impression length for the YHo materials and (b) the graphs of ln H_V versus ln($F^{5/3}/d^3$) belonging to the YHo samples

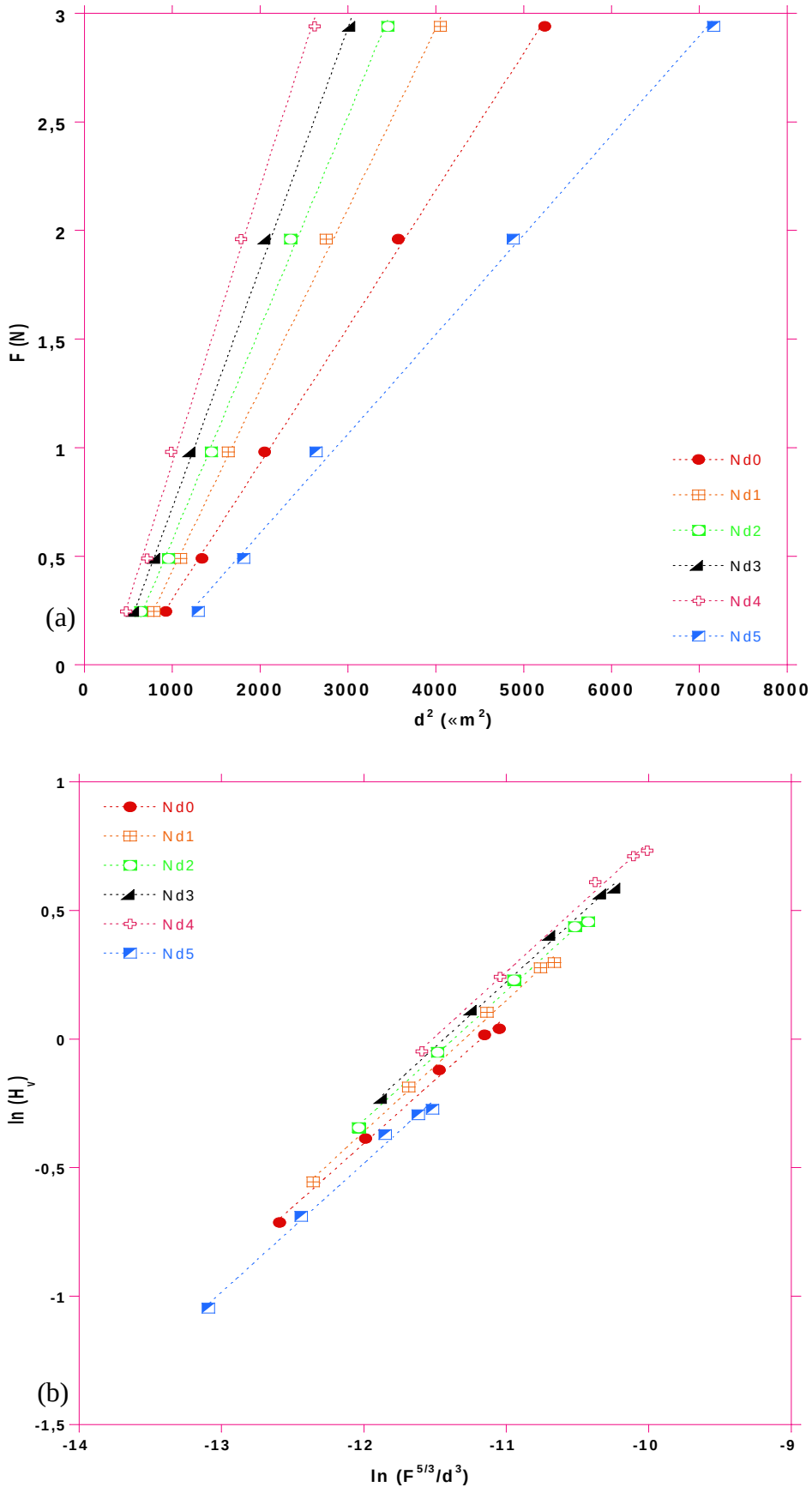

Figure 4.22: (a) Applied indentation test load against the square of the impression length and (b) Graphs of ln (H_v) versus ln($F^{5/3}/d^3$) for the YNd materials

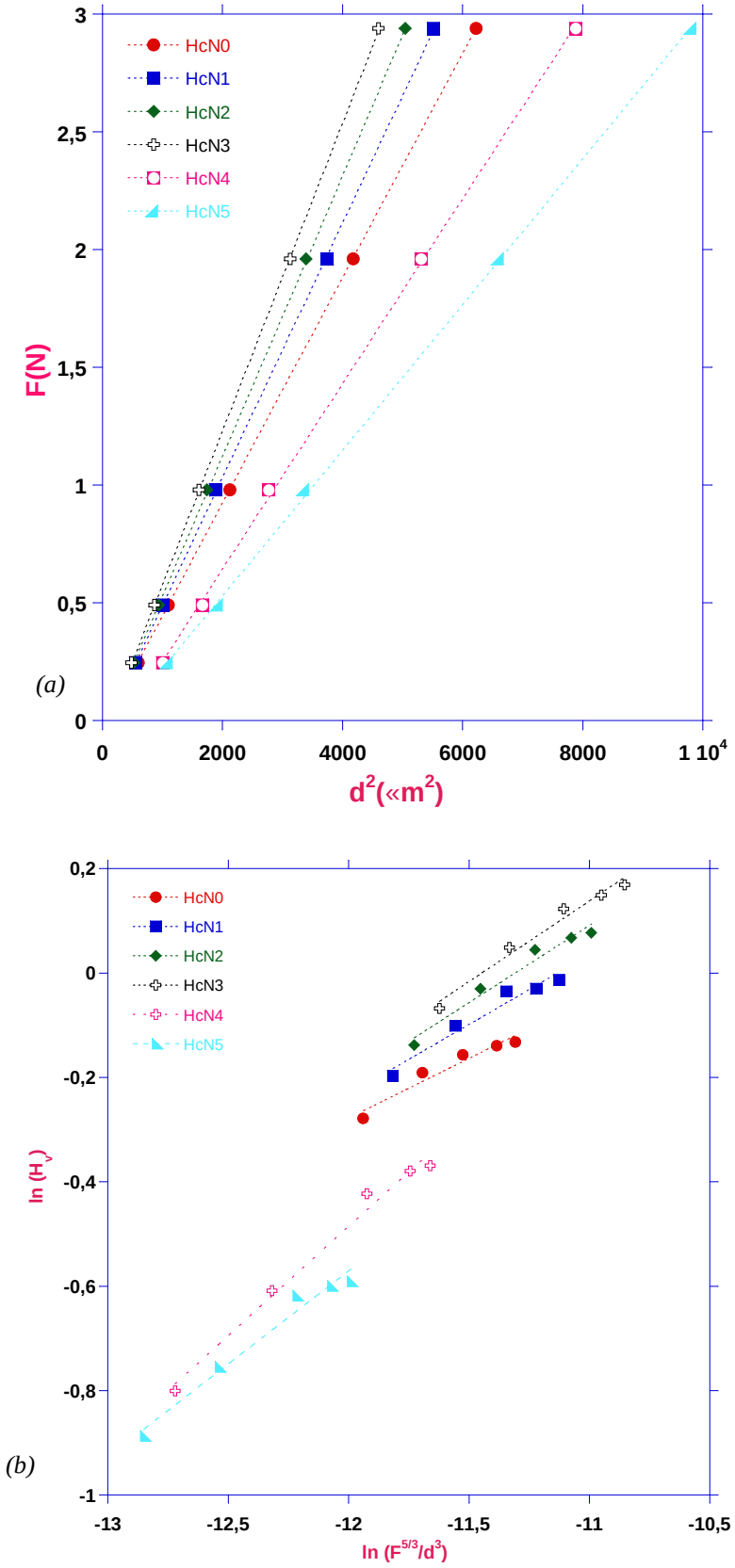

Figure 4.23: (a) Applied indentation test load against the square of the impression length and (b) Graphs of ln (H_v) versus ln ($F^{5/3}/d^3$) for the HcN materials

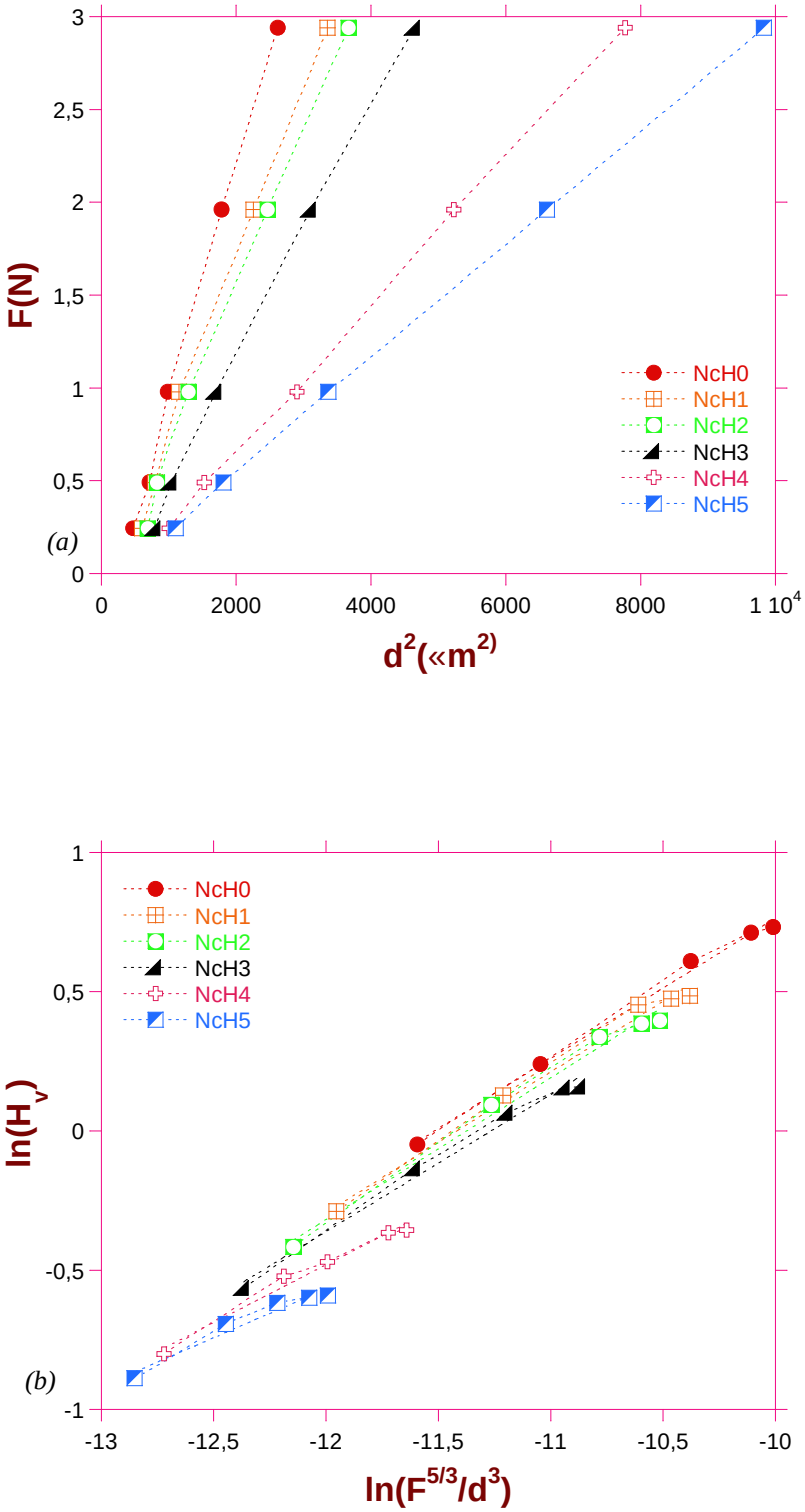

Figure 4.24: (a) Applied indentation test load against the square of the impression length and (b) Graphs of ln (H_v) versus ln ($F^{5/3}/d^3$) for the NcH materials

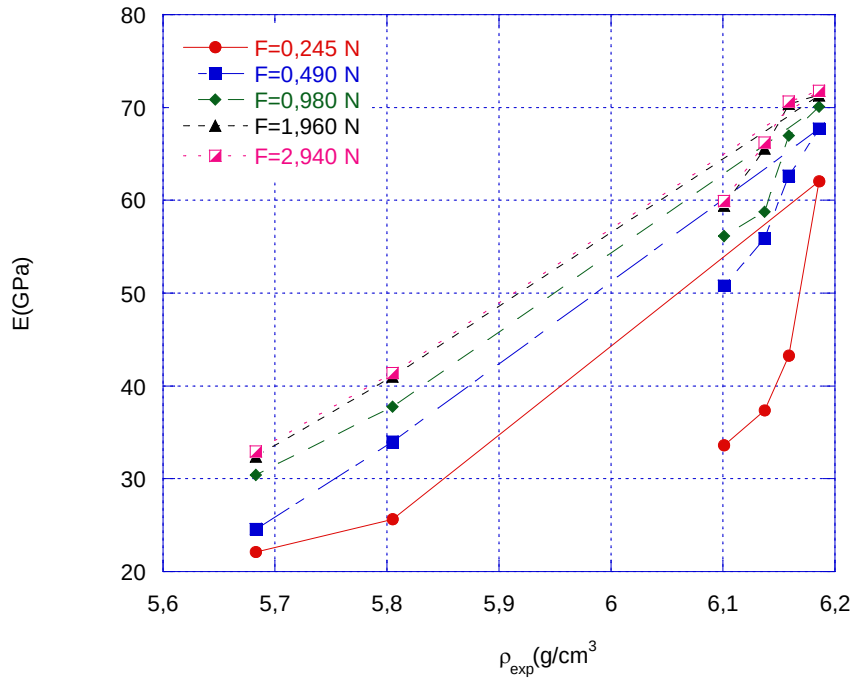

Figure 4.25: Variation of E against ρ_{exp} at different applied test loads for the YHo compounds prepared

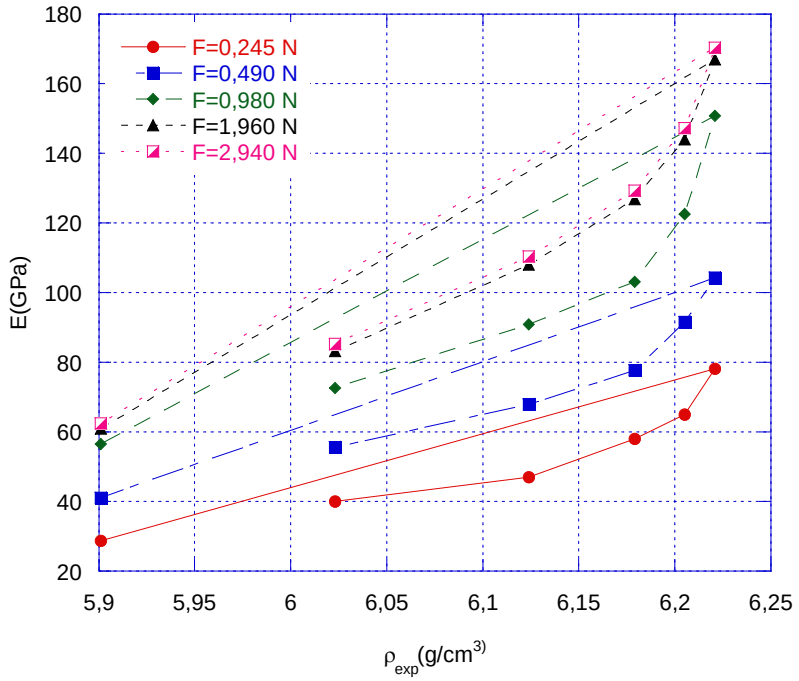

Figure 4.26: Variation of E against ρ_{exp} at different applied test loads for the YNd compounds prepared

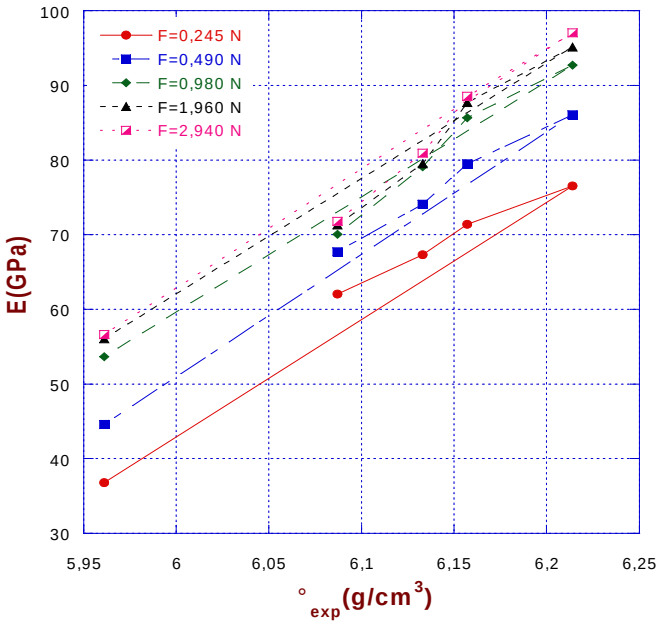

Figure 4.27: Variation of E against ρ_{exp} at different applied test loads for the HcN compounds prepared

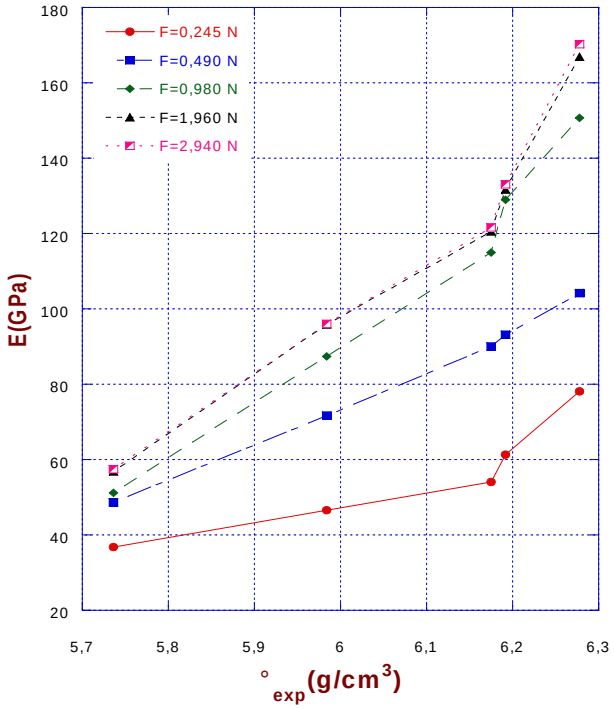

Figure 4.28: Variation of E against ρ_{exp} at different applied test loads for the NcH compounds prepared

Table 4.10: The calculated load dependent H_v, E and Y for the YHo samples

Samples	*F(N)*	*d (µm)*	*Hv (GPa)*	*E (GPa)*	*Y (GPa)*
YHo0	0,245	24,49	0,41	33,61	0,137
	0,490	33,16	0,62	50,82	0,207
	0,980	46,1	0,685	56,14	0,228
	1,960	64,63	0,725	59,42	0,242
	2,940	78,89	0,731	59,92	0,244
YHo1	0,245	23,51	0,456	37,38	0,152
	0,490	31,69	0,682	55,90	0,227
	0,980	43,39	0,717	58,77	0,239
	1,960	61,21	0,8	65,57	0,267
	2,940	74,29	0,808	66,23	0,269
YHo2	0,245	22,83	0,528	43,28	0,176
	0,490	30,6	0,764	62,62	0,255
	0,980	41,7	0,817	66,96	0,272
	1,960	58,28	0,859	70,41	0,286
	2,940	71,02	0,862	70,65	0,287
YHo3	0,245	22,04	0,757	62,05	0,252
	0,490	29,41	0,826	67,70	0,275
	0,980	40,08	0,855	70,08	0,285
	1,960	55,94	0,87	71,31	0,290
	2,940	67,84	0,876	71,80	0,292
YHo4	0,245	31,78	0,313	25,65	0,104
	0,490	40,84	0,415	34,01	0,138
	0,980	52,64	0,461	37,79	0,154
	1,960	72,86	0,5	40,98	0,167
	2,940	88,8	0,505	41,39	0,168
YHo5	0,245	33,19	0,27	22,13	0,090
	0,490	43,96	0,3	24,59	0,100
	0,980	58,04	0,371	30,41	0,124
	1,960	81,33	0,395	32,38	0,132
	2,940	99,13	0,402	32,95	0,134

Table 4.11: The characteristic parameters according to HK and IIC models for the YHo-123 system

Samples	*HK Approach*		*IIC model*	
	W (N)	*$Ax10^{-4}$ ($N/\mu m^2$)*	*$Kx10^4$ ($N^{(3-5m)/3}/\mu m^{(2-3m)}$)*	*m*
YHo0	-0,1570	4,181	0,015867	0,4613
YHo1	-0,1761	4,640	0,015252	0,4557
YHo2	-0,1219	4,787	0,012695	0,4372
YHo3	-0,0391	4,871	0,001176	0,2285
YHo4	-0,1534	2,878	0,009287	0,4275
YHo5	-0,1612	2,292	0,006808	0,4099

Table 4.12: The calculated load dependent *Hv*, *E* and *Y* for the YNd samples

Samples	*F(N)*	*d (μm)*	*Hv (GPa)*	*E (GPa)*	*Y (GPa)*
YNd0	0,245	30,45	0,489	40,08	0,163
	0,490	36,59	0,678	55,57	0,226
	0,980	45,27	0,886	72,62	0,295
	1,960	59,8	1,016	83,27	0,339
	2,940	72,39	1,040	85,24	0,347
YNd1	0,245	28,14	0,573	46,97	0,191
	0,490	33,09	0,829	67,95	0,276
	0,980	40,48	1,109	90,90	0,370
	1,960	52,48	1,319	108,11	0,440
	2,940	63,63	1,346	110,32	0,449
YNd2	0,245	25,31	0,708	58,03	0,236
	0,490	30,92	0,949	77,78	0,316
	0,980	38	1,258	103,11	0,419
	1,960	48,44	1,548	126,88	0,516
	2,940	58,79	1,577	129,26	0,526
YNd3	0,245	23,93	0,792	64,92	0,264
	0,490	28,49	1,118	91,64	0,373
	0,980	34,85	1,495	122,54	0,498
	1,960	45,46	1,758	144,09	0,586
	2,940	55,08	1,796	147,21	0,599
YNd4	0,245	21,83	0,953	78,11	0,318
	0,490	26,72	1,272	104,26	0,424
	0,980	31,42	1,839	150,73	0,613
	1,960	42,24	2,037	166,96	0,679
	2,940	51,21	2,078	170,32	0,693
YNd5	0,245	35,97	0,351	28,77	0,117
	0,490	42,56	0,501	41,06	0,167
	0,980	51,35	0,689	56,47	0,230
	1,960	69,86	0,744	60,98	0,248
	2,940	84,63	0,761	62,37	0,254

Table 4.13: The characteristic parameters according to HK and IIC models for the YNd-123

Samples	**HK model**		**IIC model**	
	W (N)	**$Ax10^{-4}$ ($N/\mu m^2$)**	**$Kx10^4$ ($N^{(3-5mA)/3}/\mu m^{(2-3m)}$)**	**m**
YNd0	-0,3290	6,289	0,025212	0,4946
YNd1	-0,4020	8,349	0,031811	0,5101
YNd2	-0,4058	9,772	0,030469	0,5029
YNd3	-0,3800	11,057	0,032363	0,5052
YNd4	-0,3459	12,671	0,033189	0,5039
YNd5	-0,3057	4,578	0,025222	0,5011

Table 4.14: The calculated load dependent *Hv*, *E* and *Y* for the HcN samples

Samples	*F(N)*	*d (µm)*	*Hv (GPa)*	*E (GPa)*	*Y (GPa)*
HcN0	0,245	24,49	0,757	62,05	0,252
	0,49	33,16	0,826	67,70	0,275
	0,98	46,1	0,855	70,08	0,285
	1,960	64,63	0,87	71,31	0,290
	2,940	78,89	0,876	71,80	0,292
HcN1	0,245	23,51	0,821	67,29	0,274
	0,49	31,69	0,904	74,10	0,301
	0,98	43,39	0,965	79,09	0,322
	1,960	61,21	0,97	79,50	0,323
	2,940	74,29	0,987	80,90	0,329
HcN2	0,245	22,83	0,871	71,39	0,290
	0,49	30,6	0,970	79,50	0,323
	0,98	41,7	1,045	85,65	0,348
	1,960	58,28	1,070	87,70	0,357
	2,940	71,02	1,080	88,52	0,360
HcN3	0,245	22,04	0,934	76,55	0,311
	0,49	29,41	1,050	86,06	0,350
	0,98	40,08	1,131	92,70	0,377
	1,960	55,94	1,161	95,16	0,387
	2,940	67,84	1,184	97,04	0,395
HcN4	0,245	31,78	0,449	36,80	0,150
	0,49	40,84	0,544	44,59	0,181
	0,98	52,64	0,655	53,69	0,218
	1,960	72,86	0,684	56,06	0,228
	2,940	88,8	0,691	56,64	0,230
HcN5	0,245	33,19	0,412	33,77	0,137
	0,49	43,96	0,47	38,52	0,157
	0,98	58,04	0,539	44,18	0,180
	1,960	81,33	0,549	45,00	0,183
	2,940	99,13	0,554	45,41	0,185

Table 4.15: The characteristic parameters according to HK and IIC models for the HcN-123

Samples	**HK model**		**IIC model**	
	W (N)	**$Ax10^{-4}$ ($N/\mu m^2$)**	**$Kx10^4$ ($N^{(3-5mA)/3}/\mu m^{(2-3m)}$)**	**m**
HcN0	-0,038871	4,7868	0,0011804	0,22887
HcN1	-0,051369	5,4086	0,0019572	0,2672
HcN2	-0,06378	5,9586	0,0028395	0,29592
HcN3	-0,07432	6,5365	0,0034244	0,30869
HcN4	-0,1421	3,9294	0,0093345	0,41849
HcN5	-0,089409	3,0914	0,0040768	0,35655

Table 4.16: The calculated load dependent *Hv*, *E* and *Y* for the NcH samples

Samples	*F(N)*	*d (μm)*	*Hv (GPa)*	*E (GPa)*	*Y (GPa)*
NcH0	0,245	21,83	0,953	78,11	0,318
	0,49	26,72	1,272	104,26	0,424
	0,98	31,42	1,839	150,73	0,613
	1,960	42,24	2,037	166,96	0,679
	2,940	51,21	2,078	170,32	0,693
NcH1	0,245	24,61	0,749	61,39	0,250
	0,49	28,25	1,137	93,19	0,379
	0,98	33,97	1,574	129,01	0,525
	1,960	47,54	1,607	131,72	0,536
	2,940	57,93	1,624	133,11	0,541
NcH2	0,245	26,23	0,66	54,10	0,220
	0,49	28,74	1,099	90,08	0,366
	0,98	35,98	1,403	114,99	0,468
	1,960	49,68	1,472	120,65	0,491
	2,940	60,57	1,485	121,72	0,495
NcH3	0,245	28,24	0,569	46,64	0,190
	0,49	32,21	0,875	71,72	0,292
	0,98	41,26	1,067	87,46	0,356
	1,960	55,71	1,17	95,90	0,390
	2,940	68,2	1,172	96,06	0,391
NcH4	0,245	31,78	0,449	36,80	0,150
	0,49	39,09	0,594	48,69	0,198
	0,98	53,89	0,625	51,23	0,208
	1,960	72,33	0,694	56,88	0,231
	2,940	88,17	0,701	57,46	0,234
NcH5	0,245	33,19	0,412	33,77	0,137
	0,49	42,62	0,5	40,98	0,167
	0,98	58,04	0,539	44,18	0,180
	1,960	81,33	0,549	45,00	0,183
	2,940	99,13	0,554	45,41	0,185

Table 4.17: The characteristic parameters according to HK and IIC models for the NcH-123

Samples	**HK model**		**IIC model**	
	W (N)	**$Ax10^{-4}$ ($N/\mu m^2$)**	**$Kx10^4$ ($N^{(3-5mA)/3}/\mu m^{(2-3m)}$)**	**m**
NcH0	-0,34577	12,672	0,033202	0,50404
NcH1	-0,25331	9,6427	0,032253	0,50584
NcH2	-0,25632	8,8276	0,032701	0,50905
NcH3	-0,24231	6,9309	0,025516	0,49191
NcH4	-0,14503	3,9789	0,0089604	0,41466
NcH5	-0,073999	3,0733	0,0037928	0,35023

Table 4.18: Comparison results: H_V, H_{HK} and H_{IIC} for YHo

Samples	H_{HK} *(GPa)*	H_{IIC} *(GPa)*	H_V *(GPa)*
YHo0	0,775	0,634	0,725–0,731
YHo1	0,860	0,692	0,800–0,808
YHo2	0,903	0,765	0,859–0,862
YHo3	0,887	0,836	0,870–0,876
YHo4	0,533	0,103	0,500–0,505
YHo5	0,425	0,347	0,395–0,402

Table 4.19: Comparison results: H_V, H_{HK} and H_{IIC} for YNd

Samples	H_{HK} *(GPa)*	H_{IIC} *(GPa)*	H_V *(GPa)*
YNd0	1,166	0,719	1,016-1,040
YNd1	1,548	1,067	1,319-1,346
YNd2	1,812	1,426	1,548-1,577
YNd3	2,050	1,857	1,758-1,796
YNd4	2,349	2,513	2,037-2,078
YNd5	0,849	0,413	0,744-0,761

Table 4.20: Comparison results: H_V, H_{HK} and H_{IIC} for HcN

Samples	H_{HK} *(GPa)*	H_{IIC} *(GPa)*	H_V *(GPa)*
HcN0	0,887664	0,83676	0,870-0,876
HcN1	1,002971	1,0196	0,970-0,987
HcN2	1,104963	0,95227	1,070-1,080
HcN3	1,212129	1,73520	1,1611,184
HcN4	0,728668	0,54693	0,684-0,691
HcN5	0,573269	0,50476	0,549-0554

Table 4.21: Comparison results: H_V, H_{HK} and H_{IIC} for NcH

Samples	H_{HK} *(GPa)*	H_{IIC} *(GPa)*	H_V *(GPa)*
NcH0	2,3499	1,63597	2,037-2,078
NcH1	1,7881	1,33837	1,607-1,624
NcH2	1,6370	1,2241	1,472-1,485
NcH3	1,2853	0,970855	1,170-1,172
NcH4	0,73785	0,612578	0,694-0,701
NcH5	0,56991	0,510665	0,549-0,554

CHAPTER 5

CONCLUSION

In the current study, we try to improve the microstructural, electrical, mechanical and superconducting properties of the Y-123 superconducting ceramics by the partial replacement of Y particles for Ho impurities and by the partial replacement of Ba particles for Nd impurities in their crystal structures. The standard experimental measurements such as the bulk density, dc resistivity, transport critical current density, X-ray diffraction, electron dispersive spectroscopy, scanning electron microscopy and Vickers microhardness are performed to catch the optimum doping level of Ho, Nd and co-doping of Ho+Nd particles. In other words, we have shown that the effect of hole (filling) localization effect, onset–offset critical transition temperature, spin-gap opening temperature, crystallinity, crystal plane alignments, crystal structure, grain size, phase purity, lattice parameters, surface morphologies and real (load independent) microhardness values are of critical importance to the SEM, XRD, H_v and dc resistivity behavior of the pure, Y-site Ho substituted and Ba-site Nd substituted Y-123 bulk superconducting matrix. Every result observed from the experimental examinations illustrates that the crucial characteristics mentioned above improve regularly with the enhancement of the Ho content level at the Y-sites in the superconducting core up to a critical value of x=0,100 (optimum), the enhancement of the Nd content level at the Ba-sites in the superconducting core up to a critical value of y=0,250 (optimum) and

the enhancement of the co-doping content level at the Y-sites and Ba-sites in the superconducting core up to a critical value of x, y=0,100 (optimum), after which the properties tend to degrade considerably. Shortly, excess (0,100 < x for only Ho in YHo, 0,250 < y for only Nd in YNd, 0,100 < y for only Nd in HcN and 0 < x for only Ho in NcH) penetration of YBCO diminishes the crystal lattice, and the major experimental evidences to be inferred from this work are as the followings:

- The dc resistivity measurements demonstrate that the normal state resistivity of the Y-123 materials after T_c^{onset} value systematically increases with ascending the Ho concentration level in YHo until the certain value x=0,100, ascending the Nd concentration level in YNd until the certain value y=0,100, ascending the Nd concentration level until the certain value y=0,100 and descending the Ho concentration level until the certain value x=0 owing to both the enhancement in the metallic connectivity between the superconducting grains and the optimization of the mobile hole density and possible improvements in the lattice vibration. As for the room temperature resistivities, the minimum resistivity values of about 2,37 mΩ.cm, 2,77 mΩ.cm, 1,72 mΩ.cm and 2,84 are obtained for the YHo3, the YNd4, the HcN3 and the NcH0 compounds respectively while the YHo5, the YNd5, the HcN4 and the NcH4 the (maximum doped) sample has the maximum resistivity value of about 8,15 mΩ.cm. The consider increase in the resistivity stems from the decrement in the mobile hole concentration (hole localization effect) of the Cu–sites in the Y-123 system.

- Furthermore, both the T_c^{onset} and T_c^{offset} values belonging to the samples increase significantly up to the optimum doping level of Ho, Nd and co-doping inclusions as a consequence of the increment in the connectivity between the superconducting grains, average crystallite size and mobile hole concentration in the

$Cu–O_2$ layers. From the Ho content level of x=0,100 onwards in the YHo matrix, from the Nd content level of y=0,250 onwards in the YNd matrix, from the Nd content level of y=0,100 onwards in the HcN matrix, from the Ho content level of x=0 onwards in the HcN matrix the values degrade harshly due to the phase transition from optimally doped state to the underdoped state position in the crystal structure. In this respect, the T_c^{onset} and T_c^{offset} values are noted to be about 94,38 K and 92,14 K for the YHo3 sample and 90,12 K and 43,89 K for the YHo5 compound. It is necessary to underline that the former material has the smallest broadening degree of 2,24 K. At the same time, the T_c^{onset} and T_c^{offset} values are noted to be about 98,93 K and 97,25 K for the YNd4 sample and 54,84 K and 32,97 K for the YNd5 compound. It is necessary to underline that the former material has the smallest broadening degree of 1,68 K. The T_c^{onset} and T_c^{offset} values are noted to be about 97,22 K and 94,84 K for the HcN3 sample and 84,92 K and 60,72 K for the HcN4 compound. It is necessary to underline that the former material has the smallest broadening degree of 2,38 K. Finally, the T_c^{onset} and T_c^{offset} values are noted to be about 98,13 K and 96,76 K for the NcH0 sample and 99,51 K and 75,66 K for the NcH4 compound. It is necessary to underline that the former material has the smallest broadening degree of 1,37 K.

- Similarly, the bulk densities (degree of granularity) increase (decrease) monotonously with the enhancement of the Ho in YHo and the enhancement of the Nd in HcN up to optimum doping level of x, y=0,100 and the enhancement of the Nd individuals in YNd up to optimum doping level of y=0,250 as consequence of the improvement of the interaction between the superconducting grains.

- The experimental XRD results present that every sample crystallizes in the orthorhombic structure with space-group P/mmm. In fact, the orthorhombic crystal system improves with the enhancement in Ho doping level at the Y-site and Nd doping level in the superconducting matrix up to a critic value of x,y=0,100 and with the enhancement in Nd doping level at the Ba-site in the superconducting matrix up to a critic value of y=0,250 after which the split diffraction peaks guarantee that the crystal structure tends to present the pseudotetragonal, confirming that the excess Ho and Nd ingredients are unfavorable for the Y-123 phase formation but more favorable for the Cu_1 site.

- Similar to the DC resistivity measurement results, at the optimum doping level the maximum transport critical current density is obtained to be about 384 $A.cm^{-2}$ for the YHo3 sample, about 224 $A.cm^{-2}$ for the YNd3 sample, about 251 $A.cm^{-2}$ for the HcN3 sample and about 225 $A.cm^{-2}$ for the NcH0 sample verifying that the Ho and Nd inclusions inserted in the Y-123 superconducting matrix introduce the nucleation centers (effective flux pinning centers) into the crystal structure. However, regarding excess Ho and Nd impurities, there is considerable decrease in the J_c value due to the presence of the increased pores, hole localization effect, voids, stacking faults, planar and micro defects (twin, domains etc.) and grain boundary resistivity and weak-links between the superconducting grains.

- SEM images point out that the best texturing, crystallinity and connectivity between grains, largest grain size and lowest porosity are observed for the YHo3, YNd4, the HcN3 or NcH0. Additionally, the SEM measurement results give that the dense surface with a fine interaction between the superconducting grains regularly improves with the enhancement of the Ho inclusions in YHo and Nd inclusion in HcN superconducting matrix up to x, y=0,100, with the enhancement of

the Nd inclusions in the YNd superconducting matrix up to y=0,250 after this critical doping value and all doping value in NcH, the surface morphologies start to retrograde considerably due to the increase of the porosity (decrease in the crystalline sizes) partial melting, voids and cracks leading to new phase formations such as $BaCuO_2$; Y-247 and Y-124. Shortly, among the samples, the YHo3, YNd4, HcN3 and NcH0 specimens are observed to be the smoothest and densest surface morphology with the most uniform surface appearance, largest crystalline size, best texturing, lowest porosity, best crystallinity and grain connectivity.

- EDS investigations show that the elements used for the preparation of samples distribute homogeneously, confirming that all the elements incorporate into the crystalline structure of the samples prepared. The EDS findings present that for all the samples no extra peaks are observed with the increase of the impurity concentration in their EDS pictorials, verifying that the elements each incorporate successfully into the Y-123 superconducting crystal structure. Besides, the peak intensities of the cupper, barium and particularly yttrium elements noticeably decrease with the presence of the holmium and neodymium inclusions in the superconducting matrix. This is associated with the fact that the Ho inclusions inserted may substitute for the Cu (after $x > 0,100$) and Y elements and the Nd inclusions inserted may substitute for the Ba, the Cu (after $y > 0,250$) and Y elements. Hence, the experimental evidence is enough to discuss why the superconducting properties degrade with the excess Ho and Nd nanoparticles in the crystal structure.

- Unfortunately, it is found that the mechanical, electrical and especially superconducting characteristics degrade dramatically up to the Ho content level of x=0,250 in NcH beyond which they destroy utterly. However, all the properties

improve with the increase in the Nd individuals until the concentration level of y=0,100 in HcN after which they tend to retrograde systematically and in fact reach their local minimum points (but still exhibit the superconducting characteristics). The long and short of it is that the enhancement in the properties is the effect of both the decrement of the porosity, grain boundary resistivity and weak-links in the crystal structure and the improvement of the homogeneities in the oxidation states of the superconducting grains. It is attributed to the fact that Nd element appears at both divalent and trivalent states in the crystal. In the case of former position, the mechanical, electrical and especially superconducting properties belonging to the Y-123 co-doped with Nd and Ho nanoparticles while trivalent cation state noticeably damages the properties due to the presence of the increased local structural distortions and mobile hole localization (filling) in the crystal system.

- The final characterization method, the microhardness measurements conducted at different applied indentation test loads (0,245 N-2,940 N) illustrate that all the samples prepared in this work exhibit the typical Rise Indentation Size Effect behavior (hardness increases with the loads). Thus, in the materials the plastic deformation plays dominant character as compared to the elastic deformation (no elastic recovery). Moreover, the elastic modulus and yield strength values extracted from the Vickers microhardness findings are found to enhance (linear microhardness behavior) with ascending the Ho and the Nd content level until the certain value of x, y=0,100 and with ascending the Nd content level until the certain value of y=0,250 beyond which and with ascending the Ho content level, they start to suppress significantly as a consequence of the increment in the specimen cracking/porosity, minor phases, grain boundary weak-links and irregular grain orientation distribution.

- As for the theoretical modeling belonging to the Y-site Ho and Ba-site Nd substituted Y-123 superconducting ceramics, it is found that the IIC method is fairly superior to HK approach for the description of the load independent microhardness values.

REFERENCES

[1] M. Runde, IEEE T. Appl. Supercond. 5 (1995) 813–816.

[2] H. Miao, M. Meinesz, B. Czabai, J. Parrell, S. Hong, AIP Conf. Proc. 986 (2008) 423–430.

[3] A. Godeke, D. Cheng, D.R. Dietderich, C.D. English, H. Felice, C.R. Hannaford, S.O. Prestemon, G. Sabbi, R.M. Scanlan, Y. Hikichi, J. Nishioka, T. Hasegawa, IEEE T. Appl. Supercond. 18 (2008) 516–519.

[4] H. Maeda, Y. Tanaka, M. Fukutomi, T. Asano, Jpn. J. Appl. Phys. Lett. 27 (1988) L209–L210.

[5] J.M. Tarascon, Y. Lepage, L.H. Greene, B.G. Bagley, P. Barboux, D.M. Hwang, G.W. Hull, W.R. Makinnon, M. Giroud, Phys. Rev. B 38 (1988) 2504–2508.

[6] P. Bordet, C. Chaillout, J. Chenavas, J.L. Hodeau, M. Marezio, J. Karpinski, E. Kaldis, Nature 336 (1988) 596–599.

[7] P. Marsh, R.M. Fleming, M.L. Mandich, A.M. DeSantolo, J. Kwo, M. Hong, L.J. Martinez-Miranda, Nature 334 (1988) 660–662.

[8] B. Batlogg, Solid State Commun. 107 (1998) 639–647.

[9] A. Kuczkowski, B. Kusz, Synth. Met. 94 (1998) 145–148.

[10] M.E. Sagsoz, M. Ertugrul, U. Cevik, Mater. Lett. 60 (2006) 1778–1781.

[11] S. Gupta, R.S. Yadav, N.P. Lalla, G.D. Verma, B. Das, Integr. Ferroelectr. 116 (2010) 68–81.

[12] S. Nagaya, N. Hirano, M. Naruse, T. Watanabe, T. Tamada, IEEE T. Appl. Supercond. 23 (2013) 5602804–5602807.

[13] F.N. Werfel, U. Floegel-Delor, R. Rothfeld, T. Riedel, B. Goebel, D. Wippich, P. Schirrmeister, Supercond. Sci. Technol. 25 (2012) 014007.

[14] T.A. Coombs, IEEE T. Appl. Supercond. 21 (2011) 3581–3586.

[15] H.H. Xu, L. Cheng, S.B. Yan, D.J. Yu, L.S. Guo, X. Yao, J. Appl. Phys. 111 (2012) 103910.

[16] K.Y. Choi, I.S. Jo, S.C. Han, Y.H. Han, T.H. Sung, M.H. Jung, G.S. Park, S.I. Lee, Curr. Appl. Phys. 11 (2011) 1020–1023.

[17] S. Altin, M.A. Aksan, M.E. Yakinci, J. Alloy. Compd. 584 (2014) 553–557.

[18] S. Jin, T.H. Tiefel, R.C. Sherwood, M.E. Davis, R.B. van Dover, G.W. Kammlott, R.A. Fasrnacht and H.D. Keith, Appl. Phys. Lett. 52 (1988) 2074–2076.

[19] K. Salama, V. Selymanickam, L. Gao and K. Sun, Appl. Phys. Lett. 54 (1989) 2352–2354.

[20] L. Zhou, P. Zhang, P. Ji, K. Wang and X. Wu, Supercond. Sci. Technol. 3 (1990) 490-492.

[21] T. Egi, J.G. Wen, K. Koroda, H. Unoki and N. Koshizuka, Appl. Phys. Lett. 67 (1995) 2406–2408.

[22] Anonyms, (2014), http://en.wikipedia.org/wiki/Superconductivity.

[23] A. Mann, Nature 475 (2011) 280–282, doi:10.1038/475280a.

[24] D. Pines, (2002), The Gap Symmetry and Fluctuations in High-Tc Superconductors, New York: Kluwer Academic, pp.111–142, doi:10,1007/0-306-47081-0_7, ISBN0-306-45934-5.

[25] P. Monthoux, A.V. Balatsky, and D. Pines, Phys. Rev. Lett. 67 (1991) 3448–3451, doi:10.1103/PhysRevLett.67.3448.

[26] J.C. Gallop, Supercond. Sci. Technol. 3 (1990) 20-25.

[27] R. Clem, Supercond. Sci. Technol. 11 (1998) 909–914.

[28] N.W. Arhcraft and N.D. Mermin, (1976), Solid State Physics, Holt Rinehart and Wiston.

[29] H.K. Onnes, Common Phys. Lab Unive Leiden, (1911), 119-120.

[30] W.Meissner and R. Ochsenfeld, Naturwissenschaften 21 (1933) 787.

[31] Anonyms, (2014), www.superconductors.org.

[32] M.A. Aksan, S. Altin, M.E. Yakinci, A. Guldeste, Y. Balci, Mater. Sci. Tech. 27 (2011) 314-319.

[33] A. Tsukamoto, K. Imagawa, M. Hiratani, K. Kanehori, K. Takagi, Jpn. J. Appl. Phys. 30 (1991) L 830- L 833.

[34] A.R Innes, E.H. Rhoderic, (1969), Introduction to Superconductivity, Oxford Pergaman Press London.

[35] A. Goyal, E.D. Specht, Z.L. Wang, D.M. Kroeger, Ultramicroscopy 67 (1997) 35-57.

[36] F.Keskin, Thesis of Master, The Abant Izzet Baysal University, (2006).

[37] Anonyms, (2014), http://en.wikipedia.org/wiki/Superconductivity.

[38] R. Beyers, B.T. Aim, G. Gorman, V.Y. Lee, S.S.P. Parkin, M.L. Ramirez, K.P. Roche, J.E. Vazquez, T.M. Giir and R.A. Huggings, Nature 340 (1989) 619-621.

[39] J. Reyes-Gasga, T. Krekels, G. Van Tendeloo, J. Van Landuyt, S. Amelinckx, W.H.M. Bruggink, H. Verweij, Physica C 159 (1989) 831-848.

[40] G. Van Tendeloo, T. Krekels, O. Milat, S. Amelinckx, Journal of Alloys and Compounds (JALCOM) 195 (1993) 307-314.

[41] Anonyms, (2014), http://en.wikipedia.org/wiki/Superconductivity#mediaviewer/File:Sc_history.gif.

[42] G. Bilgiç, Thesis of Master, Dokuz Eylul University, (2004).

[43]Anonyms, (2014), http://en.wikipedia.org/wiki/High-temperature_superconductivity.

[44] W. Jin, S. Hao, H. Zhang, New J. Phys. 11 (2009) 3036-3052 doi:10.1088/1367-2630/11/11/113036.

[45] Anonyms, (2014), http://www.ch.ic.ac.uk/rzepa/mim/century/html/ybco.htm.

[46] Anonyms, (2014), http://hoffman.physics.harvard.edu/materials/images/ybco.gif.

[47] Anonyms, (2014), http://commons.wikimedia.org/wiki/File:YBCO_structure.jpg.

[48] S. Heinemann, R. Wirth, G. Dresen, Pys. Chem. Minerals 30 (2003), 125-130.

[49] H. Hilgenkamp, J. Mannhart, Reviews of Modern Physıcs 74 (2002), 485-549.

[50] Ch. Jooss, L.O. Kautschor, M.P. Delamare, B. Bringmann, K. Guth, V. Born, S. Sievers, H. Walter, J. Dzick, J. Holzmann, H.C. Freyhardt, B. de Boer, B. Holzapfel, F. Sandiumenge, MRS Proceedings 659 (2001) II7.1.

[51] N. Murayama, Y. Kodama, S. Sakaguchi, F.Wakai, K. Michishita, Y. Ikuhara, Physica C: Superconductivity 185–189 (1991) 2213-2214.

[52] I.D. Heittnger, K.E. Gray, D.J. Miller, D.H. Kim, D.G. Steel, B.R. Washburn, J. Sharping, C. Moreov, M. Eddy, J.E. Tkoczyk, J. Deluca, J.H. Kang, and J. Tolvacchion, Physica C 273 (1997) 275-280.

[53] B. Lebech, (1999), Annual Progress Report of the Condensed Matter Physics and Chemistry Department, 1-170.

[54] H. Hilgenkamp, C.W. Schneider, B. Goetz, R.R. Schulz, A. Schmehl, H. Bielefeldt and J. Mannhart, Supercond. Sci. Technol. 12 (1999) 1043–1045.

[55] P. Mikheenko, J. Hruat, Q. Yhu, M. Lonescu, and S. Dau, Supercond. Sci. Technol 10 (1997) 444-449.

[56] G. Hammerl, H. Bielefeldt, S. Leitenmeier, A. Schmehl, C.W. Schneider, A. Weber and J. Mannhart, Large Grain Boundary Area Superconductors, Institue of Physics, Augsburg University 1-11.

[57] A. Georgeta, Romanian Reports in Physiscs 56 (2004) 404-412.

[58] K.E. Gray, D.J. Miller, M.B. Field, D.H. Kim and P. Berghuis, Pysica C 341-348 (2000) 1397-1400.

[59] R. Ramesh, B.G. Bagley, J.M. Tarascon, S.M. Green, M.L. Rudee and H.L. Luo, Apply Phys.67 (1990) 379-387.

[60] S.P. Ashworth, B.A. Glowacki, M.P. James, R. Garre and S. Conti, IEEE Trans. Appl. Supercon. 5 (1995) 1271-1274.

[61] X.Y. Lu, A. Nagete, K. Watanabe, T. Nojima, D. Kamio, K. Sugaware, and S. Kamada, IEEE T. Appl. Supercond. 11 (2001) 3553-3556.

[62] C.S. Pande, Matter Phys. Mech. 2 (2000) 1-9.

[63] S.M. Cassidy, L.F. Cohen, M.N. Cuthbert, S.X. Dou and A.D. Caplin, Cryogenics 32 (1992) 1034-1037.

[64] I. Felner and B. Brosh, Phys. Rev. B 43 (1991) 10364–10367.

[65] A.V. Narlikar, (2005), Frontiers in superconducting materials. New York: Springer-Verlag Berlin Heidelberg.

[66] L. Garwin, Nature 332 (1988) 103.

[67] Y. Tokura, Physica C185-189 (1991) 174-179.

[68] C. Greaves and P.R. Slater, Physica C 161 (1989) 245-251.

[69] G. Xiao, M.Z. Cieplak, D.Musser, A. Gavrin, F.H. Streitz, C.L. Chien, J.J. Rhyne and J.A. Gotaas, Nature 332 (1988), 238-240.

[70] Y. Tokura, J.B. Torrance, T.C. Huang and A.I. Nazzal, Phys. Rev. B38 (1988), 7156-7159.

[71] P. Karen, H. Fjellvag, O. Braaten, A. Kjekshus, H. Bratsberg, Acta Chern. Scand. 44 (1990) 994.

[72] T. Tamegai, A. Watanabe, I. Oguro and Y. Iye, Jpn. J. Appl. Phys. 26 (1987) L1304-L1306.

[73] Y. Nakabayashi, Y. Kubo, T. Manako, I Tabuchi, A. Ochi, K. Utsumi, H. Igarashi and M. Yonezawa, Jpn. J. Appl. Phys.27 (1988) L64-L66.

[74] M. Guillaume, P. Allenspach, W. Henggeler, J. Mesot, B. Roessli, U. Staub, P. Fischer, A. Furrer and V. Trounov, J.Phys.: Condens. Matter 6 (1994) 7963-7976.

[75] J.M.S. Skakle, Materials Science and Engineering, R23 (1998) 1-40.

[76] H. Arabi, D.A. Ciomartan, M.E. Clamp, P.W. Mitchell, J.W. Ross, D.J. Sandiford, O.S. Mills and R.H. Fenn, PhysicaC 193 (1992) 90-98.

[77] Y. LePage, T. Siegrist, S.A. Sunshine, L.F. Schneemeyer, D.W. Murphy, S.M. Zahurak, J.V. Waszczak, W.R. McKinnon, J.M. Tarascon, G.W. Hull and L.H. Greene, Phys. Rev. B 36 (1987) 3617-3621.

[78] R.P. Gupta and M. Gupta, Phys. Rev. B 47 (1993) 2795-2800.

[79] T. Tamegai, I. Oguro, K. Koga, A. Watanabe and Y. lye, Physica B 148 (1987) 453-455.

[80] D.B. Currie and M.T. Weller, Physica C 214 (1993) 204-213.

[81] C.N.R. Rao, R. Nagarajan, A.K. Ganguli, G.N. Subbana and S.V. Bhat, Phys. Rev. B 42 (1990) 6765-6768.

[82] M. Buchgeister, W. Hiller, 8. M. Hosseini, K. Kopitzki and D. Wagener, Proceedings of the Superconductors, April 29 -May 4 1990, Rio de Janeiro, Brazil, ed. R. Nicolsky, (World Scientific Publishing, Singapore, 1990) 511-517.

[83] T. Krekels, H. Zou, G. Van Tendeloo, D. Wagener, M. Buchgeister, S.M. Hosseini and P. Herzog, Physica C 196 (1992) 363-368.

[84] J.T. Vaughey, J.P.Thiel, E.F. Hasty, D.A. Groenke, C.L. Stern, K.R. Poeppelmeier, B. Dabrowski, A.W. Mitchel and D.G. Hinks, Chem. Mater. 3 (1991) 935.

[85] B.D. Dunlap, J.D. Jorgensen, C. Segre, A.E. Dwight, J.L. Matykiewicz, H. Lee, W. Peng and C.W. Kimball, Physica C 158 (1989) 397-405.

[86] T. Krekels, G. Van Tendeloo, D. Broddin, S. Amelinckx, L. Tanner, M. Mehbod, E. Vanlathem and R. Deltour, Physica C 173 (1991) 361-376.

[87] J.M. Tarascon, P. Barboux, P.F. Miceli, L.H. Greene, G.W. Hull, M. Eibschutz and S.A. Sunshine, Phys. Rev. B 37 (1988) 7458-7469.

[88] G. Roth, P. Adelmann, G. Heger, R. Knitter and Th.Wolf, J. de Physique I 1 (1991) 721-741.

[89] G. Yıldırım, Thesis of Doctor, The Abant Izzet Baysal University, (2012).

[90] F.Yong, Z.Lian, Z.Pingxiang, J.Ping, W.Xiaozu, L.Changxun and X.Mianrong, Journal of Superconductivity, Vol. 3 No. 2, (1992), 95-97.

[91] C. Chaillout, P. Bordet, J. Chenavas, J.L. Hodeau, M. Marezio, J. Karpinski, E. Kaldis and S. Rusiecki, Solid State Commun. 70 (1989) 275–278.

[92] A. Hamrita, F.B. Azzouz, A. Madani and M.B. Salem, Physica C 472 (2012) 34–38.

[93] S.J. Hao, W.T. Jin, C.Q. Guo and H. Zhang, Physica C 475 (2012) 28–31.

[94] S.B. Guner, O. Gorur, S. Celik, M. Dogruer, G. Yildirim, A. Varilci and C. Terzioglu, J. Alloy. Compd. 540 (2012) 260–266.

[95] S. Vinu, P.M. Sarun, A. Biju, R. Shabna, P. Guruswamy and U. Syamaprasad, Supercond. Sci. Technol. 21 (2008) 1–4.

[96] S. Vinu, P.M. Sarun, R. Shabna, A. Biju and U. Syamaprasad, Mater. Lett. 62 (2008) 4421–4424.

[97] R. Shabna, P.M. Sarun, S. Vinu, A. Biju and U. Syamaprasad, Supercond. Sci. Technol. 22 (2009) 45016–45022.

[98] S. Vinu, P.M. Sarun, R. Shabna, P.M. Aswathy, J.B. Anooja and U. Syamaprasad, Physica B 405 (2010) 4355–4359.

[99] S. Vinu, P.M. Sarun, R. Shabna and U. Syamaprasad, J. Alloy. Compd. 487 (2009) 1–4.

[100] G.B. Akyuz, K. Kocabas, A. Yıldız, L. Ozyuzer and M. Ciftcioglu, J. Supercond. Nov. Magn. 24 (2011) 2189–2201.

[101] M.A. Ansari, R. Nigam, V.P.S. Awana, A. Gupta, R.B. Saxena, H. Kishan, N.P. Lalla, V. Ganesan, A.V. Narlikar and C.A. Cardoso, J. Appl. Phys. 97 (2005) 10B104-1-10B104-3.

[102] O. Gorur, G. Yildirim, S.P. Altintas and C. Terzioglu, J. Mater. Sci: Mater. El. 24 (2013) 1842–1854.

[103] M.H. Whangbo and C.C. Torardi, Science 249 (1990) 1143-1146.

[104] P.M. Sarun, S. Vinu, R. Shabna, A. Biju and U. Syamaprasad, J. Alloy. Compd. 472 (2009) 13–17.

[105] A. Biju, P.M. Sarun, R.P. Aloysius and U. Syamaprasad, J. Alloy. Compd. 454 (2008) 46–51.

[106] G. Yildirim, E. Yucel, S. Bal, M. Dogruer, A. Varilci, M. Akdogan, C. Terzioglu and Y. Zalaoglu, J. Supercond. Nov. Magn. 25 (2012) 231–237.

[107] T.J. Kistenmacher, J. Appl. Phys. 64 (1988) 5067–5070.

[108] A. Yildiz, K. Kocabas and G.B. Akyuz, J. Supercond. Nov. Magn. 25 (2012) 1459–1467.

[109] B.D. Cullity, (2001), Elements of X-ray Diffraction, third ed., Addison-Wesley.

[110] F.K. Lotgering, J. Inorg. Nucl. Chem. 9 (1959) 113–123.

[111] W. Gao and J.B. Vander Sande, Supercond. Sci. Technol. 5 (1992) 318–326.

[112] P.B. Allen, Y.E. Picket and H. Krakauer, Phy. Rev. B 37 (1988) 7482–7490.

[113] S. Martin, M. Gurvitch, C.E. Rice, A.F. Hebard, P.L. Gammel, R.M. Fleming and A.T. Fiory, Phys. Rev. B 39 (1989) 9611–9613.

[114] D.M. Newns, P.C. Pattnaik and C.C. Tsuei, Phys. Rev. B 43 (1991) 3075–3084.

[115] P.A. Lee and N. Read, Phys. Rev. Lett. 58 (1987) 2691–2694.

[116] K. Levin, J.H. Kim, J.P. Lu and Q. Si, Physica C 175 (1991) 449–522.

[117] G. Yildirim, M. Dogruer, F. Karaboga and C. Terzioglu, J. Alloy. Compd. 584 (2014) 344–351.

[118] O. Gorur, C. Terzioglu, A. Varilci and M. Altunbas, Supercond. Sci. Technol. 18 (2005) 1233–1237.

[119] M. B. Turkoz, S. Nezir, C. Terzioglu, A. Varilci and G. Yildirim, J. Mater. Sci: Mater. El. 24 (2013) 896–905.

[120] O. Ozturk, E. Asikuzun, M. Erdem, G. Yildirim, O. Yildiz and C. Terzioglu, Mater. Sci: Mater. El. 23, (2012) 511–519.

[121] P.M. Sarun, S. Vinu, R. Shabna, A. Biju and U. Syamaprasad, Mater. Lett. 62 (2008) 2725–2728.

[122] J.H. Koo and G. Cho, J. Phys. Condens. Matter 15 (2003) L729–L733.

[123] O. Ozturk, E. Asikuzun and G. Yildirim, J. Mater. Sci: Mater. El. 24 (2013) 1274–1281.

[124] A. Ianculescu, M. Gartner, B. Despax, V. Bley, Th. Leby, R. Gavrila and M. Modreanu, Appl. Surf. Sci. 253 (1996) 344–348.

[125] K. Kocabas, O. Ozkan, O. Bilgili, Y. Kadioglu and H. Yılmaz, J. Supercond. Nov. Magn. 23 (2010) 1485–1492.

[126] A. Hamrita, F.B. Azzouz, A. Madani and M.B. Salem, Physica C 472 (2012) 34–38.

[127] N.K. Sarıtekin, Y. Zalaoglu, G. Yildirim, M. Dogruer, C. Terzioglu, A. Varilci and O. Gorur, J. Alloy. Compd. 610 (2014) 361–371.

[128] G. Yildirim, S. Bal and A. Varilci, J. Supercond. Nov. Magn. 25 (2012) 1655-1663.

[129] T. Kucukomeroglu, E. Bacaksiz, C. Terzioglu and A. Varilci, Thin Solid Films 516 (2008) 2913-2916.

[130] M.R. Persland, J.L. Tallon, R.G. Buckley, R.S. Liu, and N.E. Floer, Physica C 176, (1991). 95-105.

[131] G. Yildirim, Y. Zalaoglu, M. Akdogan, S.P. Altintas, A. Varilci and C. Terzioglu, J. Supercond. Nov. Magn. 24 (2011) 2153–2159.

[132] D. Dew-Hughes, Cryogenics 14 (1974) 657-658.

[133] E.H. Brandt, Rep. Prog. Phys. 58 (1995) 1465–1594.

[134] M. Dogruer, Y. Zalaoglu, G. Yildirim, A. Varilci and C. Terzioglu, J. Mater. Sci: Mater. El. 24 (2013) 2019–2026.

[135] S. Bal, M. Dogruer, G. Yildirim, A. Varilci, C. Terzioglu, and Y. Zalaoglu, J. Supercond. Nov. Magn. 25, (2012) 847-856.

[136] K. Fujita, T. Noda, K.M. Kojima, H. Eisaki and S. Uchida, Phys. Rev. Lett. 95, (2005) 097006-1-097006-4.

[137] K. Ozturk, S. Celik, U. Cevik and E. Yanmaz, J. Alloy. Compd. 433 (2007) 46–52.

[138] Y. Zalaoglu, G. Yildirim, and C. Terzioglu, J. Mater. Sci. Mater Electron 24 (2013) 239-247doi 10,1007/s10854-012-0723-8.

[139] M. Tinkham, (1996) Introduction to Superconductivity, 2nd edn., (McGraw-Hill, New York).

[140] G. Yildirim, J. Alloy. Compd. 578 (2013) 526–535.

[141] R.R. Reddy, M. Murakami, S. Tanaka and P.V. Reddy, Physica C 257 (1996) 137–142.

[142] H. Aydin, A.Babanli, S.P. Altintas, E. Asikuzun, N. Soylu, O. Ozturk, M. Dogruer, C. Terzioglu and G. Yildirim, J. Mater. Sci: Mater. El. 24 (2013) 4566–4573.

[143] C.J. Poole, H.A. Farach, R. J. Creswick and R. Prozorov, (2007), Superconductivity, second ed., Academic Press, San Diego.

[144] M. Dogruer, G. Yildirim, A. Varilci and C. Terzioglu, J. Alloy. Compd. 556 (2013) 143–152.

[145] M. Dogruer, F. Karaboga, G. Yildirim, C. Terzioglu and O. Ozturk, J. Mater. Sci: Mater. El. 24 (2013) 2659–2666.

[146] Y. Zalaoglu, E. Bekiroglu, M. Dogruer, G. Yildirim, O. Ozturk and C. Terzioglu, J. Mater. Sci: Mater. El. 24 (2013) 2339-2345.

[147] S. Safran, A. Kılıc, E. Asikuzun, E. Kılıcarslan, O. Ozturk and A. Gencer, J. Mater. Sci: Mater. El. (2014) 2737-2747 doi:10,1007/s10854-014-1937-8.

[148] L. Hong and R.C. Bradt, J. Mater. Sci. 31, (1996) 1065–1070.

CIRRICULUM VITAE

Namık Kemal SARITEKİN

Address:

Abant Izzet Baysal University

Department of Physics,

Golkoy-Bolu, Turkey

Phone: +90 374 2541000 – 2737

Fax: +90 374 2534642

E-mail: tekinfizikster@gmail.com

Personal Details:

Gender: Male

Date of birth: 8th of December, 1970

Place of birth: Kutahya, Turkey

Education:

1989-1993 Undergraduate Studies in Physics at Middle East Technical University

2009-2011 M.S. in Electric Education at Duzce University

Thesis: A data paths design tool for automatically mapping artificial neural network on to FPGAs

2011-2015 Ph.D. in Physics at Abant Izzet Baysal University

Thesis: Investigation of mechanical and superconducting properties of

$Y_{1-x}Ho_xBa_{2-y}Nd_yCu_3O_{7-\delta}$ superconducting samples by experimental and theoretical methods

Specialization: Type II Superconducting materials.

Publications:

1. N.K. Saritekin, Y. Zalaoglu, G. Yildirim, C. Terzioglu and O. Gorur "Determination of solid solubility level of Ho nanoparticles in Y-123 superconducting matrix and strong Cu1 site preference of nanoparticles", Journal of Alloys and Compounds, doi: http://dx.doi.org/10.1016/j.jallcom.2014.04.037

2. N.K. Saritekin, M. Dogruer, G. Yildirim and C. Terzioglu "Research on MgB_2 bulk superconductors exposed to Ag nanoparticles diffusion", J Mater Sci: Mater Electron doi: 10,1007/s10854-014-1993-0.

3. N.K. Sarıtekin, O. Görür, A. Varilci, C. Terzioğlu, G. Yıldırım and M. Doğruer, "Substitution for Nd in High-Tc Superconductor $YBa_2Cu_3O_{7-\delta}$ Ceramics", ICSM 2014, Antalya, Turkey, Apr 27-May 2 2014, pp:128

4. Y. Zalaoglu, G. Yildirim, N.K Saritekin, H. Buyukuslu, A. Varilci, C. Terzioglu, and O. Gorur, "Important defeats on pinning of 2D pancake vortices in highly anisotropic Bi-2212 superconducting matrix with homovalent Bi/La substitution" , Journal of Alloys and Compounds.

Work Experience:

From 1993 to 2015, I have worked at the Science Collage, as a Physics Teacher.